Astronomy & Astrophysics manuscript no. Paper_acc
March 24, 2016
©ESO 2016

The (w)hole survey: an unbiased sample study of transition disk candidates based on Spitzer catalogs

N. van der Marel[1,2], B.W. Verhaar[1], S. van Terwisga[1], B. Merín[3], G. Herczeg[4], N.F.W. Ligterink[1], and E.F. van Dishoeck[1,5]

[1] Leiden Observatory, Leiden University, P.O. Box 9513, 2300 RA Leiden, the Netherlands
[2] Institute for Astronomy, University of Hawaii, 2680 Woodlawn Drive, Honolulu HI 96822, USA
[3] European Space Astronomy Centre (ESA), P.O. Box 78, 28691 Villanueva de la Cañada, Spain
[4] Max-Planck-Institut für Extraterrestrische Physik, Giessenbachstrasse 1, 85748 Garching, Germany
[5] Kavli institute, Peking University, Beijing, China

2016

arXiv:1603.07255v1 [astro-ph.EP] 23 Mar 2016

ABSTRACT

Understanding disk evolution and dissipation is essential for studies of planet formation. Transition disks, i.e., disks with large dust cavities and gaps, are promising candidates of active evolution. About two dozen SED-selected candidates have been confirmed to have dust cavities through millimeter interferometric imaging, but this sample is biased towards the brightest disks. The *Spitzer* surveys of nearby low-mass star forming regions have resulted in more than 4000 Young Stellar Objects (YSOs). Using color criteria we have selected a sample of ∼150 candidates, and an additional 40 candidates and known transition disks from the literature. The *Spitzer* data were complemented by new observations at longer wavelengths, including new JCMT and APEX submillimeter photometry, and *WISE* and *Herschel*-PACS mid and far-infrared photometry. Furthermore, optical spectroscopy was obtained and stellar types were derived for 85% of the sample, including information from the literature. The SEDs were fit to a grid of RADMC-3D disk models with a limited number of parameters: disk mass, inner disk mass, scale height and flaring, and disk cavity radius, where the latter is the main parameter of interest. A large fraction of the targets possibly have dust cavities based on the SED. The derived cavity sizes are consistent with imaging/modeling results in the literature, where available. Trends are found with $L_{\rm disk}/L_*$ and stellar mass and a possible connection with exoplanet orbital radii. A comparison with a previous study where color observables are used (Cieza et al. 2010) reveals large overlap between their category of planet-forming disks and our transition disks with cavities. A large number of the new transition disk candidates are suitable for follow-up observations with ALMA.

Key words. protoplanetary disks - planets and satellites: formation - planet-disk interactions

1. Introduction

A central question in planet formation is how the optically thick protoplanetary disks around classical T Tauri stars evolve into the optically thin debris disks around older systems (Williams & Cieza 2011). An important part of the evolution occurs in the transitional phase between these two regimes. Transitional disks, disks with inner dust cavities, are considered to form the evolutionary link, although it remains uncertain whether all disks go through this phase at some point during their lifetime (e.g. Cieza et al. 2007; Currie & Kenyon 2009). One of the most exciting explanations for transition disks is the presence of a young planet that has cleared out its orbit (Lin & Papaloizou 1979). This scenario has been confirmed through the (tentative) detection of planets embedded in transition disks through direct imaging for a handful of disks (Kraus & Ireland 2012; Quanz et al. 2013; Reggiani et al. 2014; Quanz 2015; Sallum et al. 2015). As it remains unclear how and at what stage planets are formed in a disk, finding them at the earliest stage and study of their environment can provide important clues on the planet formation process. For a better understanding of the role of transition disks in the disk evolution and planet formation process, a large unbiased sample of transition disks with large holes should be studied.

The transition disk fraction is thought to be 5%-25% depending on the definition, and with the fraction varying with stellar age (Currie & Sicilia-Aguilar 2011), implying that the evolutionary path through a transition disk is either rapid or uncommon. Transitional disk candidates are traditionally identified through a deficit of infrared flux in the mid-IR spectral energy distribution (SED) (e.g. Strom et al. 1989; Calvet et al. 2002; Espaillat et al. 2014, for review). The deficit arises from the absence of hot small dust particles close to the star, which can be caused by either grain growth (e.g. Dullemond & Dominik 2005), photoevaporative clearing (e.g. Alexander et al. 2006) or interaction with a stellar companion or recently formed planet (e.g. Artymowicz & Lubow 1994), all processes closely linked to disk evolution. Thanks to *Spitzer* mid-infrared spectroscopy surveys, a large number of transitional disks has been discovered through a minimum in the infrared part of their SED (e.g. Brown et al. 2007; Najita et al. 2007; Kim et al. 2009; Merín et al. 2010). Submillimeter observations of about two dozen of the brightest disks have directly resolved large holes with pioneering interferometers, confirming their transition disk status (e.g. Piétu et al. 2005; Brown et al. 2008, 2009; Isella et al. 2010a,b; Andrews et al. 2011). The hole sizes generally match well with estimates from SED modeling, suggesting that the current interpretation and modeling of SEDs can correctly infer this parameter provided that the mid-infrared

part of the SED is well covered observationally. The Atacama Large Millimeter/submillimeter Array (ALMA) has produced even sharper dust images of a small sample of transition disks with evidence for dust trapping (van der Marel et al. 2013; Casassus et al. 2013; Pérez et al. 2014; Zhang et al. 2014). ALMA has also revealed the gas distribution through CO observations, showing that substantial amounts of gas are present inside the dust cavities (Bruderer et al. 2014; van der Marel et al. 2015; Perez et al. 2015; van der Marel et al. 2016) indicating the presence of planets. However, ALMA has so far focused on the most well-studied and brightest transition disks. A larger sample is required to derive a more general picture.

Transition disk candidates have historically been identified through a range of different criteria (Brown et al. 2007; Muzerolle et al. 2010; Oliveira et al. 2010; Merín et al. 2010; Cieza et al. 2010, 2012b; Romero et al. 2012), usually involving the Spitzer colors in the (mid) infrared. The availability of *Spitzer* IRS spectra between 5-35 μm was crucial for classification and determination of the hole size in these studies especially in covering the 8-20 μm region where the SEDs reach their minimum but which is not well covered by the 8 and 24 micron photometry points. In recent years, far infrared *Herschel* PACS and SPIRE photometry has been used to identify and characterize (transition) disks (e.g Ribas et al. 2013; Bustamante et al. 2015; Rebollido et al. 2015). Other studies identified candidates by comparing the infrared part of their SEDs with the 'median' T Tauri disk SED (e.g. Harvey et al. 2007; Merín et al. 2008). These studies define a separate class of transition disks as 'anemic' disks: disks with homologous depletion of dust due to grain growth or settling at all radii, exhibiting a low infrared excess at all wavelengths. Furthermore, some studies distinguish between pre-transitional and transitional disks: disks with a gap (inner disk present inside the cavity) and disks with a hole (Espaillat et al. 2007) although there is no obvious evolutionary connection. A 'cold disk' (Brown et al. 2007) refers to a transition disk with a strong deficit in the mid infrared, implying a cavity with a steep inner wall. Note that a few transition disks have been found in millimeter imaging without evidence for mid infrared dips in their SED, e.g. MWC 758 (Isella et al. 2010b)

Selection of candidates is sometimes followed up by radiative transfer modeling of the radial disk structure, to constrain the dust cavity size and disk mass (Kim et al. 2009; Merín et al. 2010) to determine the origin of the cavity besides clearing by a companion. Increased grain growth in the inner part of disk would result in the appearance of a dust deficit in the SED (Dullemond & Dominik 2005), although this would not be visible in millimeter imaging (Birnstiel et al. 2010). Furthermore, multiplicity studies can define the origin of the cavity as circumbinary disk whereas measuring the accretion through optical Hα can determine photoevaporative clearing (Najita et al. 2007; Espaillat et al. 2007; Cieza et al. 2010). Theoretical work has also shown that photoevaporative clearing cannot explain the largest observed cavities and a combination of processes may be responsible (Owen & Clarke 2012; Rosotti et al. 2013).

Overall, the definition of a transition disk candidate remains loose and has been used in various contexts in different studies. Due to lack of a large sample of transition disks, general properties remain uncertain and it is still unclear whether the origin for all transition disk cavities is the same, or whether disks follow different evolutionary paths (Cieza et al. 2007). Also, the distribution of cavity radii is not known, while this could constrain the birth sites of giant planets before migration. The analysis of a large unbiased sample of transition disks and candidates can provide firm constraints on their general properties. *Spitzer* surveys in all nearby (<500 pc) star-forming regions (Cores to Disks (c2d), Gould-Belt (GB) and Taurus) have provided identification and SEDs of several thousands of Young Stellar Objects (YSOs) (e.g. Evans et al. 2009; Rebull et al. 2010; Dunham et al. 2015, and references therein), out of which many transition disk candidates. In addition, in recent years the AllWISE catalog with mid infrared targets has become available (Wright et al. 2010), and the *Herschel Space Observatory* (Pilbratt et al. 2010) has observed large parts of nearby star forming regions in the far infrared. Due to the availability of *Spitzer* data combined with WISE and *Herschel* data, the timing is perfect for a large transition disk SED survey.

In this work, we analyze transition disk candidates selected from the *Spitzer* catalogs using robust color criteria developed by Merín et al. (2010). These criteria were developed after deep analysis of the SEDs including IRS spectra. Our sample is complemented by additional candidates and known transition disks from the literature. The SEDs are complemented with optical, new archival far infrared *Herschel*, *Spitzer* IRS spectra (where available) and new submillimeter observations and are modeled using the dust radiative transfer code RADMC-3D with a generic disk structure with a cavity. The main parameter of interest is the cavity size $r_{\rm cav}$. In Section 2 we discuss the selection criteria of the sample and the additional observations, Section 3 presents the results of the observations, Section 4 discusses the modeling procedure and limitations and the resulting disk parameters and in Section 5 we discuss the robustness of the sample and comparison with previous studies. One of the aims of this study is to define a large sample of transition disk candidates with dust cavities that are large enough to be imaged in the future by ALMA ($\geq$10 AU or ~0.03", for the largest distances). The resolved images of gas and dust will provide more clues on the origin of the dust cavities and the place of transition disks in disk evolution.

2. Observations

2.1. Target selection

The c2d, GB and Taurus *Spitzer* Legacy programs completed full infrared surveys using the Infrared Array Camera (IRAC; 3.6-8.0 μm) and Multiband Imaging Photometer (MIPS; 24-160 μm) in the nearby star-forming regions ($\leq$450 pc), resulting in more than 3000 identified YSOs (see Table 1 for an overview of papers presenting the data). Several bright YSOs from the c2d survey were targeted for additional observation with the *Spitzer* InfraRed Spectrograph (IRS; 5-35 μm). Merín et al. (2010, hereafter M10) analyzed 35 possible transition disk candidates for which IRS spectra were available in detail through SED modeling, and defined two sets of color criteria:

$$\begin{aligned}[\mathrm{A}] : 0.0 < [3.6] - [8.0] < 1.1;\\ 3.2 < [8.0] - [24.0] < 5.3;\end{aligned} \quad (1)$$

$$\begin{aligned}[\mathrm{B}] : 1.1 < [3.6] - [8.0] < 1.8;\\ 3.2 < [8.0] - [24.0] < 5.3;\end{aligned} \quad (2)$$

where the bracketed numbers refer to the magnitudes at the *Spitzer* wavelengths. The Region A criteria select 'clean' inner holes (disks for which there is no substantial excess in any IRAC band and there is a clear signature of an inner dust hole) and the Region B criteria select disks with a clear signature of an inner dust hole, but some excess in the IRAC bands, possibly resulting from an inner disk. The latter criterion includes several of the confirmed imaged transition disks (Brown et al. 2009;

Table 1: Overview Spitzer papers of YSOs in star forming regions

Cores to Disks (c2d)		d (pc)	Paper
Ophiuchus (MIPS)	Padgett et al. (2008)	120	VII
Serpens	Harvey et al. (2007)	250-400[a]	IX
Cham II	Alcalá et al. (2008)	180	X
Lupus I,III,IV	Merín et al. (2008)	150-200	XI
Perseus	Young et al. (2015)	250	XII
WTTS (c2d)	Padgett et al. (2006); Cieza et al. (2007); Wahhaj et al. (2010)	-	
Disks with holes (c2d)	Merín et al. (2010)	-	
Gould Belt (GB)			
IC5146	Harvey et al. (2008)	950	I
Cepheus	Kirk et al. (2009)	300	II
CrA	Peterson et al. (2011)	150	III
Lupus V & VI (full)	Spezzi et al. (2011)	150	IV
Ophiuchus North	Hatchell et al. (2012)	120	V
Auriga	Broekhoven-Fiene et al. (2014)	450	VI
Others			
η Cham (IRAC)	Megeath et al. (2005)	97	
η Cham (MIPS)	Sicilia-Aguilar et al. (2009)	97	
Cham I	Luhman et al. (2008)	160	
Taurus	Rebull et al. (2010); Luhman et al. (2010)	140	
λ Orionis	Hernández et al. (2010)	450	
Orion	Megeath et al. (2012)	450	
FEPS	Carpenter et al. (2008)	-	

Notes. [(a)] The distance to Serpens is uncertain, but recent VLBA observations put it at 415 pc (Dzib et al. 2011), which has been used in this study.

Andrews et al. 2009), but may also include some disks without holes (M10).

M10 finds one transition disk with a particularly large hole (Sz 84, object 17), which falls outside of the color criteria mentioned above. Inspection of its SED reveals a steep slope between the 24 μm and 70 μm flux. Therefore we set an additional color criterium:

$$\begin{aligned}&[\mathrm{L}] : 0.0 < [3.6] - [8.0] < 1.1;\\ &\quad 10.0 > [24.0] - [70.0] > 3.8;\end{aligned} \tag{3}$$

In this case the MIPS-2 flux at 70 μm has to be detected rather than an upper limit. Due to the large beam size of *Spitzer* at 70 μm of 18", this flux can be confused with nearby sources. The long wavelength flux thus has to be taken with extra care for the Region L criteria. The Region L targets are not mutually exclusive with the Region A criteria: some targets follow in both.

The color criteria were applied to the three main *Spitzer* catalogs, listed in Table 2, resulting in 153 candidates. In addition to the catalogs, we searched the literature for additional transition disk candidates, by using the color criteria on *Spitzer* targets that were not included in the catalogs (row 'Other' in Table 2), finding an additional 12 disks. Targets in Orion, Cepheus (Kirk et al. 2009) and IC 5146 (Harvey et al. 2008) are not included due to their large distances (450, 500 and 950 pc respectively). Finally, we added 7 confirmed transition disks known from resolved millimeter imaging and 21 targets that were marked as transition disk candidate by various authors, but were not yet included by the color criteria. The number of targets from various selections are listed in Table 2 with corresponding references. All targets in the sample are listed in Table A.1. Several of the color-selected targets have been identified as transition disk candidates or confirmed by millimeter imaging, as indicated in the last column of Table A.1.

The distance to Serpens is uncertain, with values between 250 and 400 pc (discussion in e.g. Oliveira et al. 2009). However, VLBA observations have set a distance of 415 pc for the Main Cloud (Dzib et al. 2010), which has been used in more recent work (Erickson et al. 2015; Ortiz-León et al. 2015), and has also been used in this study.

Table 2: Target selection in each catalog

Catalog/Criterion	[A]	[B]	[L]
c2d (Evans et al. 2009)	30	34	9
GB (Dunham et al. 2015)	25	15	31
Taurus (Rebull et al. 2010)	7	12	6
Other samples[a]	7	4	1
Additional targets[b]	7 imaging 21 SED		

Notes. [(a)] Targets were selected using our color criteria in the following papers, for targets not included in the c2d/GB/Taurus catalogs: Padgett et al. (2006); Silverstone et al. (2006); Carpenter et al. (2008); Luhman et al. (2008); Kim et al. (2009); Sicilia-Aguilar et al. (2009); Cieza et al. (2010); Luhman et al. (2010) [(b)] Some targets were added from the literature that did not follow the color criteria. Imaging targets were taken from Piétu et al. (2006); Ohashi (2008); Brown et al. (2009); Isella et al. (2010a); Andrews et al. (2010, 2011); Rosenfeld et al. (2013); van der Marel et al. (2013). The other targets were identified as transition disk candidate by Megeath et al. (2005); Hernández et al. (2007); Merín et al. (2008); Monnier et al. (2008); Hughes et al. (2008); Sicilia-Aguilar et al. (2008); Ireland & Kraus (2008); Kim et al. (2009); McClure et al. (2010); Najita et al. (2010); Espaillat et al. (2011); Furlan et al. (2011)

2.2. Additional photometry

For each target, an SED was constructed using the *Spitzer* IRAC and MIPS photometry, complemented with optical B, V and R data from the NOMAD catalog (Zacharias et al. 2005) and near infrared J, H and K photometry from 2MASS (Cutri et al. 2003). Reduced *Spitzer* IRS low-res spectra of 5-35 μm were taken from the Cornell Atlas of Spitzer/IRS Sources (CASSIS) (Lebouteiller et al. 2011) when available. For ID63 (DoAr28), the IRS spectrum in CASSIS included extended emission, a properly reduced spectrum was kindly provided by Melissa McClure (McClure et al. 2010). Unfortunately IRS spectra are not available for the entire sample, while colors only provide limited constraints on the derived cavity size. Bright isolated targets could be complemented with *IRAS* photometry, especially when *Spitzer* data were saturated. The *Wide-field Infrared Survey Explorer (WISE)* performed an all sky survey in four wavelength bands: 3.4, 4.6, 12.0 and 22 μm leading to the AllWISE Source catalog (Wright et al. 2010). The coordinates of the targets in our sample were matched with the WISE targets (within 2") and the fluxes were added to the SEDs. Although 3 of the 4 bands overlap with *Spitzer*, the 12 μm flux provides an important data point in between IRAC and MIPS wavelengths when no IRS spectra are available. Furthermore, the diffraction limited beam size of the *WISE* satellite is twice as large as the *Spitzer* beam (see Table 3). The comparison between the *WISE* 22 μm flux with the MIPS-1 24 μm flux gives an independent check of confusion at longer wavelengths: if the 22 μm flux is much larger, there is likely a nearby source that will confuse 70 μm MIPS-2 flux as well. Although the *Spitzer* c2d and GB catalogs provide a quality flag on the MIPS-2 flux (MP2_Q_det_c) for possible confusion, this independent alternative check showed more directly which targets were confused at longer wavelengths. A difference between the 22 and 24 μm flux could also originate from infrared variability, for example due to scale height changes in the inner disk (e.g. Flaherty & Muzerolle 2010; Espaillat et al. 2011). However, such variability is typically on the order of 20-40%. Therefore, we only consider confusion if the difference in flux is more than 50%. The fluxes of different telescopes are taken with years in between, so without infrared monitoring there is no possibility to quantify this effect for the targets in our sample, but the effect on our SED modeling is expected to be minor. The following targets were removed from the sample due to possible confusion and their SEDs were not further analyzed: IDs 30, 32, 82, 85, 86, 88, 90, 92, 93, 95, 97, 98, 116, 123, 126, 202, 346 and 347.

Table 3: Beam sizes and apertures for photometry

Telescope	Instrument	Wavelength range (μm)	Beam size/ Aperture(")
Spitzer	IRAC	3.6,4.5,5.8,8.0	1.7–1.9
	MIPS	24.0,70.0	6.0,18
WISE		3.4,4.6,12,22	6.1,6.4,6.5,12
Herschel	PACS	70,100,160	5.5,6.5,11
APEX	SABOCA	350	7.8
	LABOCA	870	19
JCMT	SCUBA-2	850	15

At longer wavelengths, the SEDs were complemented with (sub)millimeter data from the literature where available (see refs in Table C.1). A subsample of the remaining targets were observed with the James Clerk Maxwell Telescope (JCMT) [1] and the Atacama Pathfinder Experiment (APEX) [2]. Targets were selected on their expected submillimeter brightness considering their 70 μm flux (brighter than ~140 mJy). The details of these observations are discussed in Section 2.3.

The SEDs were further complemented with far infrared fluxes from the *Herschel* Space Observatory (Pilbratt et al. 2010). The data reduction is discussed in Section 2.4.

2.3. Submillimeter observations

Observations of 32 of our targets were taken with the SABOCA and/or LABOCA instruments at the APEX telescope at the Chajnantor plateau in Chile. Observations were taken in service mode in 2012 and 2013 in ESO programs 089.C-0940, 090.C-0820 and 091.C-0822 and Max Planck programs M0010_88 and M0003_90. SABOCA is a 39-channel bolometer array operating at 350 μm (Siringo et al. 2010), LABOCA is a 295-channel bolometer array at 870 μm (Siringo et al. 2009). Imaging was performed in wobbler on-off mode. For a few sources, imaging was also performed in mapping mode (map size 1.5') to check the pointing and to check for extended emission. One source (MP Mus, ID20) was observed with the new ArTeMiS camera in mapping during its commissioning phase, operating at 350 μm (Revéret et al. 2014). Integration times were 5-40 minutes on source. The data were reduced using the CRUSH software (Kovács 2008) and (for the wobbler observations) verified using the BoA software (Schuller 2012). The results from both reduction techniques were found to agree within error bars and the CRUSH results are reported in Table 4. Flux calibration uncertainties (not included in Table 4) are typically 10% for LABOCA and 25-30% for SABOCA.

Observations of 41 of our targets were taken with the SCUBA-2 instrument at the JCMT telescope at Mauna Kea, Hawaii. Observations were taken in service mode in 2012 and 2013 in programs M12AN07, M12BN13 and M13AN01. SCUBA-2 is a 10,000 pixel bolometer camera operating simultaneously at 450 and 850 μm (Holland et al. 2013). Imaging was performed in the smallest possible map size (Daisy 3' pattern). Observations were taken in grade 3-5 weather, which is generally insufficient for observing at 450 μm, so only the 850 μm data are considered. Integration times were 5-50 minutes on source. The data were reduced using the default online pipeline. The resulting FITS images were inspected by eye for extended emission and fluxes and noise levels were derived. The noise levels were estimated by measuring the standard deviation in the map, after subtraction of point sources. The results are reported in Table 5. The flux calibration uncertainty (not included in Table 5) is typically 10% for SCUBA-2.

2.4. Herschel observations

We have searched the *Herschel* Science Archive for observations with the PACS broadband photometer (Poglitsch et al. 2010) at

[1] The James Clerk Maxwell Telescope has historically been operated by the Joint Astronomy Centre on behalf of the Science and Technology Facilities Council of the United Kingdom, the National Research Council of Canada and the Netherlands Organisation for Scientific Research. Additional funds for the construction of SCUBA-2 were provided by the Canada Foundation for Innovation.

[2] This publication is based on data acquired with the Atacama Pathfinder Experiment (APEX). APEX is a collaboration between the Max-Planck-Institut fur Radioastronomie, the European Southern Observatory, and the Onsala Space Observatory.

the coordinates of all targets in the sample. In photometry mode, PACS observes simultaneously at either 70 (PACS blue) and 160 μm (PACS red) or 100 (PACS green) and 160 μm. Therefore, targets are recovered in either two or three of these wavelength bands. Only data products of reduction level higher than 2.0 were used, using the high pass filter.

Photometry of the PACS data was performed using the *annularSkyAperturePhotometry*-task in the Herschel Interactive Processing Environment (HIPE), version 12.1.0. This task derives background-corrected fluxes from point sources by comparing the flux inside a region centered on the point source and an annulus around it. We used the values for the aperture and annulus radii as used by Ribas et al. (2013). The background was estimated using the DAOPhot algorithm. Errors were estimated manually at several positions near the source position, to avoid including nearby extended emission originating from clouds. The presence of nearby clouds is indicated in Table D.1. The flux calibration uncertainty (not included in Table D.1) is typically 5% for PACS photometry.

2.5. Optical spectroscopy

Stellar properties such as the spectral type must be determined to correct for the extinction and deredden the SED flux points. The stellar luminosity is required to understand and interpret the SEDs properly. For about half of the targets in the sample, spectral types are available from the literature. The targets without known spectral type were observed with optical spectroscopy.

Optical spectra were taken for 90 targets, including reobservation of 24 targets for which the literature spectral type was still uncertain. We obtained low resolution optical spectra with the Intermediate dispersion Spectrograph and Imaging System (ISIS) on the William Herschel Telescope [3] from 4-8 August 2012. The D5700 dichroic splits the light at 5700 Å into red and blue channels. The red emission then passes through the GG495 filter and is dispersed by the R158R grating to generate spectra from 5600–10000 Å at $R \sim 1200$. The blue emission is dispersed by the R300B grating to generate spectra from 3200–5800 Å at $R \sim 1800$.

R magnitudes ranged between 9 and 19 mags, requiring integration times between 1 and 60 minutes. The slit width was set each night depending on the seeing.

The spectra were reduced with custom written codes in IDL, including flatfield and cosmic ray corrections. The wavelength calibration was obtained from arc lamp spectra. An initial flux calibration was performed with observations of spectrophotometric standards G191 B2B, EG 274, G93-48, and LTT 6248, repeated several times each night (Oke 1990; Hamuy et al. 1992)

The spectral types of stars in our sample were estimated following the approximate method described by Herczeg & Hillenbrand (2014), based on the spectral compilation by Pickles (1998) at early spectral types and Luhman (e.g. 2004) for late K and M dwarfs. For K and M stars with accretion, the spectral types estimates include a rough correction for veiling from the accretion continuum. The spectral types are estimated to be accurate to a few subclasses at spectral types earlier than K5 and 0.5-1 subclass for late K and M stars. The Hα line equivalent width was calculated by fitting a Gaussian profile to the line.

[3] The William Herschel Telescope is operated on the island of La Palma by the Isaac Newton Group in the Spanish Observatorio del Roque de los Muchachos of the Instituto de Astrofísica de Canarias.

3. Results

3.1. Stellar parameters

Spectral types as derived from our observations and taken from the literature are given in Table A.2. The observations of previously characterized stars resulted generally in the same spectral types as derived before. Some of the WHT-ISIS targets did not show any lines and no spectral type could be determined: 19002346-3712242 (ID32), ISO-Oph43 (ID47), 18294721-0148301 (ID101), J182821.6+000016 (ID112), 18392594+0006382 (ID114), serp22 (124), 18401205+0029276 (ID125), Serp111 (ID131), J034219.3+314327 (ID164), J034345.17+320358.6 (ID202) and J162715.89-243843.2 (ID204), these SEDs were fit assuming a K7 star. For these stars, the temperature of 4060 K is marked as (4060) in Table A.2. J18272873-0406248 (ID68), 18304127-0242335 (ID80), 18291450-0220575 (ID84), 18314110-0128035 (ID104), 18385989-0008097 (ID110), 18374209+0016519 (ID119), 18381580+0024218 (ID122) and 18381447+0035099 (ID129) turned out to be giants, these SEDs were not further analyzed. There may be additional contamination in the sample by giants, especially in Serpens. For a handful of targets, the spectral type could not be determined to subtype accuracy. This paper presents new spectral types for 85 targets. For our final sample, spectral types are known for ∼85% of our targets. The uncertainty in the spectral type of a few subclasses results in less than 0.2 dex uncertainty in the bolometric luminosity, which is sufficient for our purposes of modeling the SED with a simple disk structure.

Spectral types are converted to the effective temperature $T_{\rm eff}$ using the scales in Kenyon & Hartmann (1995). The extinction A_V and stellar luminosity L_* (or stellar radius R_*, as $L_* = 4\pi R_*^2 \sigma T^4$) are fit simultaneously to the SEDs, assuming the distances listed at the bottom of Table A.1. Kurucz models of stellar photospheres (Castelli & Kurucz 2004) are used as templates for the broadband emission. The 2MASS J-band and optical V and R band fluxes are taken as reference to constrain the fit, assuming no excess in these bands, and assuming no significant veiling or variability through accretion or extinction (Cody et al. 2014; Stauffer et al. 2014). When both V and R were missing, the extinction was estimated adopting $A_J = 1.53 \times E(J-K)$, where $E(J-K)$ is the observed color excess with respected to the expected photospheric color (Kenyon & Hartmann 1995), depending on its spectral type. The extinction law is parametrized as a function of wavelength assuming R_V=5.5 (Indebetouw et al. 2005) and scaled to the visual extinction A_V. The resulting values are listed in Table A.2. Stellar masses are derived by interpolation of evolutionary models of Baraffe et al. (1998) in the position of the target on the HR diagram, although these are only approximations due to the uncertainties in the spectral type. For targets that could not be fit by the Baraffe models (which only include stars up to 1 $M_\odot$), masses were derived using the evolutionary models by Siess et al. (2000). Since uncertainties in stellar age are large, they are not tabulated here. We note that for the Serpens targets an alternative distance of 250 pc as used in previous work would often result in very high age estimates (>10 Myr), confirming that the 415 pc used here is likely more accurate (also demonstrated in Oliveira et al. 2009, 2013). For 10 targets no stellar mass could be derived, suggesting that their derived stellar properties are uncertain. Most of these are targets without known spectral type or late M stars.

The presence or absence of accretion can be assessed from the strength and shape of emission of the Hα and other optical lines (e.g. White & Basri 2003; Natta et al. 2006). Although

a proper treatment of the accretion requires simultaneous fitting of extinction, luminosity and accretion through broadband spectroscopy (e.g. with X-shooter, Manara et al. 2014), as accretion also results in broadband UV/blue excess, the analysis in this study is limited to a simple designation of accretion by the width of the Hα line. We do not aim to quantify the accretion in terms of $M_\odot$ yr^{-1} due to the large uncertainties when deriving accretion from the line width only. Both the equivalent width EW[Hα] and the Hα 10% width have been used to distinguish between accretors and non-accretors, where the EW[Hα] cut-off depends on the spectral type (White & Basri 2003). Typically, a star is classified as an accretor if the Hα 10% width is >300 km s^{-1} (Natta et al. 2004), or if EW[Hα] > 3Å for an early-K star, > 10Å for a late-K star and > 20Å for an M star. Since other studies often only list the EW[Hα] values, our accretion designation is largely based on that.

In recent years, several YSOs have been analyzed with broadband high resolution spectroscopy, including some of the targets in our sample (e.g. Alcalá et al. 2014; Manara et al. 2014). This accretion information is preferred to that derived from the equivalent width as this method is more reliable, and those targets have been marked explicitly in Table A.2. Accretion properties are known for 84% of our sample: about 64% of these targets are accreting, the remaining targets show little or no signs of accretion.

3.2. Long wavelength photometry

The submillimeter photometry resulted in a total of 34 detections and 39 upper limits, listed in Table 4 and 5. In addition, we have taken (sub)millimeter photometry from the literature (see Table C.1). With 57 (sub)mm detections and 47 upper limits, about 50% of the targets in our sample have constraints at longer wavelengths.

Table 4: APEX photometry at 350 and 870 μm for our sample.

ID	$F_{350\mu m}$ (Jy)	$F_{870\mu m}$ (mJy)	ID	$F_{350\mu m}$ (Jy)	$F_{870\mu m}$ (mJy)
1	2.4 ± 0.2	210 ± 20	40	< 0.7	< 20
2	-	< 40	43	-	< 18
6	0.69 ± 0.18		46	0.8 ± 0.2	164 ± 14
9	-	< 15	55	< 0.9	92 ± 6
10	-	< 20	58	-	< 18
11	2.4 ± 0.5		62	< 0.6	62 ± 9
14	-	24 ± 6	95	-	49 ± 11
15	4 ± 0.2	420 ± 50	98	-	63 ± 8
16	9.8 ± 2.4		99	-	360 ± 30[a]
18	-	20 ± 6	132	-	109 ± 11[a]
20	-	390 ± 10	200	-	< 40
22	< 0.3		203	-	55 ± 10[a]
25	-	< 30	303	-	136 7
27	0.19 ± 0.04		307	-	123 ± 14
35	-	28 ± 4[a]	316	-	98 ± 13
36	0.22 ± 0.06[a]	< 30	321	-	< 20

Notes. [(a)] The flux is contaminated by extended emission near the source position.

Herschel PACS surveys cover 92% of our targets. The derived fluxes and upper limits are listed in Table D.1 and images of the cut out maps are given in Figure. For 152 targets at least one of the three wavelengths results in a detection. For 18 targets the emission is confused by cloud emission at all three wavelengths, for 27 only at 100 and 160 μm and for 62 targets only at 160 μm. For 25 of the targets without cloud confusion no flux is detected at any of the wavelengths.

Table 5: JCMT photometry at 850 μm for our sample

ID	$F_{850\mu m}$ (mJy)	ID	$F_{850\mu m}$ (mJy)
22	< 31	124	< 19
23	153	127	< 29
26	< 30	137	63 ± 18
29	31 ± 7	154	< 56
32	< 47	155	55 ± 18
36	73 ± 18	156	< 31[a]
44	38 ± 11	161	< 115
47	< 50	163	< 117[a]
56	< 59	166	167 ± 14
60	< 24	171	17 ± 6
63	95 ± 16	174	< 27
70	32 ± 11	178	222 ± 16
82	< 57	187	126 ± 18
86	< 107[a]	189	93 ± 16
88	< 137[a]	192	< 29
89	< 35	193	32 ± 9
92	< 79	196	69 ± 19
100	< 37	202	< 56
107	< 17[a]	333	< 56
113	< 18		
120	< 21		

Notes. [(a)] The flux is contaminated by extended emission near the source position.

The PACS 70 μm fluxes and upper limits are consistent with the MIPS-2 fluxes and upper limits. The PACS sensitivity is sometimes shallower than the MIPS-2, resulting in a higher upper limit. For some targets, a more thorough data reduction of the PACS data was performed in other work (Ribas et al. 2013; Olofsson et al. 2013; Bustamante et al. 2015). In Table 6 the derived fluxes and upper limits are compared. Our values are similar within errors with previous estimates, confirming the validity of our data reduction.

3.3. Disk parameters

Millimeter fluxes can be used to obtain a rough estimate of the disk mass (gas+dust) assuming optically thin dust emission and a gas-to-dust ratio of 100. Disk masses $M_{\rm disk,mm}$ in our sample are calculated following the relations presented in Cieza et al. (2008) with standard assumptions and parameters:

$$M_{\rm disk} = 0.17 \left(F_{1.3mm}({\rm mJy}) \times \frac{d}{140{\rm pc}}^2 \right) M_{\rm Jup} \quad (4)$$

$$M_{\rm disk} = 0.08 \left(F_{0.85mm}({\rm mJy}) \times \frac{d}{140{\rm pc}}^2 \right) M_{\rm Jup} \quad (5)$$

with F_λ the flux at wavelength λ and d the distance to the star. Using this relation, disk masses of our sample range between <0.4 and 168 $M_{\rm Jup}$, and an average disk mass of 14 Jupiter masses, similar to large millimeter studies of disks (e.g. Andrews & Williams 2007a). However, these disk masses remain highly uncertain as the vertical structure, cavities and the stellar radiation field are not taken into account and the dust opacities and gas-to-dust ratio are uncertain.

Furthermore, we derive $L_{\rm disk}$ for each target by integrating over all data points after subtraction of the fitted stellar photosphere. The ratio $L_{\rm disk}/L_*$ is a measure of disk processing,

Table 6: Comparison PACS photometry with previous estimates

ID	$F_{70\mu m}$ (Jy)		$F_{100\mu m}$ (Jy)		$F_{160\mu m}$ (Jy)		Ref
	This study	Previous	This study	Previous	This study	Previous	
4	< 0.1	< 0.08	< 0.07	< 0.14	< 0.41	< 1.10	1
5	0.18 ± 0.05	0.15 ± 0.02	0.17 ± 0.03	0.17 ± 0.04	< 0.33	< 1.07	1
6	3.11 ± 0.31	3.08 ± 0.46	2.90 ± 0.29	2.82 ± 0.42	2.15 ± 0.25	2.32 ± 0.35	1
7	0.21 ± 0.04	< 0.28	0.21 ± 0.03	0.21 ± 0.01	< 0.31	< 0.32	2
9	< 0.65	0.60 ± 0.09	< 0.71	0.77 ± 0.12	< 1.06	0.98 ± 0.15	1
11	3.86 ± 0.39	3.88 ± 0.58	3.80 ± 0.38	3.63 ± 0.54	3.65 ± 0.37	3.86 ± 0.58	1
12	0.44 ± 0.05	0.38 ± 0.06	0.40 ± 0.05	0.36 ± 0.06	< 0.39	0.20 ± 0.03	1
13	< 0.11	< 0.04	0.14 ± 0.03	< 0.07	< 0.55	< 0.85	1
14	0.69 ± 0.08	0.68 ± 0.10	0.55 ± 0.06	0.57 ± 0.09	0.41 ± 0.07	< 0.30 ± 0.05	1
15	1.58 ± 0.16	1.61 ± 0.24	2.31 ± 0.23	2.19 ± 0.33	2.80 ± 0.28	2.74 ± 0.41	1
16	26.06 ± 2.92	25.91 ± 3.88	36.06 ± 3.9	32.32 ± 4.85	38.45 ± 6.0	27.3 ± 4.10	1
17	0.21 ± 0.05	< 0.25	0.25 ± 0.03	0.23 ± 0.01	0.30 ± 0.09	0.28 ± 0.05	2
24	0.17 ± 0.04	0.07 ± 0.02	0.11 ± 0.03	0.10 ± 0.02	< 0.09	< 0.13	3
25	< 0.34	0.11 ± 0.03	< 0.32	0.16 ± 0.04	< 0.38	< 0.23	3
26	< 0.26	0.10 ± 0.02	< 0.12	0.18 ± 0.04	< 0.02	< 0.19	3
27	0.61 ± 0.07	0.51 ± 0.13	0.80 ± 0.08	0.68 ± 0.17	0.96 ± 0.17	0.72 ± 0.18	3
179	1.23 ± 0.13	1.04 ± 0.26	1.41 ± 0.14	1.26 ± 0.31	1.69 ± 0.19	1.57 ± 0.39	3
185	0.21 ± 0.06	0.17 ± 0.04	0.24 ± 0.05	0.23 ± 0.06	< 0.91	0.29 ± 0.07	3
200	0.48 ± 0.06	0.36 ± 0.09	0.37 ± 0.05	0.37 ± 0.09	0.47 ± 0.15	0.26 ± 0.07	3

Refs. 1) Ribas et al. (2013), 2) Olofsson et al. (2013), 3) Bustamante et al. (2015)

as it traces the total amount of dust that is reprocessing stellar light. As disks become more tenuous, settle and eventually disappear, $L_{\rm disk}$ is expected to decline. The majority of the disks have $0.001 < L_{\rm disk}/L_* < 0.4$, as expected for flared disks. Disks with $L_{\rm disk}/L_* < 10^{-3}$ are generally considered as debris disks (e.g. Wahhaj et al. 2010). On the other hand, targets with $L_{\rm disk}/L_* >> 1$ are either embedded Class I objects or edge-on disks which are more difficult to analyze (Merín et al. 2010). ID178 has $L_{\rm disk}/L_* \sim 17$ and is thus removed from the analyzed sample.

Both $L_{\rm disk}/L_*$ and $M_{\rm disk,mm}$ are listed in Table A.3. The final sample consists of 184 targets for which the SEDs will be analyzed.

4. Modeling

In order to determine the presence of a dust cavity and measure its size, the SEDs are modeled using the dust radiative transfer code RADMC-3D [4] (Dullemond & Dominik 2004). This code performs a Monte Carlo continuum radiative transfer calculation based on the input dust density profile and stellar photosphere, followed by raytracing of the SED. The model has a large number of input parameters and we have fixed as many as possible that are not important for our science goals. The model assumes a passive disk which reprocesses the stellar radiation field.

The modeling procedure consists of two steps: first using a rough grid with a broad range of parameters, followed by a finer grid for the specific stellar type. The modeling was performed blindly, without taking any results from previous SED modeling or imaging studies, for an uniform approach for each disk in this sample. In Section 5 the derived parameters are compared with previously found results.

4.1. Approach

The disks are modeled using a large grid of models, computed by RADMC-3D. The model assumes an axisymmetric gas surface density profile, following a radial power-law

$$\Sigma_g(r) = \mathrm{GDR} \cdot \Sigma_c \left(\frac{r}{r_c}\right)^{-1} \quad (6)$$

with r_c the characteristic radius and GDR the gas-to-dust ratio set to 100. The outer radius is set to 200 AU and the inner radius to the sublimation radius $r_{\rm sub}$ with $r_{\rm sub} = 0.07(L_*/L_\odot)^{1/2}$, assuming a sublimation temperature of 1500 K (Dullemond et al. 2001). The characteristic radius r_c is set to 25 AU. The dust density inside the cavity is parametrized by setting the density equal to zero between $r_{\rm gap}$ and $r_{\rm cav}$. The inner disk (between $r_{\rm sub}$ and $r_{\rm gap}$) is set by varying $\delta_{\rm dust}$ to fit the near infrared excess (see Figure 1). The $r_{\rm gap}$ is fixed to 1 AU as it can not be constrained well by the SED. A full disk without a cavity is simulated by setting $r_{\rm cav} = r_{\rm gap}$.

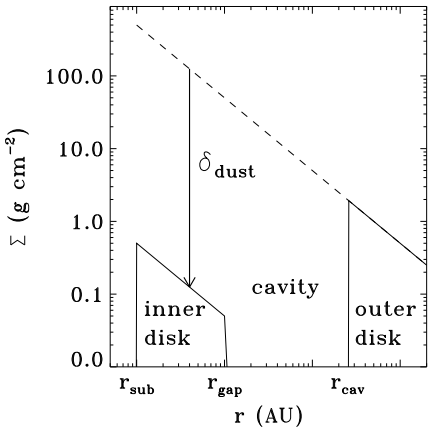

Fig. 1: Gas surface density profile used for the modeling, assuming a gas-to-dust ratio of 100.

The stellar photosphere in the model is described by its temperature and stellar luminosity, which has been fit independently

[4] www.ita.uni-heidelberg.de/~dullemond/software/radmc-3d/

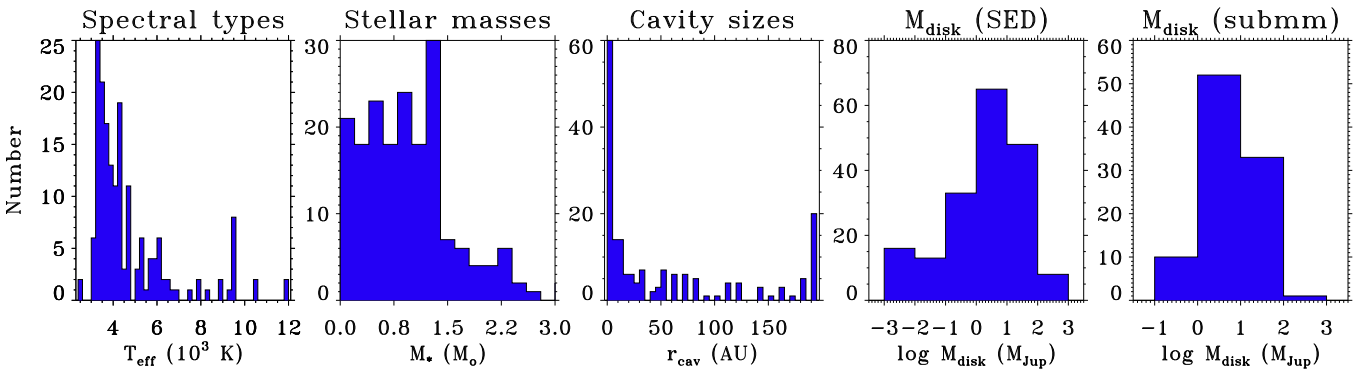

Fig. 2: Distribution of spectral types, stellar masses, cavity sizes and disk masses (derived from SED fitting and from submillimeter flux) in this study. The disk mass is calculated assuming a gas-to-dust ratio of 100.

together with the extinction. The disk is assumed to be flared, so that the vertical structure of the disk is described by

$$h(r) = h_c \left(\frac{r}{r_c}\right)^{\psi} \quad (7)$$

with h_c the scale height at r_c and ψ the flaring angle, which are both varied to fit the near and mid infrared part of the SED. As the scale height is degenerate with the cavity radius, the flaring angle is taken as a conservative value of either 1/7 or 2/7, following Chiang & Goldreich (1997). The derived cavity radius is thus likely a lower limit if the disk is flatter. With the inclusion of the *Herschel* fluxes, the scale height is better constrained than in previous SED modeling studies. Dust composition and settling is prescribed following Andrews et al. (2011), with a large and small dust grain population where the large grains have a lower scale height than the small grains. The inclination of the disks is taken as a constant of 30° and was not varied in the modeling, as only very high inclination angles (edge-on disks) result in a significant difference in the near infrared emission (and in addition, obscuration of the star). With our color criteria, edge-on disks are not expected to be included (Merín et al. 2010) and also the computation of the stellar masses from the stellar luminosities implies that most of the targets are not edge-on (although higher inclinations than 30° are still possible).

The five free parameters are thus $r_{\rm cav}$, $\delta_{\rm dust}$, Σ_c or disk mass, h_c and ψ, where $r_{\rm cav}$ is the main parameter of interest. Note that Σ_c represent the dust surface density. The fitting was performed in two steps. First, a large grid of models with a broad range of disk parameters and a limited number of stellar parameters was fit to each SED. Second, each SED was fine-tuned individually, using the exact stellar photosphere and starting from the best fit from the broad grid. The disk grids per object have a large range of cavity radii (our main parameter of interest), in combination with a small range of scale heights and disk masses. Although this approach is rather simple, results of SED modeling are known to be highly uncertain, especially for those targets without known spectral type, and the fitting results should only be considered as a first approximation of the structure. More detailed analysis and imaging data are required to fit individual targets more accurately.

In the fitting procedure, a χ^2 minimization was performed between the dereddened SED data points and the model SEDs. In the grid fitting, the data points were weighted by their excess above the stellar photosphere at each wavelength: fluxes at longer wavelengths got a larger weight than those in the optical and near infrared since the stellar photosphere is largely known from the extinction fitting. Uncertainties on the cavity radii are given in Table A.3, based on fits with up to 10% variation in χ^2.

4.2. Results

Each SED can be fit to a disk model, with the majority of disks containing a cavity. Table A.3 presents the results of the fitting procedure. Figure 2 presents the distribution of hole sizes and disk masses (assuming a gas-to-dust ratio of 100) of the full sample, showing a broad distribution of both parameters. The disk masses obtained from the fit generally agree within a factor of 2-3 with the mass estimate from the millimeter flux. During the fit procedure it became clear that certain disks have really large cavities (>100 AU) but very low scale heights, which can not be well reproduced by our flared models. These disks are likely debris disks, as also suggested by their low $L_{\rm disk}/L_*$ values. Recently, a sample of similar young WTTS disks were found to be gas-poor debris disks by ALMA observations (Hardy et al. 2015).

Figures B.1 to B.6 present the SEDs with the best fitting models overlaid. The SEDs are grouped into 5 different classifications:

- NH: Disks without holes ($r_{\rm cav}$=1 AU)
- LS: Low-mass disks with small holes ($r_{\rm cav}$ <10 AU, $M_{\rm disk} < 5M_{\rm Jup}$)
- LL: Low-mass disks with large holes ($r_{\rm cav}$ >10 AU, $M_{\rm disk} < 5M_{\rm Jup}$, $h_c > 0.01$)
- MS: Massive disks with small holes ($r_{\rm cav}$ <10 AU, $M_{\rm disk} > 5M_{\rm Jup}$)
- ML: Massive disks with large holes ($r_{\rm cav}$ >10 AU, $M_{\rm disk} > 5M_{\rm Jup}$)
- DD: Low-mass disks with large holes and very low scale heights ($r_{\rm cav}$ >100 AU, $M_{\rm disk} < 5M_{\rm Jup}$, $h_c \sim 0.01$)

For the disks classified as NH (no hole), we have excluded the targets that could be fit with a cavity >1 AU within the 10% χ^2 limit.

A large fraction of the disks (~23%) falls in the ML category of large holes in massive disks. It turns out that several of these disks are indeed the famous, bright disks with large inner holes known from imaging surveys (Andrews et al. 2011; Williams & Cieza 2011), confirming the strength of our SED modeling, even if rather simple. The new targets in the ML, MS

Table 7: Comparison cavity radii with literature values.

ID	Name	r_{cav}^{here}	r_{cav}^{lit}	Type[a]	Ref	ID	Name	r_{cav}^{here}	r_{cav}^{lit}	Type[a]	Ref
1	TCha	140^{+10}_{-10}	19	I	1	51	IRS48	120^{+10}_{-100}	60	I	13
3	RECX5	10^{+2}_{-2}	33	M	2	52	DoAr44	80^{+10}_{-20}	30	I	10
4	CHXR22E	45^{+15}_{-5}	7	M	3	54	SR21	60^{+20}_{-15}	36	I	8
6	CSCha	60^{+10}_{-10}	38	M	4	60	oph62	2^{+2}	3	M	6
9	T54	120^{+20}_{-10}	37	M	3	64	J160421	70^{+20}_{-30}	80	I	14
10	T21	190_{-10}	146	M	3	120	J182911	10^{+5}_{-8}	8	M	6
11	SZCha	30^{+10}_{-10}	29	M	3	127	Serp127	80^{+20}_{-10}	25	M	6
12	T35	15^{+5}_{-5}	15	M	3	128	J182935	25^{+45}_{-23}	7	M	6
14	T56	10^{+4}_{-4}	18	M	3	135	DMTau	4^{+2}_{-2}	18	I	10
15	CRCha	1^{+1}	10	M	4	136	UXTauA	50^{+40}_{-10}	25	I	10
18	T25	30^{+5}_{-5}	8	M	3	142	MWC758	25^{+15}_{-5}	73	I	10
21	HD142527	110^{+10}_{-20}	100	I	5	148	IPTau	100^{+10}_{-30}	2	M	4
24	Lup60	16^{+2}_{-4}	3	M	6	153	RYTau	2^{+2}	26[b]	I	15
27	Sz91	120^{+30}_{-20}	97	I	7	159	ABAur	1^{+4}	115	I	16
29	Sz84	70^{+40}_{-10}	55	M	6	161	ASR118	2^{+4}	1	M	6
33	HD135344	80^{+10}_{-10}	46	I	8	165	J034227	8^{+4}_{-4}	5	M	6
35	Sz76	2^{+2}	1	M	9	168	J034434	5^{+20}_{-3}	3	M	6
38	RXJ1615	10^{+10}_{-2}	30	I	10	169	IC348LRL190	2^{+2}	5	M	6
39	V4046Sgr	16^{+4}_{-6}	29	I	11	173	LkH-alpha330	120^{+10}_{-20}	68	I	10
45	SR24S	50^{+40}_{-20}	30	I	10	309	TWHya	10^{+2}_{-2}	4	M	17
46	RXJ1633	20^{+10}_{-5}	27	I	12	325	LkCa15	80^{+40}_{-35}	50	I	10
48	WSB60	8^{+6}_{-6}	15	I	10	326	CoKu-Tau-4	6^{+2}_{-2}	10	M	18
50	J162245	2^{+2}	1	M	6	329	GMAur	30^{+10}_{-5}	20	I	10

Refs. 1) Huélamo et al. (2015), 2) Bouwman et al. (2010), 3) Kim et al. (2009), 4) Espaillat et al. (2011), 5) Fukagawa et al. (2013), 6) Merín et al. (2010), 7) Canovas et al. (2015), 8) Brown et al. (2009), 9) Padgett et al. (2006), 10) Andrews et al. (2011), 11) Rosenfeld et al. (2013), 12) Cieza et al. (2012a), 13) van der Marel et al. (2013), 14) Mathews et al. (2012), 15) Isella et al. (2010a), 16) Piétu et al. (2005), 17) Andrews et al. (2012), 18) D'Alessio et al. (2005)
Notes.[a] M = derived from SED modeling, I = derived from millimeter imaging. [b] This value is not a real cavity size, but a transition radius: the disk was fit with a surface density profile that radially increases and decreases, peaking at 26 AU.

and some in the LL groups are promising disks for follow up observations with ALMA. Excluding the DD and NH disks, a total of 133 targets (72% of our analyzed sample) can be labeled as disks with cavities, transition disks. More than half of these (~ 70 targets) are new transition disks; about 40 had been imaged or modeled before and another 20 had been recognized as a possible transition disk. Of the new transition disks, two thirds have a known spectral type.

5. Discussion

The SED modeling has confirmed the presence of cavities in a large sample of transition disks. At least 72% of the sample could be modeled as a disk with a cavity, including about 110 new transition disks that had not been identified as transition disk before.

5.1. Comparison of cavity radii with literature values

In order to quantify the quality of our models, the fit results for the cavity size are compared with values from the literature from both SED modeling and resolved millimeter imaging in Table 7 and Figure 3. The cavity radii generally agree well within a factor of two with previously derived parameters. Especially the similarity to the imaging results is encouraging: this implies that a large number of our new targets are suitable for resolved imaging. Exceptions for the imaging targets are T Cha, RY Tau and AB Aur. For T Cha the overestimate of the cavity size could be caused by the assumed low inclination in our models: imaging has shown that the inclination is in reality ~ 67° so close to edge-on (Huélamo et al. 2015), affecting the near infrared emission from the inner disk. Also their flaring angle is lower than ours. For RY Tau, the cavity radius found by imaging is not defined in the same way as here: it is the peak of the mm dust surface density, assuming a surface density that first increases and then

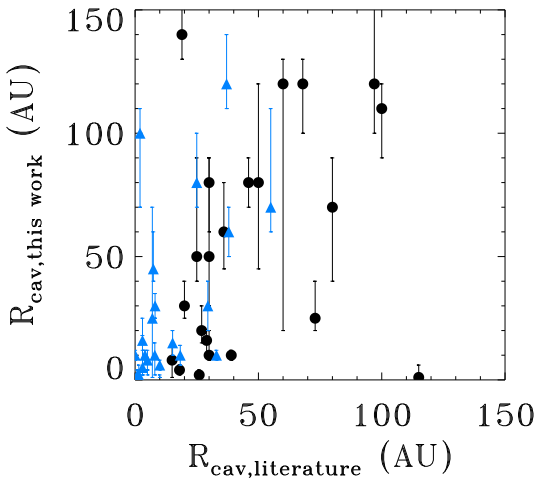

Fig. 3: Comparison derived cavity radii with literature values, based on Table 7. The black circles indicate the literature results from imaging, the blue diamonds from modeling.

Table 8: Multiplicity properties

ID	Name	Sep. (arcsec)	Sep. (AU)	r_{cav} (AU)	Ref	ID	Name	Sep. (arcsec)	Sep. (AU)	r_{cav} (AU)	Ref
1	TCha	0.062	6.7	140^{+10}_{-10}	1	60	oph62	<0.1	<12	2^{+2}	9
4	CHXR22E	<0.1	<16	45^{+15}_{-5}	2	62	J162218.5-232148	<0.1	<12	1	9
5	ISO52	<0.1	<16	30^{+50}_{-18}	2	63	DoAr28	<0.13	<16	20^{+5}_{-5}	10
6	CSCha	-	4	60^{+10}_{-10}	3	64	J160421.7-213028	<0.01	<1.5	70^{+20}_{-30}	11
7	11094742-7726290	<0.75	<120	8^{+2}_{-2}	4	134	RXJ0432.8+1735	<0.13	<18	190_{-10}	12
9	T54	0.25	40	120^{+20}_{-10}	2	135	DMTau	>0.03	>4	4^{+2}_{-2}	13
10	T21	0.14	22	190_{-10}	2	136	UXTauA	>0.03	>4	50^{+40}_{-10}	13
11	SZCha	<0.07	<11	30^{+10}_{-10}	2	140	043649.1+241258	<0.1	<14	190_{-10}	14
12	T35	<0.07	<11	15^{+5}_{-5}	2	149	V892Tau	0.06	8	10^{+8}_{-6}	15
14	T56	<0.07	<11	10^{+4}_{-4}	2	150	V410X-ray6	<0.1	<14	15^{+5}_{-5}	14
15	CRCha	<0.08	<13	1^{+1}	2	152	V819Tau	<0.1	<14	150^{+20}_{-20}	14
16	WWCha	<0.12	<19	50^{+30}_{-49}	2	153	RYTau	>0.03	>4	2^{+2}	13
17	11062554-7633418	<0.75	<120	15^{+15}_{-5}	4	162	MBO22	<0.1	<25	2^{+2}	14
18	T25	<0.08	<13	30^{+5}_{-5}	2	172	IC348-67	<0.1	<25	2^{+1}	14
21	HD142527	0.088	13	110^{+10}_{-20}	5	174	J04300424+3522238	<0.1	<45	18^{+10}_{-6}	14
23	Sz111	<0.7	<140	60^{+10}_{-10}	6	175	J04303235+3536133	0.83	116	4^{+8}_{-2}	14
24	Lup60	<0.1	<20	16^{+2}_{-4}	7	177	J04304004+3542101	1.2	168	25^{+10}_{-10}	14
25	J160830.3-390611	<0.8	<160	4^{+4}_{-2}	6	179	J160044.5-415531	<0.1	<15	1^{+59}	7
27	Sz91	<0.1	<20	120^{+30}_{-20}	7	180	J190058.1-364505	0.5	72	14^{+4}_{-4}	7
28	J160855.5-390234	<0.1	<20	2^{+2}	7	181	03445614+3209152	<0.1	<25	6^{+12}_{-5}	14
33	HD135344	<0.1	<14	80^{+10}_{-10}	8	182	03442156+3215098	<0.1	<25	2^{+23}	14
40	J163154.7-250324	<0.1	<12	1	9	183	03442257+3201536	<0.1	<25	4^{+1}_{-2}	14
41	J163205.5-250236	<0.1	<12	1	9	184	04330422+2921499	<0.1	<25	160^{+20}_{-10}	14
43	J163023.4-245416	<0.13	<16	45^{+5}_{-20}	10	191	042921.6+270125	0.22	30	2^{+2}	16
44	WSB63	<0.1	<12	4^{+2}_{-2}	9	200	J160710.08-391103.5	<0.06	<12	1	6
46	RXJ1633.9-2442	<0.1	<12	20^{+10}_{-5}	9	309	TWHya	<0.1	<5	10^{+2}_{-2}	8
47	ISO-Oph43	<0.13	<16	1^{+1}	10	318	DoAr21	-	1.5	70^{+30}_{-10}	17
48	WSB60	<0.1	<12	8^{+6}_{-7}	8	319	J162740.3-242204	0.638	80	1^{+17}	10
49	J163115.7-243402	0.33	41	20^{+30}_{-10}	9	325	LkCa15	>0.03	>4	80^{+40}_{-35}	13
50	J162245.4-243124	0.54	68	2^{+2}	9	326	CoKu-Tau-4	0.053	8	6^{+2}_{-2}	18
58	J162648.6-235634	<0.13	<16	1	10	329	GMAur	>0.03	>4	30^{+10}_{-5}	13
59	J162802.6-235504	<0.1	<12	2^{+2}	9						

Refs. 1) Huélamo et al. (2011), 2) Lafrenière et al. (2008), 3) Guenther et al. (2007), 4) Comerón (2012), 5) Biller et al. (2012), 6) Ghez et al. (1997), 7) Romero et al. (2012), 8) Vicente et al. (2011), 9) Cieza et al. (2010), 10) Ratzka et al. (2005), 11) Kraus et al. (2008), 12) Kohler & Leinert (1998), 13) Pott et al. (2010), 14) Cieza et al. (2012b), 15) Leinert et al. (1997), 16) Biller et al. (2011), 17) Loinard et al. (2008), 18) Ireland & Kraus (2008)

decreases with radius (Isella et al. 2010a). Therefore, the values can not be compared directly. For AB Aur, only a very small hole of at most 2 AU can be fit with our models, while millimeter imaging has revealed a large cavity of 115 AU at 1.4mm, with a complex, possibly spiral-arm structure (Piétu et al. 2005; Tang et al. 2012). As the AB Aur disk is still embedded in a envelope, the mid infrared emission is likely confused by cloud emission, which can explain this discrepancy between the SED and the millimeter image. The comparison with SED modeling shows large discrepancies for CHXR22E, T54, CR Cha and IP Tau. These targets were not modeled with a full radiative transfer code but a parametrized temperature profile and optically thin dust emission inside the cavity rather than an inner disk (Kim et al. 2009; Espaillat et al. 2011), so the results can not be compared directly.

5.2. Binaries

Some transition disks can be explained as circumbinary disks due to the dynamical interaction between the disk and a stellar companion. The cavity size is expected to be ∼2 times as large as the binary separation (Artymowicz & Lubow 1996). The fraction of the transition disks in our sample for which binarity has been studied is limited, but for those targets where spatially resolved information is available from the literature (either detections or upper limits), the properties are listed in Table 8, together with the cavity sizes found in this study.

Although for a handful of targets the cavity can indeed be explained by a binary companion, for the bulk of the disks the limits are not sufficient to exclude circumbinary disks. Previous binary studies of transition disks also revealed that most of the sharp cavities are not due to binary systems (Pott et al. 2010; Vicente et al. 2011).

5.3. Accretion

By combining the outcome of the SED modeling with our information on accretion, the possibility of photoevaporation as origin of the cavities can be checked. According to photoevaporation models (e.g. Alexander et al. 2006), UV photons from the star heat and ionize the gas in the disk; beyond a critical radius, the thermal velocity of the ionized gas exceeds its escape velocity and the material is dissipated as a wind. During the lifetime of the disk, the accretion rate is expected to gradually de-

crease: when the rate drops below the photoevaporation rate, the outer disk can no longer resupply the inner disk with material and an inner hole is formed. This process is called photoevaporative clearing, and transition disks created by this mechanism are expected to have no or very low accretion, although only disks with small inner cavities can be explained by this mechanism (Owen 2015). Clearing of a gap by a planet and photoevaporation could also happen simultaneously (e.g. Rosotti et al. 2013), making the distinction not purely measurable by accretion alone. Figure 4 shows the number of objects in each class that are accreting/non-accreting. The accretors are dominated by disks without holes and massive disks with large holes, which are likely transition disks with a cavity due to clearing by a companion. The non-accretors are dominated by the low-scale height low-mass disks (DD), confirming that they are likely debris disks. The non-accreting low-mass disks are possibly disks where the hole is caused by photoevaporative clearing, consistent with the so-called mm-faint disks (Owen & Clarke 2012; Owen 2015) in contrast with the mm-bright transitional disks. On the other hand, there are several low-mass accreting disks as well, so there is no general trend for the low-mass disks. The non-accreting disk without a hole (J034520.5+320634, ID171) is an outlier, but the equivalent width of this target is on the edge of accreting/non-accreting, probably due to the ubiquitous variable accretion (Mendigutía et al. 2012; Venuti et al. 2014), and should thus have been classified as an accretor.

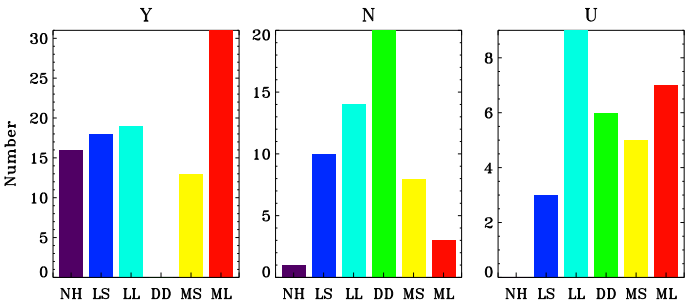

Fig. 4: Comparison of accretion properties from Table A.2 with disk hole parameters: Y means accreting, N means non-accreting, U means unknown.

5.4. Evaluation of color criteria

Considering the high success rate of new transition disks found in the sample in this study, it is now possible to re-evaluate the criteria used to select the targets. Figure 5 presents the the resulting classifications from our SED modeling for each of the four color selection criteria.

From Figure 5 it is clear that the disks without holes are most dominant in the B criteria, but overall at a low fraction. The L criteria are particularly biased towards the low scale height disks and low-mass disks with large holes. Massive disks with large holes are found in all colors. Evaluating the M10 criteria directly in the color-color plot, the DD disks fall outside the A and B range. A small amount of disks with holes falls outside the range of the A, B criteria (these are targets from the literature), generally with a shallower 8-24 μm slope.

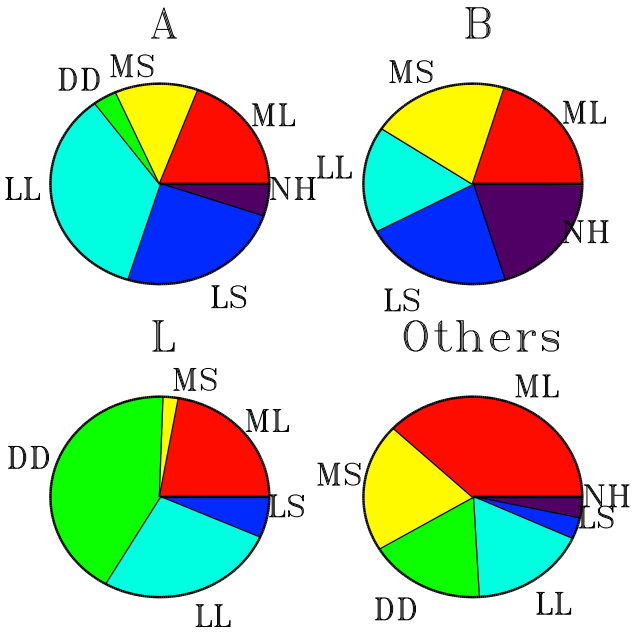

Fig. 5: Evaluation of the color criteria (Region A, B and L colors) vs the outcome of the SED modeling.

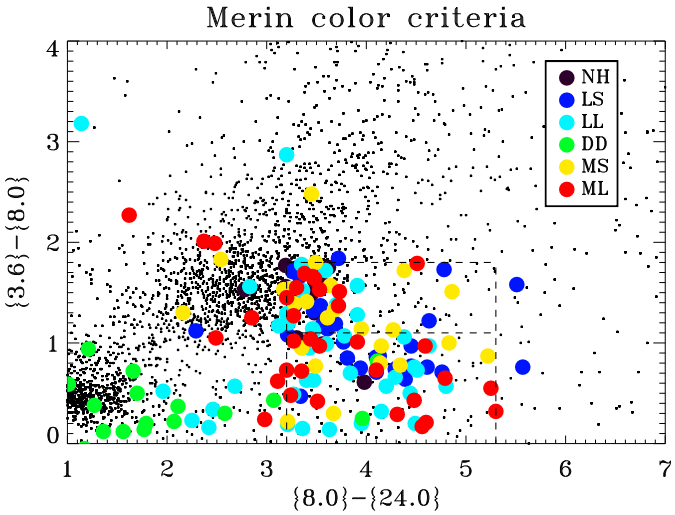

Fig. 6: Evaluation of the color criteria (A and B) vs the outcome of the SED modeling. The filled symbols are the targets analyzed in this study, the dots are all YSOs in the c2d, GB and Taurus catalogs. The dashed lines mark the Region B (top) and Region A (bottom) criteria.

5.5. Comparison with Cieza survey

A previous large survey of transition disk candidates was performed by Cieza et al. (2010, 2012b) and Romero et al. (2012), who selected a sample of candidates using their own color criteria. Rather than SED modeling, they apply criteria based on a range of observables (disk mass, $L_{\rm disk}/L_*$, accretion, multiplicity, infrared spectral slope $\alpha_{\rm excess}$ and the wavelength where the disk emission starts to dominate, $\lambda_{\rm turnoff}$) to determine the origin of the dust deficit in their disks: circumbinary disk, photoevaporative clearing, debris disk, grain growth or planetary clearing.

Of particular interest are their planet-forming disks, which are massive, accreting disks with sharp cavities ($\alpha_{\rm excess} > 0$). Their final target list is compared with our sample, and the colors

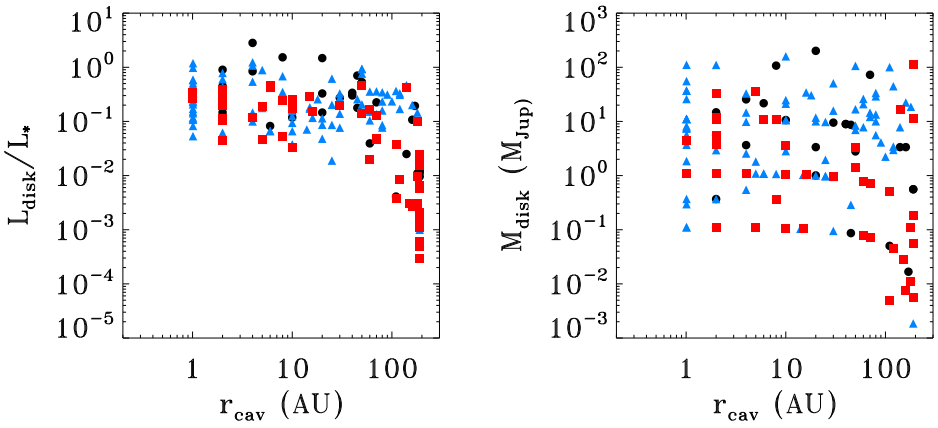

Fig. 10: The relation between cavity radius and $L_{\rm disk}/L_*$ and disk mass. Blue triangles indicate accretors, red squares non-accretors, black circles unknown.

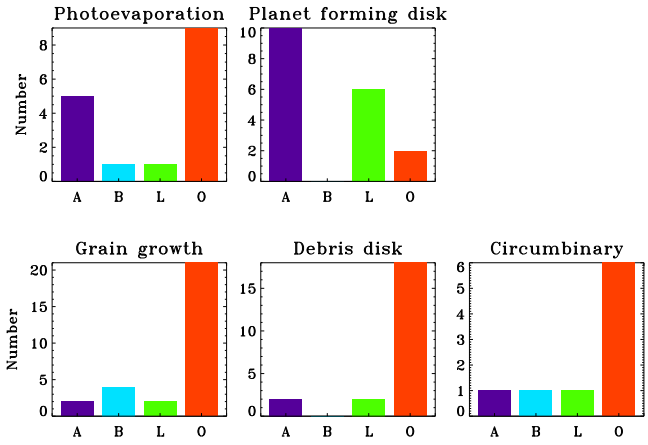

Fig. 7: Comparison of the categorization by the Cieza et al. studies with the color criteria used in this study applied to the 92 targets in the Cieza sample.

used for our color criteria have been derived for all their targets. Note that 27 of their 92 targets are already present in our sample, either selected by the color criteria or by their classification in the literature. Figure 7 shows how their categorization overlaps with our color criteria. Our A and L color criteria are clearly favored in the planet forming disks, while many of the less interesting disks from our perspective (grain growth, debris disks) fall in category, 'O', outside our color criteria. Several of the photoevaporation disks also follow the A criteria. This comparison confirms that our color criteria are good at selecting disks with sharp inner cavities.

Figure 8 shows the inital color selection of Cieza et al. ([3.6]-[4.5]<0.25, [3.6]-[24.0]>1.5) in comparison with the outcome of our classification. This Figure shows that only 50% of our disks with holes fall within these criteria. One of the reasons is that Cieza et al. have stricter constraints for their near infrared emission, which excludes the transition disks with strong near infrared excess (indicating an inner disk). The DD targets fall in the same quartile as the diskless stars, as expected.

Finally, Figure 9 shows how the classification of Cieza et al. compares with our classification for our targets. Note that we have included all our targets in the comparison, computing the values of $\alpha_{\rm excess}$ and $\lambda_{\rm turnoff}$ ourselves, in order to put them in the Cieza classification. Planet forming disks fall mostly within the class of massive disks with large cavities, while photoevaporation and debris disks are mostly consistent with low-mass disks. Neither of this is a surprise, considering the categorization of Cieza et al. (2010). Disks without holes all fall within the category of grain-growth disks. On the other hand, several other disks in the grain-growth category could be fit with a disk including a cavity. Note that circumbinarity is not well-constrained for most of our sample and therefore not included.

5.6. Evolution

The $L_{\rm disk}/L_*$ ratio is generally taken as a measure of disk evolution. For the targets in this study, there is a hint of a trend, with larger cavity radii and generally more non-accretors for lower $L_{\rm disk}/L_*$ (Figure 10a). This implies a general growth of cavity sizes with time while accretion decreases.

A relation between disk mass and cavity radius has been noted in previous studies and interpreted as a gravitational process, where larger disk masses produce more massive planets, clearing larger cavities (Merín et al. 2010). This study shows no trend between disk mass and cavity size. However, accretors are generally more massive than non-accretors (Figure 10b).

Both trends are susceptible due to the uncertainties in $r_{\rm cav}$ and biased due to the presence of many low-mass disks with large cavities in our sample, which are more likely to be debris disks than transition disks. When the DD disks are removed from the sample, there is barely a visible trend.

5.7. Cavity radii and exoplanets

If the origin of the dust cavity radii lies in forming planets, a connection should exist between the orbital radii of exoplanets and disk cavity radii according to planet-disk interaction models (Pinilla et al. 2012), unless planets migrate from their birth location. Planets are expected to clear cavities up to twice their orbital radius. We investigate this relation in Figure 11. Only

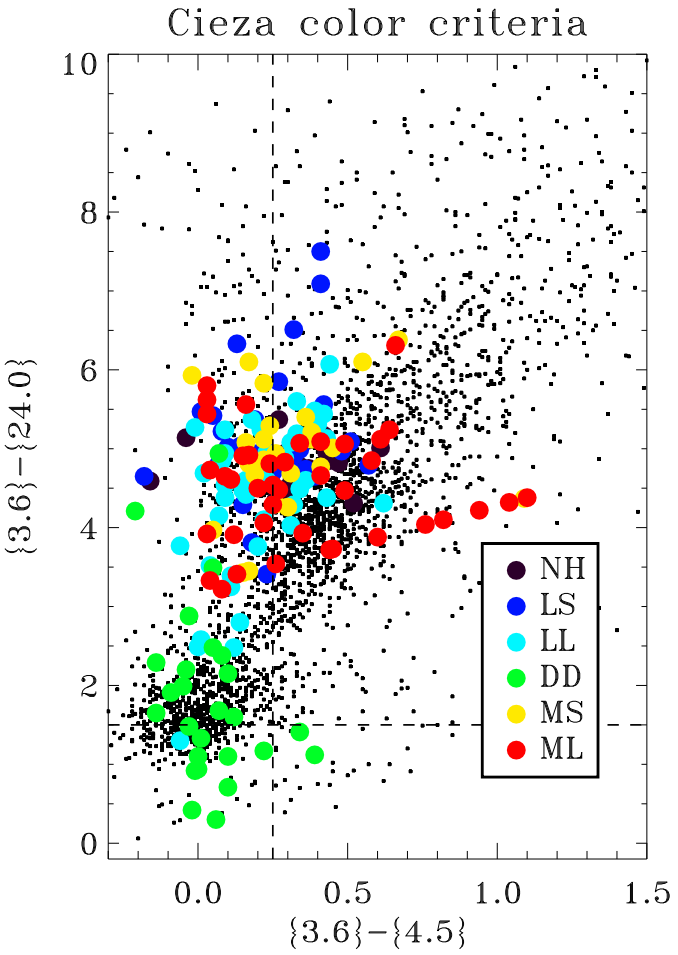

Fig. 8: Evaluation of the initial color criteria by the Cieza survey vs the outcome of our SED modeling. The filled symbols are the targets analyzed in our study, the dots are all YSOs in the c2d, GB and Taurus catalogs. The dashed lines mark the regions: the upper left quartile are the transition disks according to Cieza, the lower left quartile are diskless stars.

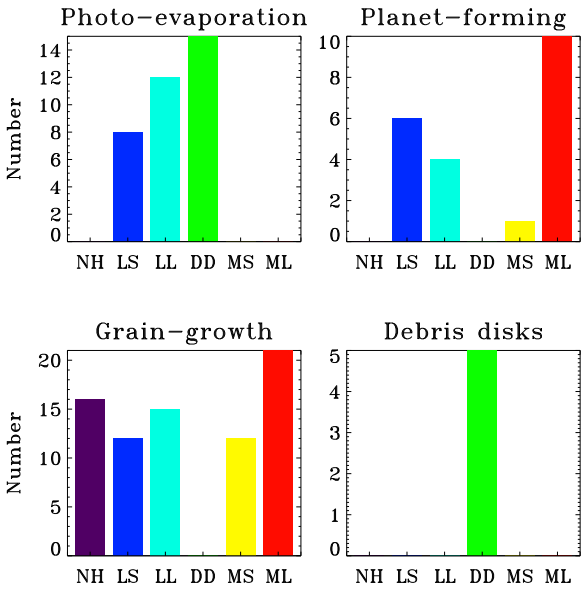

Fig. 9: Comparison of the categorization by the Cieza et al. studies with the classification of this study for our targets.

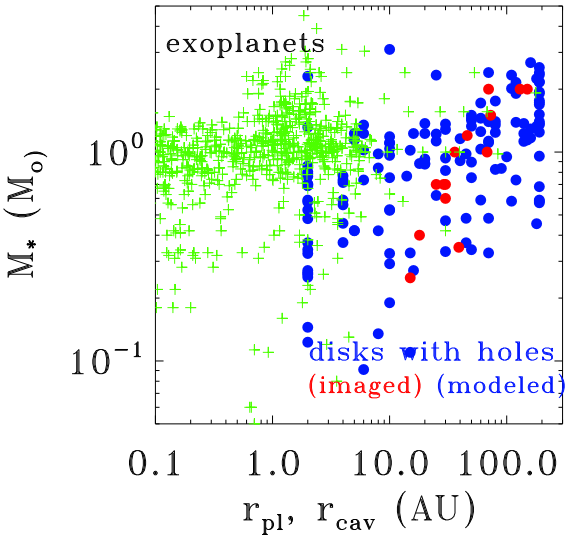

Fig. 11: Comparison of exoplanet orbital radii with transition disk cavity radii. Only cavity radii >2 AU are considered. Exoplanet orbital radii are indicated as green crosses, disk cavities with circles in blue (SED-modeling of this study) and red (millimeter imaging).

cavity radii >2 AU are considered. Both samples are heavily biased, especially there is a lack of planets on orbits larger than 5 AU (radial velocity limit), whereas disk cavity radii can not be detected below 2 AU. The exoplanet data is only fairly complete for r <1 AU (from Kepler) whereas there is no information about transition disk cavity radii at this limit. Therefore, we cannot test any connection with the current data but as both disk and exoplanet will start to fill the critical 2-10 AU range in the coming years it will be important to search for such a relation. A trend is seen between cavity radius and stellar mass (blue and red points in Figure 11) as seen in previous work (Kim et al. 2009; Merín et al. 2010).

5.8. Transition disks within the full YSO sample

A total number of 133 transition disk candidates (ML, MS, LL or LS category) is confirmed through the SED modeling. 108 of these are from one of the main *Spitzer* catalogs (c2d, GB or Taurus) of YSOs in nearby star forming regions. These three catalogs add up to 3331 YSOs, out of which 1387 are classified as disks (Class II objects). This means that approximately 8% of the disks in star forming regions are expected to be transition disks, considering only the targets from the *Spitzer* catalogs. Assuming a Class II lifetime of 3 Myr (Dunham et al. 2015; Ribas et al. 2015), this implies a transition disk lifetime of 0.24 Myr, assuming that disk evolution is continuous over the timespan of the Class II lifetime. More specifically, assuming that transition disks evolve by dissipating mass, the first stage of massive disks (MS+ML, 45 targets) is about 90 kyr, followed by

a longer period of low-mass disks (LS+LL, 63 targets) of 150 kyr. Although it is tempting to conclude that disk dissipation is rapid (Williams & Cieza 2011; Owen 2015), it should be noted that about half of the low-mass disks in the sample is still accreting (see Figure 4) and disk mass alone cannot be used as a robust measurement of transition disk evolution.

6. Summary

The main results of this work are summarized as follows.

1. A large sample of ∼200 transition disk candidates is presented and analyzed. Candidates are primarily selected from the *Spitzer* catalogs using the color criteria from Merín et al. (2010), with some additional targets from the literature.
2. The *Spitzer* data of the targets have been complemented with new submillimeter fluxes, *Herschel*-PACS archival data and optical/near infrared spectroscopy for spectral typing and accretion properties.
3. All targets are analyzed using RADMC-3D modeling with a limited number of parameters: disk mass, inner disk mass, scale height and flaring, and disk cavity radius, where the latter is the main parameter of interest.
4. The derived cavity sizes are consistent with imaging/modeling results in the literature where available.
5. Using the derived properties, the disks are categorized in disks without holes, large/small holes and massive/low-mass disks and very low scale height disks. The latter are likely debris disks. A large fraction of the targets falls in the category of disks with large holes, including several previously imaged disks.
6. Based on this classification, 133 targets (72% of the sample) are disks with cavities, including about 70 new transition disk candidates that had not been identified before.
7. The color criteria are evaluated and compared for the targets in the Cieza studies (Cieza et al. 2010, 2012b; Romero et al. 2012). In general, our color criteria are a proper tool to select transition disk candidates.
8. The cavity radius increases with stellar mass.
9. The sample list provides a large number of transition disk candidates that are suitable for follow-up observations with ALMA.

Acknowledgements. The authors would like to thank C. Manara for useful discussions and M. McClure for providing the IRS spectrum on DoAr28. N.M. is supported by the Netherlands Research School for Astronomy (NOVA). Astrochemistry in Leiden is supported by the Netherlands Research School for Astronomy (NOVA), by a Royal Netherlands Academy of Arts and Sciences (KNAW) professor prize, and by the European Union A-ERC grant 291141 CHEMPLAN. This publication makes use of data products from the Wide-field Infrared Survey Explorer, which is a joint project of the University of California, Los Angeles, and the Jet Propulsion Laboratory/California Institute of Technology, funded by the National Aeronautics and Space Administration.

References

Alcala, J. M., Krautter, J., Schmitt, J. H. M. M., et al. 1995, A&AS, 114, 109
Alcalá, J. M., Natta, A., Manara, C. F., et al. 2014, A&A, 561, A2
Alcalá, J. M., Spezzi, L., Chapman, N., et al. 2008, ApJ, 676, 427
Alexander, R. D., Clarke, C. J., & Pringle, J. E. 2006, MNRAS, 369, 216
Andrews, S. M., Rosenfeld, K. A., Kraus, A. L., & Wilner, D. J. 2013, ApJ, 771, 129
Andrews, S. M. & Williams, J. P. 2005, ApJ, 631, 1134
Andrews, S. M. & Williams, J. P. 2007a, ApJ, 671, 1800
Andrews, S. M. & Williams, J. P. 2007b, ApJ, 659, 705
Andrews, S. M., Wilner, D. J., Espaillat, C., et al. 2011, ApJ, 732, 42
Andrews, S. M., Wilner, D. J., Hughes, A. M., Qi, C., & Dullemond, C. P. 2009, ApJ, 700, 1502
Andrews, S. M., Wilner, D. J., Hughes, A. M., Qi, C., & Dullemond, C. P. 2010, ApJ, 723, 1241
Andrews, S. M., Wilner, D. J., Hughes, A. M., et al. 2012, ApJ, 744, 162
Artymowicz, P. & Lubow, S. H. 1994, ApJ, 421, 651
Artymowicz, P. & Lubow, S. H. 1996, ApJ, 467, L77
Baraffe, I., Chabrier, G., Allard, F., & Hauschildt, P. H. 1998, A&A, 337, 403
Biller, B., Allers, K., Liu, M., Close, L. M., & Dupuy, T. 2011, ApJ, 730, 39
Biller, B., Lacour, S., Juhász, A., et al. 2012, ApJ, 753, L38
Birnstiel, T., Dullemond, C. P., & Brauer, F. 2010, A&A, 513, A79
Bouwman, J., Lawson, W. A., Juhász, A., et al. 2010, ApJ, 723, L243
Broekhoven-Fiene, H., Matthews, B. C., Harvey, P. M., et al. 2014, ApJ, 786, 37
Brown, J. M., Blake, G. A., Dullemond, C. P., et al. 2007, ApJ, 664, L107
Brown, J. M., Blake, G. A., Qi, C., Dullemond, C. P., & Wilner, D. J. 2008, ApJ, 675, L109
Brown, J. M., Blake, G. A., Qi, C., et al. 2009, ApJ, 704, 496
Brown, J. M., Herczeg, G. J., Pontoppidan, K. M., & van Dishoeck, E. F. 2012, ApJ, 744, 116
Bruderer, S., van der Marel, N., van Dishoeck, E. F., & van Kempen, T. A. 2014, A&A, 562, A26
Bustamante, I., Merín, B., Ribas, Á., et al. 2015, A&A, 578, A23
Calvet, N., D'Alessio, P., Hartmann, L., et al. 2002, ApJ, 568, 1008
Calvet, N., Muzerolle, J., Briceño, C., et al. 2004, AJ, 128, 1294
Canovas, H., Schreiber, M. R., Cáceres, C., et al. 2015, ApJ, 805, 21
Carpenter, J. M., Bouwman, J., Silverstone, M. D., et al. 2008, ApJS, 179, 423
Casassus, S., van der Plas, G., M, S. P., et al. 2013, Nature, 493, 191
Castelli, F. & Kurucz, R. L. 2004, ArXiv Astrophysics e-prints
Chiang, E. I. & Goldreich, P. 1997, ApJ, 490, 368
Cieza, L., Padgett, D. L., Stapelfeldt, K. R., et al. 2007, ApJ, 667, 308
Cieza, L. A., Mathews, G. S., Williams, J. P., et al. 2012a, ApJ, 752, 75
Cieza, L. A., Schreiber, M. R., Romero, G. A., et al. 2010, ApJ, 712, 925
Cieza, L. A., Schreiber, M. R., Romero, G. A., et al. 2012b, ApJ, 750, 157
Cieza, L. A., Swift, J. J., Mathews, G. S., & Williams, J. P. 2008, ApJ, 686, L115
Cody, A. M., Stauffer, J., Baglin, A., et al. 2014, AJ, 147, 82
Comerón, F. 2008, The Lupus Clouds, ed. B. Reipurth, 295
Comerón, F. 2012, A&A, 537, A97
Comerón, F., Reipurth, B., Henry, A., & Fernández, M. 2004, A&A, 417, 583
Comerón, F., Spezzi, L., & López Martí, B. 2009, A&A, 500, 1045
Cortes, S. R., Meyer, M. R., Carpenter, J. M., et al. 2009, ApJ, 697, 1305
Currie, T. & Kenyon, S. J. 2009, AJ, 138, 703
Currie, T. & Sicilia-Aguilar, A. 2011, ApJ, 732, 24
Cutri, R. M., Skrutskie, M. F., van Dyk, S., et al. 2003, VizieR Online Data Catalog, 2246, 0
D'Alessio, P., Hartmann, L., Calvet, N., et al. 2005, ApJ, 621, 461
Dullemond, C. P. & Dominik, C. 2004, A&A, 417, 159
Dullemond, C. P. & Dominik, C. 2005, A&A, 434, 971
Dullemond, C. P., Dominik, C., & Natta, A. 2001, ApJ, 560, 957
Dunham, M. M., Allen, L. E., Evans, II, N. J., et al. 2015, ApJS, 220, 11
Dzib, S., Loinard, L., Mioduszewski, A. J., et al. 2010, ApJ, 718, 610
Dzib, S., Loinard, L., Rodríguez, L. F., Mioduszewski, A. J., & Torres, R. M. 2011, ApJ, 733, 71
Enoch, M. L., Young, K. E., Glenn, J., et al. 2006, ApJ, 638, 293
Erickson, K. L., Wilking, B. A., Meyer, M. R., et al. 2015, AJ, 149, 103
Espaillat, C., Calvet, N., D'Alessio, P., et al. 2007, ApJ, 670, L135
Espaillat, C., Furlan, E., D'Alessio, P., et al. 2011, ApJ, 728, 49
Espaillat, C., Muzerolle, J., Najita, J., et al. 2014, Protostars and Planets VI, 497
Evans, II, N. J., Dunham, M. M., Jørgensen, J. K., et al. 2009, ApJS, 181, 321
Flaherty, K. M. & Muzerolle, J. 2010, ApJ, 719, 1733
Fukagawa, M., Tsukagoshi, T., Momose, M., et al. 2013, PASJ, 65, L14
Furlan, E., Hartmann, L., Calvet, N., et al. 2006, ApJS, 165, 568
Furlan, E., Luhman, K. L., Espaillat, C., et al. 2011, ApJS, 195, 3
Garcia Lopez, R., Natta, A., Testi, L., & Habart, E. 2006, A&A, 459, 837
Ghez, A. M., McCarthy, D. W., Patience, J. L., & Beck, T. L. 1997, ApJ, 481, 378
Gräfe, C. & Wolf, S. 2013, A&A, 552, A88
Guenther, E. W., Esposito, M., Mundt, R., et al. 2007, A&A, 467, 1147
Hamuy, M., Walker, A. R., Suntzeff, N. B., et al. 1992, PASP, 104, 533
Hardy, A., Caceres, C., Schreiber, M. R., et al. 2015, A&A, 583, A66
Harvey, P., Merín, B., Huard, T. L., et al. 2007, ApJ, 663, 1149
Harvey, P. M., Huard, T. L., Jørgensen, J. K., et al. 2008, ApJ, 680, 495
Hatchell, J., Terebey, S., Huard, T., et al. 2012, ApJ, 754, 104
Henning, T., Pfau, W., Zinnecker, H., & Prusti, T. 1993, A&A, 276, 129
Herczeg, G. J. & Hillenbrand, L. A. 2014, ApJ, 786, 97
Hernández, J., Hartmann, L., Megeath, T., et al. 2007, ApJ, 662, 1067
Hernández, J., Morales-Calderon, M., Calvet, N., et al. 2010, ApJ, 722, 1226
Holland, W. S., Bintley, D., Chapin, E. L., et al. 2013, MNRAS, 430, 2513
Huélamo, N., de Gregorio-Monsalvo, I., Macias, E., et al. 2015, A&A, 575, L5
Huélamo, N., Lacour, S., Tuthill, P., et al. 2011, A&A, 528, L7
Hughes, A. M., Andrews, S. M., Espaillat, C., et al. 2009, ApJ, 698, 131
Hughes, A. M., Andrews, S. M., Wilner, D. J., et al. 2010, AJ, 140, 887
Hughes, A. M., Wilner, D. J., Qi, C., & Hogerheijde, M. R. 2008, ApJ, 678, 1119
Indebetouw, R., Mathis, J. S., Babler, B. L., et al. 2005, ApJ, 619, 931

Ireland, M. J. & Kraus, A. L. 2008, ApJ, 678, L59
Isella, A., Carpenter, J. M., & Sargent, A. I. 2009, ApJ, 701, 260
Isella, A., Carpenter, J. M., & Sargent, A. I. 2010a, ApJ, 714, 1746
Isella, A., Natta, A., Wilner, D., Carpenter, J. M., & Testi, L. 2010b, ApJ, 725, 1735
Jensen, E. L. N., Mathieu, R. D., & Fuller, G. A. 1996, ApJ, 458, 312
Jørgensen, J. K., Harvey, P. M., Evans, II, N. J., et al. 2006, ApJ, 645, 1246
Kenyon, S. J., Gómez, M., & Whitney, B. A. 2008, Low Mass Star Formation in the Taurus-Auriga Clouds, ed. B. Reipurth, 405
Kenyon, S. J. & Hartmann, L. 1995, ApJS, 101, 117
Kim, K. H., Watson, D. M., Manoj, P., et al. 2009, ApJ, 700, 1017
Kirk, J. M., Ward-Thompson, D., Di Francesco, J., et al. 2009, ApJS, 185, 198
Kohler, R. & Leinert, C. 1998, A&A, 331, 977
Kovács, A. 2008, in Society of Photo-Optical Instrumentation Engineers (SPIE) Conference Series, Vol. 7020, 1
Kraus, A. L. & Hillenbrand, L. A. 2009, ApJ, 703, 1511
Kraus, A. L. & Ireland, M. J. 2012, ApJ, 745, 5
Kraus, A. L., Ireland, M. J., Martinache, F., & Lloyd, J. P. 2008, ApJ, 679, 762
Lafrenière, D., Jayawardhana, R., Brandeker, A., Ahmic, M., & van Kerkwijk, M. H. 2008, ApJ, 683, 844
Lawson, W. A., Lyo, A.-R., & Muzerolle, J. 2004, MNRAS, 351, L39
Lebouteiller, V., Barry, D. J., Spoon, H. W. W., et al. 2011, ApJS, 196, 8
Leinert, C., Henry, T., Glindemann, A., & McCarthy, Jr., D. W. 1997, A&A, 325, 159
Lin, D. N. C. & Papaloizou, J. 1979, MNRAS, 188, 191
Loinard, L., Torres, R. M., Mioduszewski, A. J., & Rodríguez, L. F. 2008, ApJ, 675, L29
Lommen, D., Wright, C. M., Maddison, S. T., et al. 2007, A&A, 462, 211
Lommen, D. J. P., van Dishoeck, E. F., Wright, C. M., et al. 2010, A&A, 515, A77
Luhman, K. L. 2004, ApJ, 602, 816
Luhman, K. L. 2007, ApJS, 173, 104
Luhman, K. L., Allen, L. E., Allen, P. R., et al. 2008, ApJ, 675, 1375
Luhman, K. L., Allen, P. R., Espaillat, C., Hartmann, L., & Calvet, N. 2010, ApJS, 186, 111
Luhman, K. L. & Muench, A. A. 2008, ApJ, 684, 654
Mamajek, E. E., Lawson, W. A., & Feigelson, E. D. 1999, ApJ, 516, L77
Manara, C., Fedele, D., & Herczeg, G. 2015, subm. to A&A
Manara, C. F., Testi, L., Natta, A., et al. 2014, A&A, 568, A18
Mathews, G. S., Williams, J. P., & Ménard, F. 2012, ApJ, 753, 59
McClure, M. K., Furlan, E., Manoj, P., et al. 2010, ApJS, 188, 75
Megeath, S. T., Gutermuth, R., Muzerolle, J., et al. 2012, AJ, 144, 192
Megeath, S. T., Hartmann, L., Luhman, K. L., & Fazio, G. G. 2005, ApJ, 634, L113
Mendigutía, I., Mora, A., Montesinos, B., et al. 2012, A&A, 543, A59
Merín, B., Brown, J. M., Oliveira, I., et al. 2010, ApJ, 718, 1200
Merín, B., Jørgensen, J., Spezzi, L., et al. 2008, ApJS, 177, 551
Monnier, J. D., Tannirkulam, A., Tuthill, P. G., et al. 2008, ApJ, 681, L97
Mooley, K., Hillenbrand, L., Rebull, L., Padgett, D., & Knapp, G. 2013, ApJ, 771, 110
Muzerolle, J., Allen, L. E., Megeath, S. T., Hernández, J., & Gutermuth, R. A. 2010, ApJ, 708, 1107
Najita, J. R., Carr, J. S., Strom, S. E., et al. 2010, ApJ, 712, 274
Najita, J. R., Strom, S. E., & Muzerolle, J. 2007, MNRAS, 378, 369
Natta, A., Testi, L., Muzerolle, J., et al. 2004, A&A, 424, 603
Natta, A., Testi, L., & Randich, S. 2006, A&A, 452, 245
Nguyen, D. C., Brandeker, A., van Kerkwijk, M. H., & Jayawardhana, R. 2012, ApJ, 745, 119
Nuernberger, D., Chini, R., & Zinnecker, H. 1997, A&A, 324, 1036
Ohashi, N. 2008, Ap&SS, 313, 101
Oke, J. B. 1990, AJ, 99, 1621
Oliveira, I., Merín, B., Pontoppidan, K. M., & van Dishoeck, E. F. 2013, ApJ, 762, 128
Oliveira, I., Merín, B., Pontoppidan, K. M., et al. 2009, ApJ, 691, 672
Oliveira, I., Pontoppidan, K. M., Merín, B., et al. 2010, ApJ, 714, 778
Olofsson, J., Szűcs, L., Henning, T., et al. 2013, A&A, 560, A100
Ortiz-León, G. N., Loinard, L., Mioduszewski, A. J., et al. 2015, ApJ, 805, 9
Owen, J. E. 2015, ArXiv e-prints
Owen, J. E. & Clarke, C. J. 2012, MNRAS, 426, L96
Padgett, D. L., Cieza, L., Stapelfeldt, K. R., et al. 2006, ApJ, 645, 1283
Padgett, D. L., Rebull, L. M., Stapelfeldt, K. R., et al. 2008, ApJ, 672, 1013
Pérez, L. M., Isella, A., Carpenter, J. M., & Chandler, C. J. 2014, ApJ, 783, L13
Perez, S., Casassus, S., Ménard, F., et al. 2015, ApJ, 798, 85
Peterson, D. E., Caratti o Garatti, A., Bourke, T. L., et al. 2011, ApJS, 194, 43
Pickles, A. J. 1998, PASP, 110, 863
Piétu, V., Dutrey, A., Guilloteau, S., Chapillon, E., & Pety, J. 2006, A&A, 460, L43
Piétu, V., Guilloteau, S., & Dutrey, A. 2005, A&A, 443, 945
Pilbratt, G. L., Riedinger, J. R., Passvogel, T., et al. 2010, A&A, 518, L1
Pinilla, P., Benisty, M., & Birnstiel, T. 2012, A&A, 545, A81
Poglitsch, A., Waelkens, C., Geis, N., et al. 2010, A&A, 518, L2
Pott, J.-U., Perrin, M. D., Furlan, E., et al. 2010, ApJ, 710, 265
Quanz, S. P. 2015, Ap&SS, 357, 148
Quanz, S. P., Amara, A., Meyer, M. R., et al. 2013, ApJ, 766, L1
Ratzka, T., Köhler, R., & Leinert, C. 2005, A&A, 437, 611
Rebollido, I., Merín, B., Ribas, Á., et al. 2015, A&A, 581, A30
Rebull, L. M., Padgett, D. L., McCabe, C.-E., et al. 2010, ApJS, 186, 259
Reggiani, M., Quanz, S. P., Meyer, M. R., et al. 2014, ApJ, 792, L23
Revéret, V., André, P., Le Pennec, J., et al. 2014, in Society of Photo-Optical Instrumentation Engineers (SPIE) Conference Series, Vol. 9153, 5
Ribas, Á., Bouy, H., & Merín, B. 2015, A&A, 576, A52
Ribas, Á., Merín, B., Bouy, H., et al. 2013, A&A, 552, A115
Rigliaco, E., Pascucci, I., Duchene, G., et al. 2015, ApJ, 801, 31
Romero, G. A., Schreiber, M. R., Cieza, L. A., et al. 2012, ApJ, 749, 79
Rosenfeld, K. A., Andrews, S. M., Wilner, D. J., Kastner, J. H., & McClure, M. K. 2013, ApJ, 775, 136
Rosotti, G. P., Ercolano, B., Owen, J. E., & Armitage, P. J. 2013, MNRAS, 430, 1392
Sallum, S., Follette, K. B., Eisner, J. A., et al. 2015, Nature, 527, 342
Salyk, C., Herczeg, G. J., Brown, J. M., et al. 2013, ApJ, 769, 21
Schisano, E., Covino, E., Alcalá, J. M., et al. 2009, A&A, 501, 1013
Schuller, F. 2012, in Society of Photo-Optical Instrumentation Engineers (SPIE) Conference Series, Vol. 8452, 1
Sicilia-Aguilar, A., Bouwman, J., Juhász, A., et al. 2009, ApJ, 701, 1188
Sicilia-Aguilar, A., Henning, T., Juhász, A., et al. 2008, ApJ, 687, 1145
Siess, L., Dufour, E., & Forestini, M. 2000, A&A, 358, 593
Silverstone, M. D., Meyer, M. R., Mamajek, E. E., et al. 2006, ApJ, 639, 1138
Siringo, G., Kreysa, E., De Breuck, C., et al. 2010, The Messenger, 139, 20
Siringo, G., Kreysa, E., Kovács, A., et al. 2009, A&A, 497, 945
Spezzi, L., Alcalá, J. M., Covino, E., et al. 2008, ApJ, 680, 1295
Spezzi, L., Vernazza, P., Merín, B., et al. 2011, ApJ, 730, 65
Stauffer, J., Cody, A. M., Baglin, A., et al. 2014, AJ, 147, 83
Strom, K. M., Strom, S. E., Edwards, S., Cabrit, S., & Skrutskie, M. F. 1989, AJ, 97, 1451
Tang, Y.-W., Guilloteau, S., Piétu, V., et al. 2012, A&A, 547, A84
Torres, C. A. O., Quast, G. R., Melo, C. H. F., & Sterzik, M. F. 2008, Young Nearby Loose Associations, ed. B. Reipurth, 757
van der Marel, N., van Dishoeck, E. F., Bruderer, S., et al. 2016, A&A, 585, A58
van der Marel, N., van Dishoeck, E. F., Bruderer, S., et al. 2013, Science, 340, 1199
van der Marel, N., van Dishoeck, E. F., Bruderer, S., Pérez, L., & Isella, A. 2015, A&A, 579, A106
van Kempen, T. A., van Dishoeck, E. F., Salter, D. M., et al. 2009, A&A, 498, 167
Venuti, L., Bouvier, J., Flaccomio, E., et al. 2014, A&A, 570, A82
Verhoeff, A. P., Min, M., Pantin, E., et al. 2011, A&A, 528, A91
Vicente, S., Merín, B., Hartung, M., et al. 2011, A&A, 533, A135
Wahhaj, Z., Cieza, L., Koerner, D. W., et al. 2010, ApJ, 724, 835
White, R. J. & Basri, G. 2003, ApJ, 582, 1109
White, R. J. & Ghez, A. M. 2001, ApJ, 556, 265
Wilking, B. A., Meyer, M. R., Robinson, J. G., & Greene, T. P. 2005, AJ, 130, 1733
Williams, J. P. & Cieza, L. A. 2011, ARA&A, 49, 67
Winston, E., Megeath, S. T., Wolk, S. J., et al. 2009, AJ, 137, 4777
Wright, E. L., Eisenhardt, P. R. M., Mainzer, A. K., et al. 2010, AJ, 140, 1868
Young, K. E., Young, C. H., Lai, S.-P., Dunham, M. M., & Evans, II, N. J. 2015, AJ, 150, 40
Zacharias, N., Monet, D. G., Levine, S. E., et al. 2005, VizieR Online Data Catalog, 1297, 0
Zhang, K., Isella, A., Carpenter, J. M., & Blake, G. A. 2014, ApJ, 791, 42

Appendix A: Tables

Table A.1: Sample of transition disk candidates

ID	Target	RA	Dec	Reg[a]	d[b] (pc)	Color[c]	Origin data	Prev.[d]	Ref
1	TCha	11 57 13.53	-79 21 31.5	ϵ Cha	108	[L]	Other	Imag.	1,2
2	RECX11	08 47 01.80	-78 59 35.2	η Cha	97	-	Other	TD	3,4
3	RECX5	08 42 27.09	-78 57 47.9	η Cha	97	[A]	Other	PF	5,4
4	CHXR22E	11 07 13.30	-77 43 49.9	ChaI	160	-	Other	TD	6,7
5	ISO52	11 04 42.58	-77 41 57.1	ChaI	160	[B]	GB	V	8
6	CSCha	11 02 25.11	-77 33 35.9	ChaI	160	[L]	c2d	V	8
7	11094742-7726290	11 09 47.27	-77 26 29.5	ChaI	160	[B]	GB		
9	T54	11 12 42.69	-77 22 23.1	ChaI	160	[L]	GB	CB	9
10	T21	11 06 15.41	-77 21 56.9	ChaI	160	-	Other	TD	6,7
11	SZCha	10 58 16.77	-77 17 17.1	ChaI	160	-	-	TD	9
12	T35	11 08 39.05	-77 16 04.2	ChaI	160	[A]	GB	TD/V	6,10
13	ISO-ChaII29	12 59 10.19	-77 12 13.7	ChaII	180	[L]	c2d		
14	T56	11 17 37.01	-77 04 38.1	ChaI	160	-	-	TD/V	6,10
15	CRCha	10 59 06.97	-77 01 40.3	ChaI	160	-	-	V	8
16	WWCha	11 10 00.11	-76 34 57.9	ChaI	160	[B]	-	V	8
17	11062554-7633418	11 06 25.47	-76 33 42.2	ChaI	160	[B]	GB		
18	T25	11 07 19.15	-76 03 04.9	ChaI	160	[A][L]	Other	V	11,7
20	MPMus	13 22 07.55	-69 38 12.2	Isol.	100	[B]	Other	TD	12,13
21	HD142527	15 56 41.89	-42 19 23.3	Isol.	140	-	-	Imag.	14
22	J16232807-4015368	16 23 28.09	-40 15 36.9	LupVI	150	[A][L]	GB		
23	Sz111	16 08 54.69	-39 37 43.1	LupIII	200	[A][L]	c2d	LU	15
24	Lup60	16 10 29.56	-39 22 14.7	LupIII	200	[A]	c2d	GG	16
25	J160830.3-390611	16 08 30.26	-39 06 11.1	LupIII	200	[B]	c2d	L	15
26	Sz104	16 08 30.80	-39 05 48.8	LupIII	200	[B]	c2d	H	15
27	Sz91	16 07 11.60	-39 03 47.7	LupIII	200	[L]	c2d	PF	16
28	J160855.5-390234	16 08 55.52	-39 02 33.9	LupIII	200	[A]	c2d	L/PE	17,18
29	Sz84	15 58 02.50	-37 36 02.8	LupI	150	[L] *	c2d	TD	19
30	16182186-3730298	16 18 21.88	-37 30 29.9	LupV	150	[L]	GB		
31	16225309-3724373	16 22 53.10	-37 24 37.4	LupV	150	[L]	GB		
32	J19002346-3712242	19 00 23.47	-37 12 24.2	CrA	150	[A]	GB		
33	HD135344	15 15 48.44	-37 09 16.0	Isol.	140	[B]	-	Imag.	20
34	CrA-466	19 01 18.95	-36 58 28.3	CrA	150	-	Other	TD	21
35	Sz76	15 49 30.80	-35 49 52.0	LupI	150	[B]	Other		22
36	J154508.9-341734	15 45 08.88	-34 17 33.7	LupI	150	-	Other	LU	15
38	RXJ1615.3-3255	16 15 20.23	-32 55 04.9	Lup	185	[B] *	c2d	Imag.	23
39	V4046Sgr	18 14 10.47	-32 47 34.5	Isol.	73	-	-	Imag.	24
40	J163154.7-250324	16 31 54.73	-25 03 24.0	Oph	125	[B]	c2d	GG	25
41	J163205.5-250236	16 32 05.52	-25 02 36.2	Oph	125	[A]	c2d	PF	25
43	J163023.4-245416	16 30 23.39	-24 54 16.1	Oph	125	[B]	c2d		
44	WSB63	16 28 54.06	-24 47 44.3	Oph	125	[A]	c2d	PF	25
45	SR24S	16 26 58.51	-24 45 37.0	Oph	125	-	c2d	Imag.	26
46	RXJ1633.9-2442	16 33 55.60	-24 42 05.0	Oph	125	[A]	c2d	Imag.	25,50
47	ISO-Oph43	16 26 27.53	-24 41 53.6	Oph	125	[B]	c2d		
48	WSB60	16 28 16.51	-24 36 58.3	Oph	125	[B]	c2d	Imag.	23
49	J163115.7-243402	16 31 15.74	-24 34 02.0	Oph	125	[B]	c2d	GG	25
50	J162245.4-243124	16 22 45.39	-24 31 23.8	Oph	125	[A] *	c2d	PE	25
51	IRS48	16 27 37.19	-24 30 34.8	Oph	125	-	Other	Imag.	27,28
52	DoAr44	16 31 33.46	-24 27 37.4	Oph	125	[B]	c2d	Imag.	29
53	J162435.2-242620	16 24 35.20	-24 26 20.0	Oph	125	[A]	c2d		
54	SR21	16 27 10.28	-24 19 12.5	Oph	125	-	-	Imag.	20
55	J162309.2-241705	16 23 09.22	-24 17 04.6	Oph	125	[A]	c2d	PTD	30
56	J163136.8-240420	16 31 36.77	-24 04 19.8	Oph	125	[L]	c2d		
58	J162648.6-235634	16 26 48.64	-23 56 34.1	Oph	125	[B]	c2d		
59	J162802.6-235504	16 28 02.60	-23 55 04.0	Oph	125	[A]	c2d	PE	25
60	oph62	16 25 06.92	-23 50 50.4	Oph	125	[A] *	c2d	PF	25
61	J162532.5-232626	16 25 32.50	-23 26 26.0	Oph	125	[A]	c2d		
62	J162218.5-232148	16 22 18.52	-23 21 48.1	Oph	125	[B]	c2d	GG	25
63	DoAr28	16 26 47.42	-23 14 52.2	Oph	125	-	HREL	TD	30
64	J160421.7-213028	16 04 21.70	-21 30 28.4	UppS	145	[L]	-	Imag.	31

Table A.1: Sample continued.

ID	Target	RA	Dec	Reg[a]	d[b] (pc)	Color[c]	Origin data	Prev.[d]	Ref
65	18015423-0437531	18 01 54.24	-04 37 53.1	Ser	415	[L]	GB		
66	18044921-0436413	18 04 49.20	-04 36 41.5	Ser	415	[B]	GB		
67	18270980-0414297	18 27 09.79	-04 14 29.8	Ser	415	[L]	GB		
68	18272873-0406248	18 27 28.73	-04 06 24.8	Ser	415	[L]	GB		
69	18273408-0403247	18 27 34.08	-04 03 24.8	Ser	415	[L]	GB		
70	18273858-0402289	18 27 38.57	-04 02 28.9	Ser	415	[A][L]	GB		
71	18255765-0357040	18 25 57.66	-03 57 04.0	Ser	415	[L]	GB		
73	18291383-0342355	18 29 13.84	-03 42 35.5	Ser	415	[L]	GB		
74	18284156-0341507	18 28 41.56	-03 41 50.7	Ser	415	[L]	GB		
75	18283439-0339371	18 28 34.40	-03 39 37.2	Ser	415	[L]	GB		
76	18272161-0314158	18 27 21.62	-03 14 15.9	Ser	415	[L]	GB		
77	18222604-0304383	18 22 26.04	-03 04 38.3	Ser	415	[L]	GB		
78	18330328-0244021	18 33 03.30	-02 44 02.2	Ser	415	[B]	GB		
79	18324685-0243273	18 32 46.86	-02 43 27.4	Ser	415	[L]	GB		
80	18304127-0242335	18 30 41.26	-02 42 33.7	Ser	415	[L]	GB		
81	18324783-0239401	18 32 47.83	-02 39 40.1	Ser	415	[B]	GB		
82	J18321275-0222377	18 32 12.75	-02 22 37.8	Ser	415	[A][L]	GB		
83	18292883-0221157	18 29 28.84	-02 21 15.7	Ser	415	[A][L]	GB		
84	18291450-0220575	18 29 14.50	-02 20 57.5	Ser	415	[L]	GB		
85	18304121-0220189	18 30 41.20	-02 20 19.1	Ser	415	[B]	GB		
86	J18314556-0218408	18 31 45.57	-02 18 40.9	Ser	415	[A]	GB		
88	18311986-0208161	18 31 19.86	-02 08 16.1	Ser	415	[A]	GB		
89	18323005-0204130	18 32 30.06	-02 04 13.0	Ser	415	[A][L]	GB		
90	18292804-0204042	18 29 28.07	-02 04 04.7	Ser	415	[A]	GB		
91	18293961-0202414	18 29 39.60	-02 02 41.4	Ser	415	[B]	GB		
92	J18303289-0200514	18 30 32.89	-02 00 51.3	Ser	415	[A][L]	GB		
93	18311732-0200461	18 31 17.32	-02 00 46.1	Ser	415	[A]	GB		
94	18312875-0159125	18 31 28.75	-01 59 12.5	Ser	415	[A]	GB		
95	18315497-0157330	18 31 54.98	-01 57 33.1	Ser	415	[L]	GB		
96	18313657-0157320	18 31 36.57	-01 57 32.0	Ser	415	[A]	GB		
97	18313343-0155182	18 31 33.43	-01 55 18.2	Ser	415	[A]	GB		
98	18315077-0153393	18 31 50.77	-01 53 39.3	Ser	415	[B]	GB		
99	J18303321-0152563	18 30 33.22	-01 52 56.2	Ser	415	[A][L]	GB		
100	18295741-0151541	18 29 57.41	-01 51 54.1	Ser	415	[A][L]	GB		
101	18294721-0148301	18 29 47.21	-01 48 30.2	Ser	415	[A][L]	GB		
102	18293368-0145103	18 29 33.69	-01 45 10.3	Ser	415	[B]	GB		
103	18290819-0139215	18 29 08.19	-01 39 21.5	Ser	415	[B]	GB		
104	18314110-0128035	18 31 41.10	-01 28 03.6	Ser	415	[L]	GB		
105	18290391-0115357	18 29 03.92	-01 15 35.8	Ser	415	[L]	GB		
106	18371575-0026561	18 37 15.75	-00 26 56.1	Ser	415	[L]	GB		
107	18381010-0023452	18 38 10.10	-00 23 45.2	Ser	415	[L]	GB		
108	18371444-0023261	18 37 14.45	-00 23 26.2	Ser	415	[L]	GB		
110	18385989-0008097	18 38 59.90	-00 08 09.9	Ser	415	[L]	GB		
111	J182813.5+000-249	18 28 13.51	-00 02 49.1	Ser	415	[B]	c2d	TT	32
112	J182821.6+000016	18 28 21.58	+00 00 16.4	Ser	415	[B]	c2d	L	32
113	18384257+0001324	18 38 42.59	+00 01 32.5	Ser	415	[A][L]	GB		
114	18392594+0006382	18 39 25.96	+00 06 38.4	Ser	415	[A]	GB		
115	J182850.2+000950	18 28 50.21	+00 09 49.7	Ser	415	[B]	c2d	F	32
116	183549.4+001002	18 35 49.38	+00 10 01.7	Ser	415	[L]	GB		
117	18385571+0014431	18 38 55.72	+00 14 43.1	Ser	415	[A][L]	GB		
118	18394048+0014497	18 39 40.50	+00 14 49.7	Ser	415	[B]	GB		
119	18374209+0016519	18 37 42.09	+00 16 52.0	Ser	415	[L]	GB		
120	J182911.5+002039	18 29 11.49	+00 20 38.8	Ser	415	[A] *	c2d		
121	18375663-0023253	18 37 56.63	-00 23 25.3	Ser	415	[A]	GB		
122	18381580+0024218	18 38 15.81	+00 24 21.9	Ser	415	[L]	GB		
123	J18295130+0027477	18 29 51.30	+00 27 47.9	Ser	415	[L]	c2d	LU	32
124	serp22	18 28 29.06	+00 27 56.0	Ser	415	[A] *	c2d		
125	18401205+0029276	18 40 12.06	+00 29 27.7	Ser	415	[B]	GB		
126	J182901.2+002933	18 29 01.22	+00 29 33.0	Ser	415	[B]	c2d	L	32
127	Serp127	18 29 44.10	+00 33 56.0	Ser	415	[A][L] *	c2d	LU	32

Table A.1: Sample continued.

ID	Target	RA	Dec	Reg[a]	d[b] (pc)	Color[c]	Origin data	Prev.[d]	Ref
128	J182935.6+003504	18 29 35.62	+00 35 03.9	Ser	415	[A] *	c2d	LU	32
129	18381447+0035099	18 38 14.48	+00 35 09.8	Ser	415	[L]	GB		
130	18401486+0037042	18 40 14.88	+00 37 04.2	Ser	415	[A][L]	GB		
131	Serp111	18 29 36.19	+00 42 16.7	Ser	415	[A] *	c2d	LU	32
132	J182955.3+004939	18 29 55.32	+00 49 39.3	Ser	415	[A]	c2d	TT	32
133	J183008.6+005847	18 30 08.62	+00 58 46.7	Ser	415	[B]	c2d	TT	32
134	RXJ0432.8+1735	04 32 53.24	+17 35 33.7	Tau	140	-	Tau	TD	33
135	DMTau	04 33 48.73	+18 10 10.0	Tau	140	-	Tau	Imag./V	34,10
136	UXTauA	04 30 04.00	+18 13 49.3	Tau	140	[A]	Other	Imag.	34,35
137	043339.0+222720	04 33 39.00	+22 27 20.0	Tau	140	[A]	Tau		33
138	043326.2+224529	04 33 26.20	+22 45 29.0	Tau	140	[L]	Tau		36
139	J04390525+2337450	04 39 05.25	+23 37 45.0	Tau	140	[B]	GB	PTD	33
140	043649.1+241258	04 36 49.10	+24 12 58.0	Tau	140	[L]	Tau	DD	37
142	MWC758	05 30 27.53	+25 19 56.9	Isol.	200	-	Tau	Imag.	38
144	044555.7+261858	04 45 55.70	+26 18 58.0	Tau	140	[L]	Tau		
145	DHTauAB	04 29 41.50	+26 32 58.0	Tau	140	[A]	Tau		
146	043044.7+263308	04 30 44.70	+26 33 08.0	Tau	140	[L]	Tau		
147	J04214631+2659296	04 21 46.32	+26 59 29.6	Tau	140	[A]	Tau		
148	IPTau	04 24 57.08	+27 11 56.5	Tau	140	-	Tau	V	8
149	V892Tau	04 18 40.62	+28 19 15.5	Tau	140	-	Tau	CB-disk	39
150	V410X-ray6	04 19 01.10	+28 19 42.0	Tau	140	[A]	Tau	PF/TD	40,41
151	042254.6+282354	04 22 54.60	+28 23 54.0	Tau	140	[L]	Tau		
152	V819Tau	04 19 26.26	+28 26 14.3	Tau	140	-	Tau	TD	33
153	RYTau	04 21 57.41	+28 26 35.6	Tau	140	-	Tau	Imag./V	42,10
154	V410X-ray2	04 18 34.40	+28 30 30.0	Tau	140	[A]	Tau	TD	33
155	041542.7+290959	04 15 42.78	+29 09 59.0	Tau	140	[A][L]	Tau	TD	33
156	041332.3+291726	04 13 32.30	+29 17 26.0	Tau	140	[A]	Tau		
157	J032800.1+300847	03 28 00.09	+30 08 47.0	Per	250	[B]	c2d		
158	LkCa19	04 55 36.96	+30 17 55.2	Tau	140	-	Other	TD	43,35
159	ABAur	04 55 45.85	+30 33 04.3	Tau	140	-	-	Imag.	44
160	J033341.3+311341	03 33 41.29	+31 13 41.0	Per	250	[B]	c2d		
161	ASR118	03 28 56.97	+31 16 22.3	Per	250	[B] *	c2d		
162	MBO22	03 29 29.27	+31 18 34.7	Per	250	[A] *	c2d	PF	25
163	J032856.6+311836	03 28 56.65	+31 18 35.5	Per	250	[B]	c2d		
164	J034219.3+314327	03 42 19.27	+31 43 27.0	Per	250	[B]	c2d		
165	J034227.1+314433	03 42 27.12	+31 44 32.9	Per	250	[A] *	c2d		
166	J034109.1+314438	03 41 09.13	+31 44 37.9	Per	250	[B]	c2d		
167	J034355.2+315532	03 43 55.20	+31 55 32.0	Per	250	[A]	c2d		
168	J034434.8+315655	03 44 34.81	+31 56 55.2	Per	250	[A] *	c2d		
169	IC348LRL190	03 44 29.23	+32 01 15.7	Per	250	[A] *	c2d		
171	J034520.5+320634	03 45 20.46	+32 06 34.5	Per	250	[B]	c2d		
172	IC348-67	03 43 44.63	+32 08 17.8	Per	250	[A]	c2d	PF	37
173	LkH-alpha330	03 45 48.29	+32 24 11.8	Per	250	[B]	c2d	Imag.	20
174	J04300424+3522238	04 30 04.25	+35 22 23.8	Aur	450	[A][L]	GB	PF	37
175	J04303235+3536133	04 30 32.35	+35 36 13.4	Tau	140	[L]	GB	PF	37
176	04300980+3540355	04 30 09.80	+35 40 35.6	Tau	140	[B]	GB		
177	J04304004+3542101	04 30 40.05	+35 42 10.3	Tau	140	[L]	GB	GG	37
178	J04303831+3549591	04 30 38.27	+35 49 59.3	Aur	450	[L]	GB		
179	J160044.5-415531	16 00 44.53	-41 55 31.2	LupIV	150	[B]	c2d	PF	16
180	J190058.1-364505	19 00 58.05	-36 45 05.0	UppS	145	[A]	GB	PF	16
181	03445614+3209152	03 44 56.14	+32 09 15.1	Per	250	[A]	c2d	PF	37
182	03442156+3215098	03 44 21.58	+32 15 09.7	Per	250	[A]	c2d	PE	37
183	03442257+3201536	03 44 22.58	+32 01 53.8	Per	250	[A]	c2d	PE	37
184	04330422+2921499	04 33 04.22	+29 21 50.0	Per	250	[A]	Tau	DD	37
185	J160825.76-390601.1	16 08 25.76	-39 06 01.1	LupIII	200	[B]	c2d	TT	15
186	RXJ1556.1-3655	15 56 02.10	-36 55 28.2	LupIII	150	[B]	Other		22
187	043150.5+242418	04 31 50.50	+24 24 18.0	Tau	140	[B]	Tau		
188	041413.5+281249	04 14 13.50	+28 12 49.0	Tau	140	[B]	Tau		
189	041841.3+282725	04 18 41.30	+28 27 25.0	Tau	140	[B]	Tau		
190	042025.5+270035	04 20 25.50	+27 00 35.0	Tau	140	[B]	Tau		

Table A.1: Sample continued.

ID	Target	RA	Dec	Reg[a]	d[b] (pc)	Color[c]	Origin data	Prev.[d]	Ref
191	042921.6+270125	04 29 21.60	+27 01 25.0	Tau	140	[B]	Tau		
192	043249.1+225302	04 32 49.10	+22 53 02.0	Tau	140	[B]	Tau		
193	044221.0+252034	04 42 21.00	+25 20 34.0	Tau	140	[B]	Tau		
194	041539.1+281858	04 15 39.10	+28 18 58.0	Tau	140	[B]	Tau		
195	042318.2+264115	04 23 18.20	+26 41 15.0	Tau	140	[B]	Tau		
196	041414.5+282758	04 14 14.50	+28 27 58.0	Tau	140	[B]	Tau		
197	041915.8+290626	04 19 15.80	+29 06 26.0	Tau	140	[B]	Tau		
198	042155.6+275506	04 21 55.60	+27 55 06.0	Tau	140	[B]	Tau		
200	J160710.08-391103.5	16 07 10.08	-39 11 03.5	LupIII	200	[B]	c2d	L	15
201	J032741.47+302016.8	03 27 41.47	+30 20 16.8	Per	250	[B]	c2d		
202	J034345.17+320358.6	03 43 45.17	+32 03 58.6	Per	250	[A]	c2d		
203	J182815.26-000243.3	18 28 15.26	-00 02 43.3	Ser	415	[B]	c2d		
204	J162715.89-243843.2	16 27 15.89	-24 38 43.2	Oph	125	[B]	c2d		30
301	J130455.7-773949	13 04 55.74	-77 39 49.5	ChaII	180	[B] *	c2d		
303	J160115.5-415235	16 01 15.55	-41 52 35.3	LupIV	150	[B]	c2d	F	15
307	16083070-3828268	16 08 30.70	-38 28 26.8	LupIII	200	[B]	HREL	L	15
309	TWHya	11 01 51.91	-34 42 17.0	TWH	50	-	-	TD	45
310	15395742-3414567	15 39 57.42	-34 14 56.7	LupI	150	-	HREL		
314	16281385-2456113	16 28 13.85	-24 56 11.3	Oph	125	[B]	HREL		
316	16271587-2438433	16 27 15.87	-24 38 43.3	Oph	125	[B]	HREL		
317	16312019-2430009	16 31 20.19	-24 30 00.9	Oph	125	[B]	HREL		
318	DoAr21	16 26 03.03	-24 23 36.4	Oph	125	[A] *	c2d		
319	J162740.3-242204	16 27 40.27	-24 22 04.0	Oph	125	[A]	c2d	CB	25
321	Serp48	18 28 58.08	+00 17 24.5	Ser	415	[LL] *	c2d		
322	18302986+0035004	18 30 29.86	+00 35 00.4	Ser	415	[B]	HREL		
325	LkCa15	04 39 17.78	+22 21 03.5	Tau	140	[A]	Tau	Imag./V	46,10
326	CoKu-Tau-4	04 41 16.79	+28 40 00.5	Tau	140	-	-	CB-disk	47
329	GMAur	04 55 10.98	+30 21 59.4	Tau	140	[A]	-	Imag./V	48,10
333	03370363+3039291	03 37 03.63	+30 39 29.1	Per	250	-	HREL		
334	03401579+3055047	03 40 15.79	+30 55 04.7	Per	250	[B]	HREL		
335	J033234.0+310056	03 32 34.00	+31 00 56.0	Per	250	[B] *	c2d		
348	UScoJ155837.1-225724	15 58 36.91	-22 57 15.3	UppS	145	[B]	Other		49
349	RXJ1842.9-3532	18 42 57.95	-35 32 42.7	UppS	145	[A]	Other		49
350	RXJ1852.3-3700	18 52 17.30	-37 00 11.9	UppS	145	[A]	Other		49

Refs. 1) Wahhaj et al. (2010), 2) Huélamo et al. (2015), 3) Megeath et al. (2005), 4) Sicilia-Aguilar et al. (2009), 5) Bouwman et al. (2010), 6) Kim et al. (2009), 7) Luhman et al. (2008), 8) Espaillat et al. (2011), 9) Kim et al. (2009), 10) Espaillat et al. (2011), 11) Espaillat et al. (2011), 12) Cortes et al. (2009), 13) Silverstone et al. (2006), 14) Ohashi (2008), 15) Merín et al. (2008), 16) Romero et al. (2012), 17) Merín et al. (2008), 18) Romero et al. (2012), 19) Merín et al. (2010), 20) Brown et al. (2009), 21) Sicilia-Aguilar et al. (2008), 22) Padgett et al. (2006), 23) Andrews et al. (2011), 24) Rosenfeld et al. (2013), 25) Cieza et al. (2010), 26) Andrews et al. (2010), 27) van der Marel et al. (2013), 28) van Kempen et al. (2009), 29) Andrews et al. (2009), 30) McClure et al. (2010), 31) Mathews et al. (2012), 32) Harvey et al. (2007), 33) Furlan et al. (2011), 34) Andrews et al. (2011), 35) Wahhaj et al. (2010), 36) Rebull et al. (2010), 37) Cieza et al. (2012b), 38) Isella et al. (2010b), 39) Monnier et al. (2008), 40) Cieza et al. (2012b), 41) Furlan et al. (2011), 42) Isella et al. (2010a), 43) Furlan et al. (2011), 44) Piétu et al. (2005), 45) Najita et al. (2010), 46) Piétu et al. (2006), 47) Ireland & Kraus (2008), 48) Hughes et al. (2009), 49) Carpenter et al. (2008), 50) Cieza et al. (2012a)

Notes. [(a)] Full names of the regions: Cha = Chamaeleon, Lup = Lupus, CrA = Corona Australis, Oph = Ophiuchus, UppS = Upper Sco, Oph = Ophiuchus, Tau = Taurus, Aur = Auriga, Per = Perseus, TWH = TW Hydrae, Isol. = Isolated. [(b)] Distances were adopted from the literature as follows: 120 pc for Oph (Loinard et al. 2008); 150 pc for Lup I, IV, V and VI and 200 pc for LupIII (Comerón 2008; Comerón et al. 2009); 250 pc for Per (Jørgensen et al. 2006); 140 pc for Tau (Kenyon et al. 2008); 450 pc for Aur (Broekhoven-Fiene et al. 2014); 145 pc for Upp Sco (Carpenter et al. 2008); 150 pc for Corona Australis (Sicilia-Aguilar et al. 2008); 109 pc for ϵ Cha(Torres et al. 2008); 160 pc for ChaI (Kim et al. 2009); 180 pc for ChaII (Alcalá et al. 2008); 97 pc for η Cha(Mamajek et al. 1999); and 430 pc for Ser (Dzib et al. 2010). [(c)] An asterix (*) indicates this target was part of the M10 sample. [(d)] The full explanation previous classifications is as follows, according to their recording papers. 1) Cieza et al. (2010): "PF"=Planet-forming disk, "GG"=Grain-growth dominated disk, "PE"=Photoevaportive disk. 2) Merín et al. (2008); Harvey et al. (2007): "L"=low infrared excess or anemic disk, "H"=high infrared excess, "T"=T Tauri-like infrared excess. 3) Others: "PTD" = pre-transitional disk, "V" = sea-saw variability.

Table A.2: Stellar parameters

ID	Name	SpT	T_{eff} (K)	A_V (mag)	L_* ($L_\odot$)	M_* ($M_\odot$)	EW[Hα] (Å)	FW10%[Hα][a] (km s^{-1})	Accretion[d] (Y/N)	Ref
1	TCha	K0	5250	2	1.34	1.1	-	400	Y	1,2
2	RECX11	K5	4350	0.4	0.73	1.2	4.4	330	Y	3
3	RECX5	M4	3370	2.4	0.14	0.3	35	330	Y	3
4	CHXR22E	M3.5	3370	4.9	0.26	0.4	-	-	U	4
5	ISO52	M4	3370	3	0.17	0.3	[b]	-	N	5
6	CSCha	K2	4780	1.3	1.88	1.5	[b]	-	Y	6
7	11094742-7726290	M3.25	3470	5.7	0.16	0.4	200	-	Y	7
9	T54	K0	5250	0	2.47	1.4	[b]	-	N	5
10	T21	G5	5770	3	15.19	2.3	-	-	U	4
11	SZCha	K2	4780	0.7	1.36	1.4	[b]	-	Y	6
12	T35	K7	4060	3.4	0.41	1	[b]	-	Y	6
13	ISO-ChaII29	M0	3850	4.3	0.57	1	1	249	N	8
14	T56	M0.5	3720	0.3	0.34	0.8	[b]	-	Y	6
15	CRCha	K0	5250	2.4	4.99	2	[b]	-	Y	5
16	WWCha	K5	4350	3.4	4.41	0.9	65	-	Y	9,4
17	11062554-7633418	M6	3050	6.9	0.17	0.1	43.6	-	Y	10
18	T25	M2.5	3470	2.3	0.33	0.5	[b]	-	Y	6
20	MPMus	K1	5080	0.9	1.35	1.2	-47	-	Y	11
21	HD142527	F6	6360	1.4	23.58	2.3	[c]	-	Y	12
22	J16232807-4015368	M3.5	3370	4.1	0.2	0.3	-0.4	-	N	13
23	Sz111	M1.5	3580	0.1	0.38	0.6	-	375	Y	14
24	Lup60	M4.5	3240	2.6	0.22	0.3	12.9	-	N	13
25	J160830.3-390611	M4	3370	3.7	0.47	0.5	-	426	Y	14
26	Sz104	M5	3240	1	0.19	0.3	-	201	Y	14
27	Sz91	M0.5	3720	0.8	0.29	0.7	-	374	Y	14
28	J160855.5-390234	M6	3050	0	0.22	0.1	-	189	Y	14
29	Sz84	M5	3240	2.7	0.32	0.3	[b]	-	Y	6
30	16182186-3730298	K5	4350	0.8	0.05	1	0.1	-	N	13
31	16225309-3724373	M5.5	3050	4.9	1.51	-	-	-	U	13
32	J19002346-3712242	-	(4060)	14	0.79	1	0.3	-	N	13
33	HD135344	F4	6590	0.8	11.48	1.8	[c]	-	Y	12
34	CrA-466	M2	3580	5.7	0.12	0.5	-14.5	-	N	15
35	Sz76	M1	3720	1.3	0.21	0.7	10.3	227	N	16
36	J154508.9-341734	M6	3050	8.4	0.49	0.1	174.5	-	Y	13
38	RXJ1615.3-3255	K7	4060	0	1.08	1.2	[b]	-	Y	6
39	V4046Sgr	K5	4350	0.5	0.73	1.2	26.7	-	Y	13
40	J163154.7-250324	K7	4060	4.6	0.88	1.2	-	470	Y	13,17
41	J163205.5-250236	M2	3580	2.9	0.12	0.5	-	567	Y	17
43	J163023.4-245416	M3	3470	4.2	0.38	0.5	88.7	-	Y	13
44	WSB63	M2	3580	3.9	0.38	0.6	-	365	Y	17
45	SR24S	K2	4780	5.8	2.07	1.5	[c]	-	Y	18
46	RXJ1633.9-2442	M0	3850	3.3	0.44	0.9	-	301	Y	13,17
47	ISO-Oph43	-	(4060)	15	0.41	1	-0.6	-	N	13
48	WSB60	M5.5	3050	5.8	0.38	0.1	[b]	-	Y	6
49	J163115.7-243402	K5	4350	1.9	2.53	0.9	-	450	Y	13,17
50	J162245.4-243124	M2	3580	2.9	0.38	0.6	[b]	-	Y	6
51	IRS48	A0	9520	10.6	14.5	1.9	[c]	-	Y	19
52	DoAr44	K3	4730	2.9	1.46	1.4	[b]	-	Y	6
53	J162435.2-242620	M4	3370	6.7	0.12	0.3	60.2	-	Y	13
54	SR21	G3	5830	5.5	6.5	1.7	[b]	-	Y	6
55	J162309.2-241705	G	5830	6	1.76	1.2	8.4	-	Y	13
56	J163136.8-240420	-	(4060)	11.2	0.04	-	-	-	U	
58	J162648.6-235634	K8	3960	3.3	0.43	1	28.4	-	Y	13,20
59	J162802.6-235504	M4	3370	5.2	0.2	0.3	-	159	N	13,17
60	oph62	M0	3850	3.7	0.28	0.9	[b]	-	Y	6
61	J162532.5-232626	M2.5	3470	1.5	0.19	0.4	7.4	-	N	13
62	J162218.5-232148	K5	4350	1.8	0.83	1.3	-	493	Y	13,17
63	DoAr28	K5	4350	2.6	0.73	1.2	44.5	-	Y	13
64	J160421.7-213028	K5	4350	0	0.55	1.1	5.3	-	Y	13
65	18015423-0437531	F3	6740	0.8	10.71	1.7	-4.3	-	N	13
66	18044921-0436413	M5	3240	6.6	3.45	-	32	-	Y	13
67	18270980-0414297	-	(4060)	6.7	3.92	0.6	-	-	U	
68	18272873-0406248	M-GIANT	-	-	-	-	-	-	N	13
69	18273408-0403247	B9	10500	4.4	39.52	2.4	-9.8	-	N	13
70	18273858-0402289	G5	5770	5.2	3.23	1.4	5.8	-	Y	13

Table A.2: Stellar parameters continued.

ID	Name	SpT	T_{eff} (K)	A_V (mag)	L_* ($L_\odot$)	M_* ($M_\odot$)	EW[Hα] (Å)	FW10%[Hα][a] (km s^{-1}	Accretion[d] (Y/N)	Ref
71	18255765-0357040	FG	6030	7.4	3.05	1.3	1.2	-	N	13
73	18291383-0342355	-	4060	14.4	7.14	0.7	-	-	U	
74	18284156-0341507	-	(4060)	10.6	1.53	1.2	-	-	U	
75	18283439-0339371	-	(4060)	13.2	3.92	0.6	-	-	U	
76	18272161-0314158	A0	9520	3.4	29.59	2.2	-9.2	-	N	13
77	18222604-0304383	F5	6440	4.5	4.48	1.4	-3.2	-	N	13
78	18330328-0244021	M5.5	3050	7	1.25	-	21.6	-	Y	13
79	18324685-0243273	A0	9520	1.8	23.97	2.2	-10.3	-	N	13
80	18304127-0242335	M-GIANT	-	-	-	-	-	-	N	13
81	18324783-0239401	FG	6030	10.8	4.3	1.4	-15.8	-	N	13
82	J18321275-0222377	-	(4060)	9.3	0.02	1	-	-	U	
83	18292883-0221157	M4.5	3240	6	0.22	0.3	68.5	-	Y	13
84	18291450-0220575	M-GIANT	-	-	-	-	-	-	N	13
85	18304121-0220189	-	(4060)	14	0.12	1	-	-	U	
86	J18314556-0218408	-	(4060)	14.9	0.12	1	-	-	U	
88	18311986-0208161	-	(4060)	11	2.83	1	-	-	U	
89	18323005-0204130	A6	8350	5.7	25.22	2	-5.7	-	N	13
90	18292804-0204042	-	(4060)	10.6	0.2	1	-	-	U	
91	18293961-0202414	-	(4060)	12	0.3	0.9	-	-	U	
92	J18303289-0200514	-	(4060)	14.9	0.12	1	-	-	U	
93	18311732-0200461	A0	9520	12.4	32.63	1	-	-	N	13
94	18312875-0159125	-	(4060)	14.9	2.83	0.6	-	-	U	
95	18315497-0157330	-	(4060)	8.7	0.71	1	-	-	U	
96	18313657-0157320	-	(4060)	7	1.92	1.3	-	-	U	
97	18313343-0155182	-	(4060)	9.3	0.06	1	-	-	U	
98	18315077-0153393	-	(4060)	11.4	0.12	1	-	-	U	
99	J18303321-0152563	A2	8970	2.7	16.85	1.9	-9.6	-	N	13
100	18295741-0151541	A7	7850	8.8	13.68	1.8	-6.6	-	N	13
101	18294721-0148301	-	(4060)	7.2	0.79	1.1	0.3	-	N	13
102	18293368-0145103	-	(4060)	19.8	0.35	1	-	-	U	
103	18290819-0139215	-	(4060)	15	0.88	1.2	-	-	U	
104	18314110-0128035	M-GIANT	-	-	-	-	-	-	N	13
105	18290391-0115357	FG	6030	8.7	3.86	1.4	1.7	-	N	13
106	18371575-0026561	A7	7850	1.9	46.82	2.5	-6.6	-	N	13
107	18381010-0023452	M3	3470	3.4	0.38	0.5	4.8	-	N	13
108	18371444-0023261	-	(4060)	7	8.52	-	-	-	U	
110	18385989-0008097	M-GIANT	-	-	-	-	-	-	N	13
111	J182813.5+000-249	K2	4780	3.8	4.23	1.6	13.4	-	Y	13,21
112	J182821.6+000016	-	(4060)	4	1.53	1.2	17.5	-	Y	13
113	18384257+0001324	FG	6030	5.2	0.19	-	-1.3	-	N	13
114	18392594+0006382	-	(4060)	7.1	8.52	-	-5.1	-	N	13
115	J182850.2+000950	K7	4060	7.5	1.53	1.2	131.3	-	Y	13,21
116	183549.4+001002	FG	6030	6.6	2.68	1	-1.5	-	N	13
117	18385571+0014431	GK	5250	4.7	0.99	1	-5.3	-	N	13
118	18394048+0014497	M1	3720	1	0.21	0.7	9.3	-	N	13
119	18374209+0016519	M-GIANT	-	-	-	-	-	-	N	13
120	J182911.5+002039	M2	3580	2.9	0.15	0.5	[b]	-	N	6
121	18375663-0023253	-	(4060)	3.8	0.12	1	-	-	U	
122	18381580+0024218	M-GIANT	-	-	-	-	-	-	N	13
123	J18295130+0027477	B8	11900	4	52.2	1	-9.1	-	N	13
124	serp22	-	(4060)	11	0.63	1.1	-	-	U	
125	18401205+0029276	F4	6590	8.9	5.5	1.4	42.7	-	Y	13
126	J182901.2+002933	M2	3580	1	0.21	1	88.6	-	Y	13,21
127	Serp127	M1	3720	2.8	0.76	0.8	[b]	-	Y	6
128	J182935.6+003504	K7	4060	3.8	1.41	1.2	10.9	273	Y	21
129	18381447+0035099	M-GIANT	-	-	-	-	-	-	N	13
130	18401486+0037042	K7	4060	4.3	0.2	0.8	38	-	Y	13
131	Serp111	-	(4060)	5.1	0.63	1.1	9.8	-	Y	13
132	J182955.3+004939	A2	8970	5.6	39.42	2.2	9.9	-	Y	13,21
133	J183008.6+005847	K5	4350	0.7	1.04	1.4	7.4	-	Y	13,21
134	RXJ0432.8+1735	M2	3580	0.7	0.38	0.6	1.4	-	N	13
135	DMTau	M1	3720	0.7	0.25	0.7	[b]	-	Y	6
136	UXTauA	K2	4780	0.8	1.88	1.5	9.5	-	Y	22
137	043339.0+222720	M2.5	3470	2	0.03	0.4	28	-	Y	13,23
138	043326.2+224529	M3	3470	5.6	0.29	0.5	4.2	-	N	13,23
139	J04390525+2337450	K5	4350	5.1	0.08	-	18.2	-	Y	13,23

Table A.2: Stellar parameters continued.

ID	Name	SpT	T_{eff} (K)	A_V (mag)	L_* ($L_\odot$)	M_* ($M_\odot$)	EW[Hα] (Å)	FW10%[Hα][a] (km s^{-1})	Accretion[d] (Y/N)	Ref
140	043649.1+241258	F2	6890	1.5	3.98	1.4	-5.5	-	N	23
142	MWC758	A8	7580	0.7	34.37	2.3	[c]	-	Y	24
144	044555.7+261858	K1	5080	3	0.15	-	-1.1	-	N	13,23
145	DHTauAB	M1	3720	0.5	0.44	0.8	-	348	Y	23,25
146	043044.7+263308	K3	4730	2.6	3.54	1.5	-1.1	-	N	23
147	J04214631+2659296	M6	3050	3	0.02	0.1	17.3	-	N	23
148	IPTau	M0	3850	0.6	0.51	0.9	11	-	Y	22
149	V892Tau	B8	11900	9.5	131.67	3.1	-	-	U	26
150	V410X-ray6	M4.5	3240	1.7	0.32	0.3	-	210	N	23
151	042254.6+282354	A0	9520	0.9	16.65	1.9	10	-	Y	23
152	V819Tau	K7	4060	1.1	0.79	1.1	-	180	N	23
153	RYTau	G1	5945	2.8	17.11	2.3	[c]	-	Y	27
154	V410X-ray2	M0	3850	17	1.05	1	-	-	U	23
155	041542.7+290959	M1.25	3720	2.8	0.34	0.8	2.3	-	N	28
156	041332.3+291726	G5	5770	2.4	0.04	-	-2.4	-	N	13
157	J032800.1+300847	M5	3240	3.7	0.44	0.2	21.8	-	Y	13
158	LkCa19	K0	5250	1	1.75	1.2	-1.2	110	N	16
159	ABAur	A0	9520	1.6	112.53	3.1	[c]	-	Y	29,24
160	J033341.3+311341	K4	4560	5.7	0.19	0.8	205	-	Y	13
161	ASR118	K4	4560	5.7	0.19	0.8	17.6	-	Y	13,30
162	MBO22	M0	3850	2.5	0.2	0.8	4.8	-	N	30
163	J032856.6+311836	K6	4205	3.3	0.34	1	104.7	-	Y	13
164	J034219.3+314327	-	(4060)	7	0.3	0.9	64.7	-	Y	13
165	J034227.1+314433	K7	4060	7.1	0.35	1	4.3	-	N	30
166	J034109.1+314438	FG	6030	5.4	3.86	1.4	-1.2	-	N	13
167	J034355.2+315532	K	4730	9.3	0.37	0.8	-2.9	-	N	13
168	J034434.8+315655	M3	3470	3.1	0.16	0.4	130	504	Y	30
169	IC348LRL190	M4	3370	7.9	0.14	0.3	-5.7	-	N	13,30
171	J034520.5+320634	M1	3720	2.6	0.69	0.8	11.5	-	N	31
172	IC348-67	M0.75	3720	0.7	0.17	0.7	-	280	N	32
173	LkH-alpha330	G3	5830	3	12.75	2.2	[b]	-	Y	6
174	J04300424+3522238	M0	3850	2.1	0.33	0.9	-	370	Y	13,32
175	J04303235+3536133	M0	3850	3.2	0.16	0.8	-	350	Y	13,32
176	04300980+3540355	M4	3370	4.1	0.02	0.3	10.3	-	N	13
177	J04304004+3542101	K7	4060	2.7	0.09	0.6	-	310	Y	32
178	J04303831+3549591	-	(4060)	8.8	0.09	1	-	-	U	
179	J160044.5-415531	K0	5250	1.3	1.34	1.1	-	532	Y	33
180	J190058.1-364505	M0.75	3720	1.9	0.39	0.8	-	440	Y	33
181	03445614+3209152	K0	5250	4.8	2.22	1.3	-	360	Y	32
182	03442156+3215098	M2	3580	1.1	0.09	0.5	-	130	N	32
183	03442257+3201536	M2	3580	2.1	0.25	0.6	-	140	N	32
184	04330422+2921499	B9	10500	2.8	79.81	2.7	-	-	N	32
185	J160825.76-390601.1	M5	3240	0	0.22	0.3	[b]	-	Y	14
186	RXJ1556.1-3655	M1	3720	0	0.25	0.7	82.6	416	Y	16
187	043150.5+242418	M0.5	3720	1.5	0.29	0.7	29.3	-	Y	23,34
188	041413.5+281249	M0	3850	1	0.33	0.9	99	-	Y	23
189	041841.3+282725	K5	4350	20.4	0.32	0.9	-	-	U	23
190	042025.5+270035	M2.25	3580	1.5	0.04	0.5	-	-	U	23
191	042921.6+270125	M6	3050	4.1	0.49	0.1	-	-	U	23
192	043249.1+225302	K6	4205	2.5	0.55	1.1	22	-	Y	23,35
193	044221.0+252034	M4.5	3240	4.3	0.29	0.3	114.6	-	Y	13
194	041539.1+281858	M5	3240	4	0.57	0.2	997.2	-	Y	23
195	042318.2+264115	M3.5	3370	8.6	0.26	0.4	-	-	U	23
196	041414.5+282758	M3.5	3370	3.7	1.34	0.3	-	-	N	36
197	041915.8+290626	K7	4060	2.5	1.65	1.2	-	458	Y	23,25
198	042155.6+275506	M1	3720	0.9	0.83	0.8	-	453	Y	25
200	J160710.08-391103.5	M0	3850	0.5	0.57	1	24.2	-	Y	13
201	J032741.47+302016.8	M3	3470	1.7	0.52	0.5	51.3	-	Y	13
202	J034345.17+320358.6	-	(4060)	7.1	0.25	1	150.2	-	Y	13
203	J182815.26-000243.3	-	(4060)	5.4	3.17	0.6	-	-	U	
204	J162715.89-243843.2	-	(4060)	16.1	0.63	1	-	-	U	
301	J130455.7-773949	M0.5	3720	0.7	0.5	0.8	0.2	311	N	30
303	J160115.5-415235	-	(4060)	12.8	0.04	-	-	0	U	
307	16083070-3828268	-	(4060)	0	2.2	1.3	-	0	U	
309	TWHya	K6	4205	1.3	0.34	1	[b]	-	Y	6
310	15395742-3414567	-	(4060)	0.5	0.02	-	-	0	U	

Table A.2: Stellar parameters continued.

ID	Name	SpT	T_{eff} (K)	A_V (mag)	L_* ($L_\odot$)	M_* ($M_\odot$)	EW[Hα] (Å)	FW10%[Hα][a] (km s^{-1})	Accretion[d] (Y/N)	Ref
314	16281385-2456113	-	(4060)	4.6	0.25	0.9	-	0	U	
316	16271587-2438433	-	(4060)	16.1	0.63	1	-	0	U	
317	16312019-2430009	-	(4060)	2.2	2.35	1	-	0	U	
318	DoAr21	K1	5080	5.5	8.66	2.4	1.5	450	N	30
319	J162740.3-242204	K7	4060	1.9	2.06	1.3	29.2	-	Y	13
321	Serp48	F6	6360	4.4	9.96	1.7	-2.3	-	N	13,21
322	18302986+0035004	-	(4060)	2.3	0.71	1.1	-	0	U	
325	LkCa15	K3	4730	1.2	1.01	1.2	[b]	-	Y	6
326	CoKu-Tau-4	M1	3720	0.1	0.29	0.7	-	185	N	23,25
329	GMAur	K5	4350	0.3	0.83	1.3	[b]	-	Y	6
333	03370363+3039291	-	(4060)	0	2.35	1.3	-	0	U	
334	03401579+3055047	-	(4060)	2.7	0.01	-	-	0	U	
335	J033234.0+310056	K6	4205	4	1.02	1.3	71.4	-	Y	13,30
348	UScoJ155837.1-225724	G7	5630	0.6	3.27	1.4	-	-	U	37
349	RXJ1842.9-3532	K2	4780	0.7	0.92	1.2	[b]	-	Y	6
350	RXJ1852.3-3700	K2	4780	0.7	0.68	1	[b]	-	Y	6

Refs. 1) Alcala et al. (1995), 2) Schisano et al. (2009), 3) Lawson et al. (2004), 4) Luhman (2007), 5) Manara et al. (2015), 6) Manara et al. (2014), 7) Luhman & Muench (2008), 8) Spezzi et al. (2008), 9) Luhman (2004), 10) Comerón et al. (2004), 11) Silverstone et al. (2006), 12) Garcia Lopez et al. (2006), 13) This work, 14) Alcalá et al. (2014), 15) Sicilia-Aguilar et al. (2008), 16) Wahhaj et al. (2010), 17) Cieza et al. (2010), 18) Natta et al. (2006), 19) Brown et al. (2012), 20) Wilking et al. (2005), 21) Oliveira et al. (2009), 22) White & Ghez (2001), 23) Rebull et al. (2010), 24) Salyk et al. (2013), 25) Nguyen et al. (2012), 26) Furlan et al. (2006), 27) Calvet et al. (2004), 28) Furlan et al. (2011), 29) Mooley et al. (2013), 30) Merín et al. (2010), 31) Cieza et al. (2007), 32) Cieza et al. (2012b), 33) Romero et al. (2012), 34) Rigliaco et al. (2015), 35) Kraus & Hillenbrand (2009), 36) Herczeg & Hillenbrand (2014), 37) Carpenter et al. (2008)

Notes. [(a)] We have reversed the signs of the width of the Hα line taken from Rebull et al. (2010) and Winston et al. (2009), as they list a negative value for emission and positive for absorption. [(b)] The accretion properties have been derived using a full X-shooter spectrum rather than only fitting the Hα line. [(c)] The accretion properties have been derived using other lines (e.g. Brγ). [(d)] 'Y' means accreting, 'N' means non-accreting', 'U' means unknown.

Table A.3: Results of disk fitting procedure and classification

ID	Name	r_{cav} (AU)	Σ_c (g cm^{-2})	$M_{disk,fit}$[a] (M_{Jup})	δ_{dust}	h_c	ψ	$M_{disk,mm}$[a] (M_{Jup})	L_{disk}/L_*	Classification[b]
1	TCha	140^{+10}_{-10}	7E-02	7.8	1E-02	0.10	1/7.	3.7	0.467	ML
2	RECX11	6^{+4}_{-4}	3E-03	1.1	1E-02	0.01	1/7.	< 1.5	0.067	LS
3	RECX5	10^{+2}_{-2}	3E-04	0.1	1E-04	0.01	1/7.	-	0.038	LL
4	CHXR22E	45^{+15}_{-5}	3E-04	0.1	1E-06	0.01	2/7.	-	0.178	LL
5	ISO52	30^{+50}_{-18}	3E-03	0.9	1E-01	0.05	2/7.	-	0.195	LL
6	CSCha	60^{+10}_{-10}	8E-02	20.9	1E-06	0.05	1/7.	20.6	0.105	ML
7	11094742-7726290	8^{+2}_{-2}	3E-03	1.1	1E-02	0.15	1/7.	-	0.685	LS
9	T54	120^{+20}_{-10}	3E-04	0.0	1E-03	0.01	1/7.	< 1.6	0.008	DD
10	T21	190_{-10}	3E-04	0.0	1E-02	0.01	1/7.	< 2.1	0.001	DD
11	SZCha	30^{+10}_{-10}	5E-02	15.8	1E-04	0.05	2/7.	32.8	0.329	ML
12	T35	15^{+5}_{-5}	3E-03	1.0	1E-03	0.05	1/7.	< 22.2	0.183	LL
13	ISO-ChaII29	190_{-10}	1E-02	0.2	1E-04	0.01	1/7.	-	0.007	DD
14	T56	10^{+4}_{-4}	3E-02	10.6	1E-04	0.05	1/7.	2.5	0.201	ML
15	CRCha	1^{+1}	2E-01	55.6	1E+00	0.03	1/7.	43.9	0.083	MS
16	WWCha	50^{+30}_{-49}	4E-01	106.1	1E-01	0.20	1/7.	-	0.934	ML
17	11062554-7633418	15^{+15}_{-5}	3E-03	1.0	1E-06	0.05	2/7.	-	0.172	LL
18	T25	30^{+5}_{-5}	3E-03	0.9	1E-06	0.05	1/7.	2.1	0.139	LL
20	MPMus	1^{+3}	1E-01	37.1	1E+00	0.04	1/7.	15.9	0.17	MS
21	HD142527	110^{+10}_{-20}	6E-01	100.6	1E-01	0.10	1/7.	216	0.366	ML
22	J16232807-4015368	50^{+40}_{-10}	5E-03	1.4	1E-06	0.05	1/7.	-	0.465	LL
23	Sz111	60^{+10}_{-10}	1E-01	26.1	1E-06	0.05	2/7.	25	0.152	ML
24	Lup60	16^{+2}_{-4}	3E-03	1.0	1E-06	0.02	1/7.	< 3.8	0.151	LL
25	J160830.3-390611	4^{+4}_{-2}	3E-03	1.1	1E-04	0.01	1/7.	-	0.1	LS
26	Sz104	2^{+2}	3E-04	0.1	1E-02	0.05	1/7.	< 5.0	0.307	LS
27	Sz91	120^{+30}_{-20}	2E-02	3.4	1E-06	0.05	1/7.	5.7	0.17	LL
28	J160855.5-390234	2^{+2}	3E-04	0.1	1E-02	0.10	1/7.	< 3.4	0.434	LS
29	Sz84	70^{+40}_{-10}	6E-02	14.5	1E-08	0.02	1/7.	2.8	0.136	ML
31	16225309-3724373	170^{+10}_{-20}	3E-04	0.0	1E-02	0.01	1/7.	-	0.193	DD
33	HD135344	80^{+10}_{-10}	2E-01	33.5	1E-01	0.05	1/7.	49.6	0.233	ML
34	CrA-466	10^{+4}_{-4}	3E-04	0.1	1E-02	0.20	1/7.	-	0.25	LL
35	Sz76	2^{+2}	9E-02	33.2	1E-02	0.02	1/7.	< 2.8	0.104	MS
36	J154508.9-341734	1	2E-02	5.6	1E+00	0.05	1/7.	6.7	0.337	NH
38	RXJ1615.3-3255	10^{+10}_{-2}	5E-01	159.2	1E-06	0.03	1/7.	60.1	0.094	ML
39	V4046Sgr	16^{+4}_{-6}	1E-01	34.3	1E-04	0.03	1/7.	16.8	0.117	ML
40	J163154.7-250324	1	3E-03	1.1	1E+00	0.10	1/7.	< 1.3	0.434	NH
41	J163205.5-250236	1	3E-04	0.1	1E+00	0.05	1/7.	< 1.3	0.107	NH
43	J163023.4-245416	45^{+5}_{-20}	1E-03	0.3	1E-01	0.15	2/7.	< 1.1	0.257	LL
44	WSB63	4^{+2}_{-2}	7E-03	2.6	1E-04	0.05	1/7.	2.4	0.146	LS
45	SR24S	50^{+40}_{-20}	6E-02	16.8	1E-01	0.20	1/7.	35.1	0.764	ML
46	RXJ1633.9-2442	20^{+10}_{-5}	3E-02	10.1	1E-06	0.05	1/7.	10.5	0.114	ML
47*	ISO-Oph43	1^{+1}	3E-03	1.1	1E+00	0.05	1/7.	-	0.27	LS
48	WSB60	8^{+6}_{-7}	3E-02	10.7	1E-02	0.05	1/7.	-	0.35	MS
49	J163115.7-243402	20^{+30}_{-10}	3E-03	1.0	1E-01	0.01	1/7.	< 0.8	0.048	LL
50	J162245.4-243124	2^{+2}	1E-03	0.4	1E-04	0.01	1/7.	< 0.7	0.11	LS
51	IRS48	120^{+10}_{-100}	2E-02	3.0	1E-04	0.10	1/7.	11.5	0.31	LL
52	DoAr44	80^{+10}_{-20}	3E-02	5.6	1E-02	0.10	1/7.	13.4	0.345	ML
53	J162435.2-242620	1	3E-02	11.1	1E+00	0.01	1/7.	-	0.054	NH
54	SR21	60^{+20}_{-15}	3E-02	7.8	1E-01	0.10	2/7.	34.3	0.356	ML
55*	J162309.2-241705	1	2E-02	7.8	1E+00	0.03	1/7.	5.9	0.227	NH
56*	J163136.8-240420	4^{+6}_{-2}	1E-02	3.6	1E-06	0.20	1/7.	-	0.842	LS
58	J162648.6-235634	1	8E-04	0.3	1E+00	0.15	1/7.	< 1.1	0.418	NH
59	J162802.6-235504	2^{+2}	3E-04	0.1	1E-04	0.01	1/7.	-	0.115	LS
60	oph62	2^{+2}	3E-03	1.1	1E-06	0.01	2/7.	< 1.5	0.062	LS
61	J162532.5-232626	5^{+85}_{-3}	3E-04	0.1	1E-02	0.05	1/7.	-	0.192	LS
62	J162218.5-232148	1	1E-02	4.4	1E+00	0.05	1/7.	4	0.238	NH
63	DoAr28	20^{+5}_{-5}	4E-02	11.7	1E-06	0.03	1/7.	6.1	0.087	ML
64	J160421.7-213028	70^{+20}_{-30}	5E-02	12.1	1E-04	0.08	1/7.	20.4	0.359	ML
65	18015423-0437531	190_{-10}	3E-04	0.0	1E-06	0.01	1/7.	-	0.001	DD
66	18044921-0436413	30^{+10}_{-26}	3E-03	0.9	1E-03	0.05	1/7.	-	0.276	LL
67*	18270980-0414297	110^{+10}_{-10}	3E-04	0.1	1E-06	0.01	1/7.	-	0.004	DD
69	18273408-0403247	190_{-10}	3E-04	0.0	1E-06	0.01	1/7.	-	0.001	DD
70	18273858-0402289	80^{+30}_{-10}	6E-02	13.4	1E-04	0.03	1/7.	8.3	0.077	ML
71*	18255765-0357040	180^{+10}_{-20}	3E-04	0.0	1E-04	0.01	1/7.	-	0.003	DD
73*	18291383-0342355	190_{-10}	3E-02	0.6	1E-04	0.01	1/7.	-	0.011	DD

Table A.3: Fitting results continued

ID	Name	$r_{\rm cav}$ (AU)	Σ_c (g cm^{-2})	$M_{\rm disk,fit}$[a] ($M_{\rm Jup}$)	$\delta_{\rm dust}$	h_c	ψ	$M_{\rm disk,mm}$[a] ($M_{\rm Jup}$)	$L_{\rm disk}/L_*$	Classification[b]
74*	18284156-0341507	140^{+10}_{-100}	3E-02	3.4	1E-04	0.01	1/7.	-	0.025	DD
75*	18283439-0339371	190_{-20}	3E-02	0.6	1E-04	0.01	1/7.	-	0.013	DD
76	18272161-0314158	190_{-10}	3E-04	0.0	1E-06	0.01	1/7.	-	0.002	DD
77	18222604-0304383	190_{-10}	3E-04	0.0	1E-06	0.01	1/7.	-	0.002	DD
79	18324685-0243273	190_{-10}	3E-04	0.0	1E-06	0.01	1/7.	-	0	DD
81*	18324783-0239401	70^{+30}_{-10}	3E-03	0.7	1E-02	0.05	1/7.	-	0.129	LL
83	18292883-0221157	2^{+16}	3E-03	1.1	1E-04	0.01	2/7.	-	0.053	LS
89	18323005-0204130	110^{+40}_{-10}	3E-05	0.0	1E-06	0.10	1/7.	< 9.0	0.004	LL
91*	18293961-0202414	30^{+50}_{-25}	3E-02	9.5	1E-02	0.10	1/7.	-	0.272	ML
94*	18312875-0159125	190_{-150}	3E-04	0.0	1E-04	0.10	1/7.	-	0.01	LL
96*	18313657-0157320	60^{+50}_{-30}	3E-04	0.1	1E-04	0.05	1/7.	-	0.039	LL
99	J18303321-0152563	190_{-10}	6E+00	111.7	1E-10	0.01	2/7.	91.8	0.025	ML
100	18295741-0151541	190_{-10}	6E-01	11.2	1E-06	0.01	1/7.	< 9.4	0.016	ML
101*	18294721-0148301	5^{+85}_{-2}	1E-01	36.3	1E-06	0.01	1/7.	-	0.045	MS
102*	18293368-0145103	45^{+115}_{-40}	3E-02	8.7	1E-01	0.20	1/7.	-	0.702	ML
103*	18290819-0139215	40^{+5}_{-5}	3E-02	8.9	1E-01	0.10	1/7.	-	0.338	ML
105*	18290391-0115357	190_{-10}	3E-04	0.0	1E-04	0.01	1/7.	-	0.002	DD
106	18371575-0026561	190_{-10}	3E-04	0.0	1E-04	0.01	1/7.	-	0.001	DD
107	18381010-0023452	70^{+40}_{-20}	3E-04	0.1	1E-06	0.10	1/7.	< 4.4	0.047	LL
108*	18371444-0023261	180^{+10}_{-40}	3E-04	0.0	1E-02	0.05	1/7.	-	0.011	LL
111	J182813.5+000-249	1	3E-01	111.2	1E+00	0.05	1/7.	-	0.207	NH
112*	J182821.6+000016	1	3E-03	1.1	1E+00	0.10	1/7.	-	0.304	NH
113*	18384257+0001324	60^{+20}_{-20}	3E-03	0.8	1E-06	0.05	2/7.	-	0.167	LL
114*	18392594+0006382	180^{+10}_{-130}	3E-03	0.1	1E-06	0.01	1/7.	-	0.01	DD
115	J182850.2+000950	5^{+35}_{-4}	5E-03	1.8	1E-01	0.20	1/7.	< 12.4	0.889	LS
117*	18385571+0014431	60^{+40}_{-10}	3E-04	0.1	1E-06	0.01	1/7.	-	0.019	LL
118	18394048+0014497	2^{+2}	3E-04	0.1	1E-02	0.15	1/7.	-	0.397	LS
120	J182911.5+002039	10^{+5}_{-8}	3E-03	1.1	1E-06	0.05	1/7.	< 5.4	0.17	LL
124*	serp22	10^{+10}_{-5}	3E-03	1.1	1E-04	0.05	1/7.	-	0.118	LL
125	18401205+0029276	50^{+10}_{-49}	3E-02	8.4	1E-01	0.20	1/7.	-	0.927	ML
127	Serp127	80^{+20}_{-10}	5E-02	10.1	1E-05	0.03	2/7.	< 7.5	0.086	ML
128	J182935.6+003504	25^{+45}_{-24}	3E-03	1.0	1E-02	0.05	1/7.	-	0.086	LL
130	18401486+0037042	30^{+40}_{-25}	3E-04	0.1	1E-06	0.10	1/7.	-	0.077	LL
131*	Serp111	10^{+10}_{-5}	1E-02	3.5	1E-03	0.05	1/7.	1.2	0.257	LL
132	J182955.3+004939	180^{+10}_{-176}	5E-01	18.6	1E-04	0.05	1/7.	27.8	0.146	ML
133	J183008.6+005847	1	3E-02	11.1	1E+00	0.15	1/7.	-	0.582	NH
134	RXJ0432.8+1735	190_{-10}	3E-04	0.0	1E-04	0.01	1/7.	-	0.006	DD
135	DMTau	4^{+2}_{-2}	9E-02	32.8	1E-06	0.05	1/7.	16.8	0.121	MS
136	UXTauA	50^{+40}_{-10}	3E-02	7.0	1E-04	0.05	1/7.	12	0.206	ML
137	043339.0+222720	4^{+2}_{-2}	4E-02	14.6	1E-01	0.20	2/7.	5.1	1.236	MS
138	043326.2+224529	180^{+10}_{-20}	3E-03	0.1	1E-06	0.01	1/7.	-	0.1	DD
139	J04390525+2337450	2^{+2}	3E-03	1.1	1E-03	0.10	1/7.	-	0.603	LS
140	043649.1+241258	190_{-10}	3E-04	0.0	1E-05	0.01	1/7.	< 2.2	0.001	DD
142	MWC758	25^{+15}_{-5}	3E-02	9.8	1E-01	0.05	1/7.	29.4	0.203	ML
144	044555.7+261858	110^{+40}_{-10}	3E-03	0.5	1E-06	0.01	1/7.	-	0.037	DD
145	DHTauAB	1^{+1}	2E-02	5.6	1E+00	0.10	1/7.	3.9	0.328	MS
146	043044.7+263308	190_{-10}	3E-04	0.0	1E-04	0.01	1/7.	-	0.001	DD
147	J04214631+2659296	6^{+9}_{-2}	3E-02	10.8	1E-01	0.05	2/7.	-	0.426	MS
148	IPTau	100^{+10}_{-30}	1E-02	2.2	1E-01	0.10	1/7.	2.7	0.235	LL
149	V892Tau	10^{+8}_{-8}	3E-02	10.6	1E-06	0.03	1/7.	51	0.153	ML
150	V410X-ray6	15^{+5}_{-5}	3E-04	0.1	1E-06	0.10	2/7.	< 0.6	0.291	LL
151	042254.6+282354	190_{-10}	1E-04	0.0	1E-06	0.05	1/7.	-	0.001	LL
152	V819Tau	150^{+20}_{-20}	3E-04	0.0	1E-04	0.01	1/7.	< 0.7	0.003	DD
153	RYTau	2^{+2}	3E-02	11.1	1E-02	0.10	1/7.	44.8	0.385	MS
154	V410X-ray2	6^{+2}_{-2}	6E-02	21.7	1E-04	0.02	1/7.	-	0.082	MS
155	041542.7+290959	50^{+10}_{-5}	1E-02	3.4	1E-06	0.05	1/7.	4.4	0.141	LL
156	041332.3+291726	10^{+60}_{-5}	1E-02	3.5	1E-06	0.01	2/7.	< 2.5	0.033	LL
157	J032800.1+300847	1^{+4}	3E-03	1.1	1E+00	0.05	1/7.	-	0.325	LS
158	LkCa19	190_{-10}	3E-04	0.0	1E-06	0.01	1/7.	-	0.001	DD
159	ABAur	1^{+5}	2E-02	8.2	1E+00	0.05	1/7.	28.7	0.152	MS
160	J033341.3+311341	1	1E-01	37.1	1E+00	0.20	1/7.	-	1.191	NH
161	ASR118	2^{+4}	8E-03	2.9	1E-03	0.20	1/7.	< 29.4	0.785	LS
162	MBO22	2^{+2}	2E-02	5.5	1E-06	0.05	2/7.	3.4	0.321	MS
163	J032856.6+311836	1^{+1}	3E-02	11.1	1E+00	0.20	1/7.	< 29.9	0.978	MS

Table A.3: Fitting results continued

ID	Name	r_{cav} (AU)	Σ_c (g cm^{-2})	$M_{disk,fit}$[a] (M_{Jup})	δ_{dust}	h_c	ψ	$M_{disk,mm}$[a] (M_{Jup})	L_{disk}/L_*	Classification[b]
164*	J034219.3+314327	1^{+3}	1E-03	0.4	1E+00	0.20	1/7.	-	0.505	LS
165	J034227.1+314433	8^{+4}_{-4}	1E-03	0.4	1E-04	0.02	1/7.	< 0.8	0.052	LS
166*	J034109.1+314438	140^{+20}_{-10}	2E-01	16.8	1E-01	0.15	1/7.	42.5	0.424	ML
167*	J034355.2+315532	8^{+42}_{-4}	3E-02	10.7	1E-04	0.05	1/7.	-	0.238	MS
168	J034434.8+315655	5^{+20}_{-3}	3E-03	1.1	1E-04	0.05	1/7.	< 0.8	0.177	LL
169	IC348LRL190	2^{+2}	3E-04	0.1	1E-04	0.02	1/7.	-	0.194	LS
171	J034520.5+320634	1	1E-02	4.4	1E+00	0.10	1/7.	4.4	0.343	NH
172	IC348-67	2^{+1}	3E-02	11.8	1E-06	0.10	1/7.	7.9	0.384	MS
173	LkH-alpha330	120^{+10}_{-20}	3E-01	44.7	1E-04	0.05	1/7.	53.6	0.331	ML
174	J04300424+3522238	18^{+10}_{-6}	9E-02	30.5	1E-06	0.05	1/7.	< 22.2	0.257	ML
175	J04303235+3536133	4^{+8}_{-2}	2E-03	0.5	1E-04	0.15	2/7.	0.8	0.542	LS
176	04300980+3540355	2^{+2}	3E-03	1.1	1E-06	0.05	2/7.	-	0.195	LS
177	J04304004+3542101	25^{+10}_{-10}	6E-03	2.0	1E-06	0.01	1/7.	< 0.4	0.019	LL
179	J160044.5-415531	1^{+59}	2E-02	7.4	1E+00	0.05	1/7.	9.2	0.141	MS
180	J190058.1-364505	14^{+4}_{-4}	3E-04	0.1	1E-06	0.05	1/7.	< 1.8	0.071	LL
181	03445614+3209152	6^{+12}_{-5}	3E-03	1.1	1E+00	0.01	1/7.	< 0.6	0.067	LS
182	03442156+3215098	2^{+23}	1E-02	3.7	1E-04	0.01	1/7.	-	0.044	LS
183	03442257+3201536	4^{+1}_{-2}	3E-03	1.1	1E-06	0.05	1/7.	< 0.8	0.119	LS
184	04330422+2921499	160^{+20}_{-10}	1E-04	0.0	1E-04	0.01	1/7.	< 1.5	0.003	DD
185	J160825.76-390601.1	1	1E-02	3.7	1E+00	0.12	1/7.	< 9.4	0.582	NH
186	RXJ1556.1-3655	1	3E-04	0.1	1E+00	0.10	2/7.	-	0.274	NH
187	043150.5+242418	4^{+2}_{-2}	3E-02	9.9	1E-01	0.20	1/7.	10	1.076	MS
188	041413.5+281249	1	5E-03	1.9	1E+00	0.15	1/7.	2.6	0.452	NH
189	041841.3+282725	40^{+80}_{-30}	3E-02	8.9	1E-01	0.07	1/7.	-	0.302	ML
190	042025.5+270035	2^{+2}	2E-02	5.5	1E-04	0.05	1/7.	1.4	0.147	MS
191	042921.6+270125	2^{+2}	1E-03	0.4	1E-02	0.05	1/7.	-	0.449	LS
192	043249.1+225302	25^{+10}_{-10}	3E-03	1.0	1E-02	0.20	1/7.	< 2.3	0.617	LL
193	044221.0+252034	10^{+10}_{-8}	8E-03	2.8	1E-04	0.05	1/7.	2.6	0.125	LL
194	041539.1+281858	10^{+2}_{-5}	7E-02	24.8	1E-05	0.02	1/7.	2.3	0.157	ML
195	042318.2+264115	2^{+2}	3E-04	0.1	1E-02	0.05	1/7.	-	0.264	LS
196	041414.5+282758	2^{+2}	1E-02	4.1	1E-04	0.05	1/7.	5.5	0.219	LS
197	041915.8+290626	1	3E-02	11.1	1E+00	0.03	1/7.	10.4	0.114	NH
198	042155.6+275506	90^{+50}_{-10}	2E-02	4.1	1E-02	0.15	1/7.	7.2	0.314	LL
200	J160710.08-391103.5	1	2E-02	7.4	1E+00	0.10	1/7.	< 6.5	0.397	NH
201	J032741.47+302016.8	1^{+3}	7E-02	25.9	1E+00	0.05	1/7.	-	0.34	MS
203*	J182815.26-000243.3	2^{+98}	4E-02	14.7	1E-01	0.10	2/7.	-	0.9	MS
301	J130455.7-773949	2^{+2}	3E-02	11.1	1E-02	0.05	1/7.	-	0.242	MS
303*	J160115.5-415235	4^{+6}_{-2}	7E-02	25.5	1E-04	0.20	2/7.	-	2.82	MS
307*	16083070-3828268	160^{+10}_{-20}	5E-02	3.4	1E-06	0.05	2/7.	-	0.107	LL
309	TWHya	10^{+2}_{-2}	3E-02	10.6	1E-04	0.02	1/7.	-	0.066	ML
310*	15395742-3414567	20^{+60}_{-14}	6E-01	201.1	1E-02	0.20	2/7.	-	1.477	ML
314*	16281385-2456113	20^{+10}_{-10}	1E-02	3.4	1E-06	0.05	1/7.	-	0.146	LL
318	DoAr21	70^{+30}_{-10}	3E-04	0.1	1E-02	0.05	2/7.	-	0.048	LL
319	J162740.3-242204	1^{+17}	3E-03	1.1	1E+00	0.05	1/7.	-	0.116	LS
321	Serp48	190_{-10}	3E-03	0.1	1E-05	0.01	1/7.	< 5.1	0.018	DD
322*	18302986+0035004	70^{+10}_{-10}	3E-01	72.6	1E-08	0.05	1/7.	-	0.225	ML
325	LkCa15	80^{+40}_{-35}	1E-01	29.0	1E-01	0.05	1/7.	32.8	0.159	ML
326	CoKu-Tau-4	6^{+2}_{-2}	3E-02	10.8	1E-06	0.10	1/7.	-	0.46	MS
329	GMAur	30^{+10}_{-5}	2E-01	50.6	1E-04	0.05	2/7.	51.2	0.211	ML
333*	03370363+3039291	50^{+30}_{-10}	1E-02	2.8	1E-05	0.10	1/7.	-	0.533	LL
334*	03401579+3055047	8^{+112}_{-7}	3E-01	107.3	1E-01	0.20	2/7.	-	1.528	MS
335	J033234.0+310056	2^{+8}_{-1}	3E-01	110.6	1E-01	0.05	2/7.	-	0.28	MS
348	UScoJ155837.1-225724	20^{+10}_{-8}	3E-03	1.0	1E-01	0.10	1/7.	-	0.328	LL
349	RXJ1842.9-3532	160^{+10}_{-10}	3E-01	22.3	1E-04	0.05	1/7.	8.9	0.201	ML
350	RXJ1852.3-3700	10^{+2}_{-2}	6E-02	21.2	1E-06	0.03	1/7.	-	0.228	ML

Notes. [(*)] Fit results are uncertain due to unknown spectral type. [(a)] Disk masses refer to the full disk mass, computed assuming a gas-to-dust ratio of 100. [(b)] NH = disks without holes, ML = massive disks with large holes, MS = massive disks with small holes, LL = low-mass disks with large holes, LS = low-mass disks with small holes, DD = low-mass disks with very low scale heights. See also definition in the text.

Appendix B: SEDs

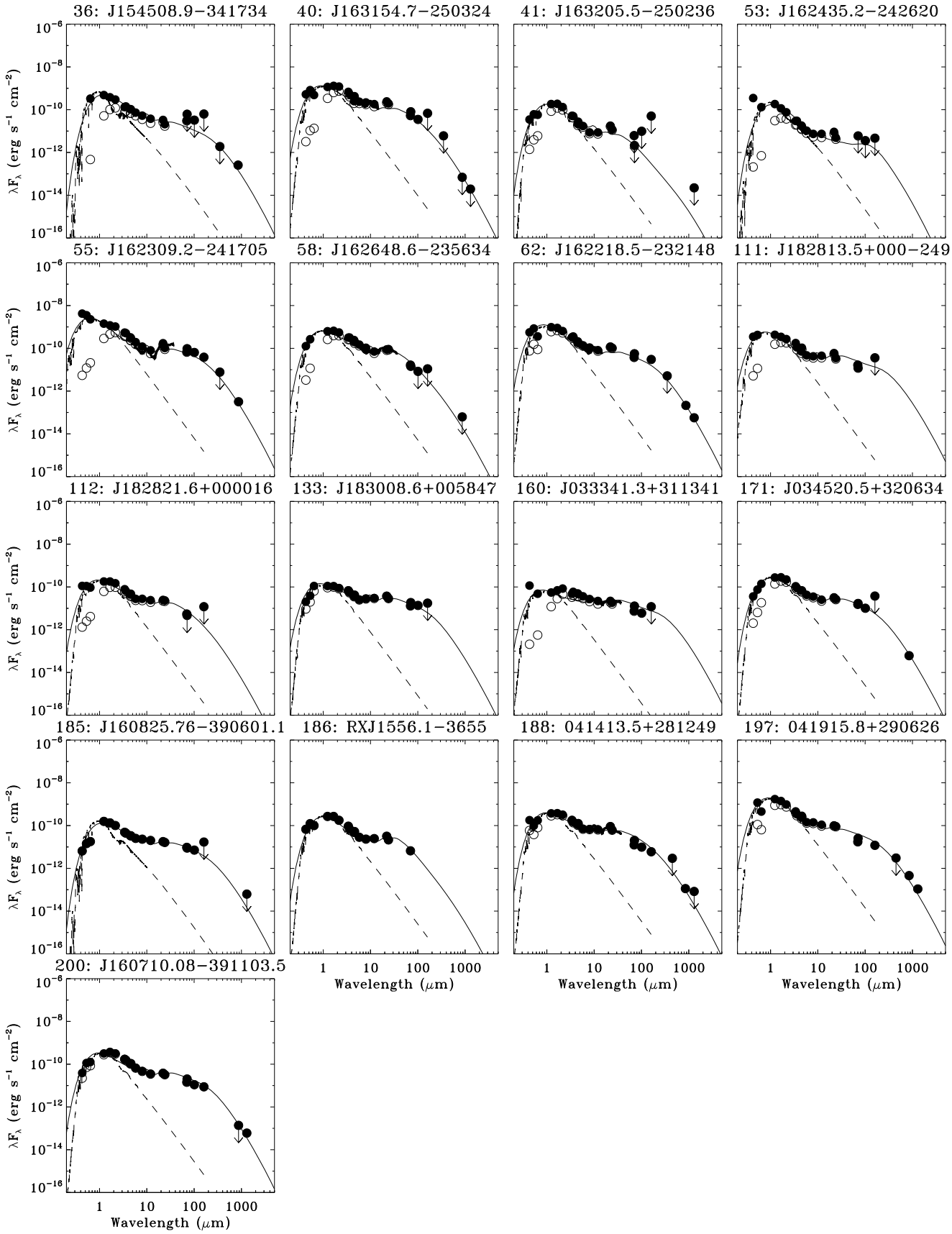

Fig. B.1: SEDs of disks without holes. In this and subsequent Figures the dashed line indicates the stellar spectrum. Open circles denote observed fluxes before extinction correction, filled circles after extinction correction.

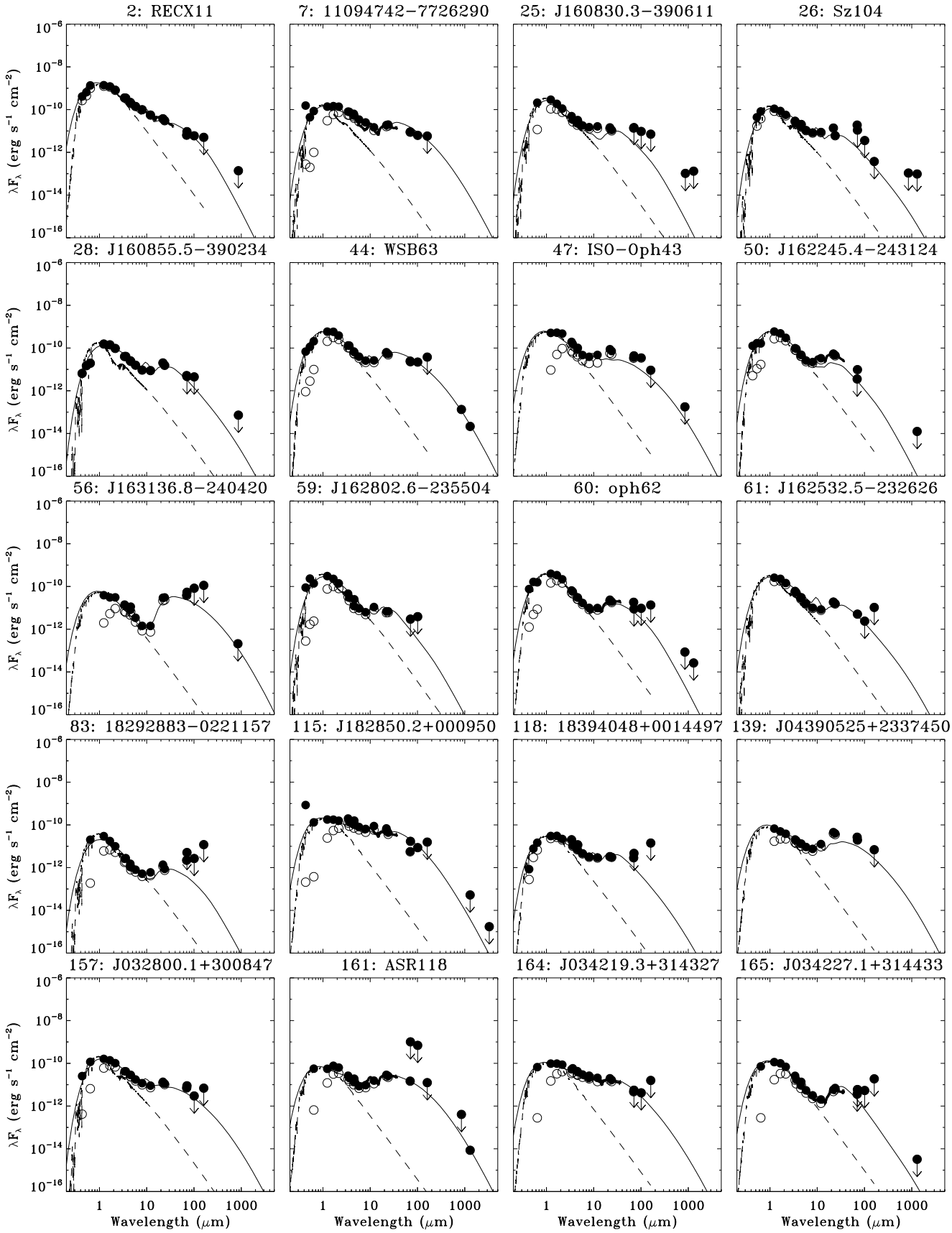

Fig. B.2: SEDs of low-mass disks with small holes.

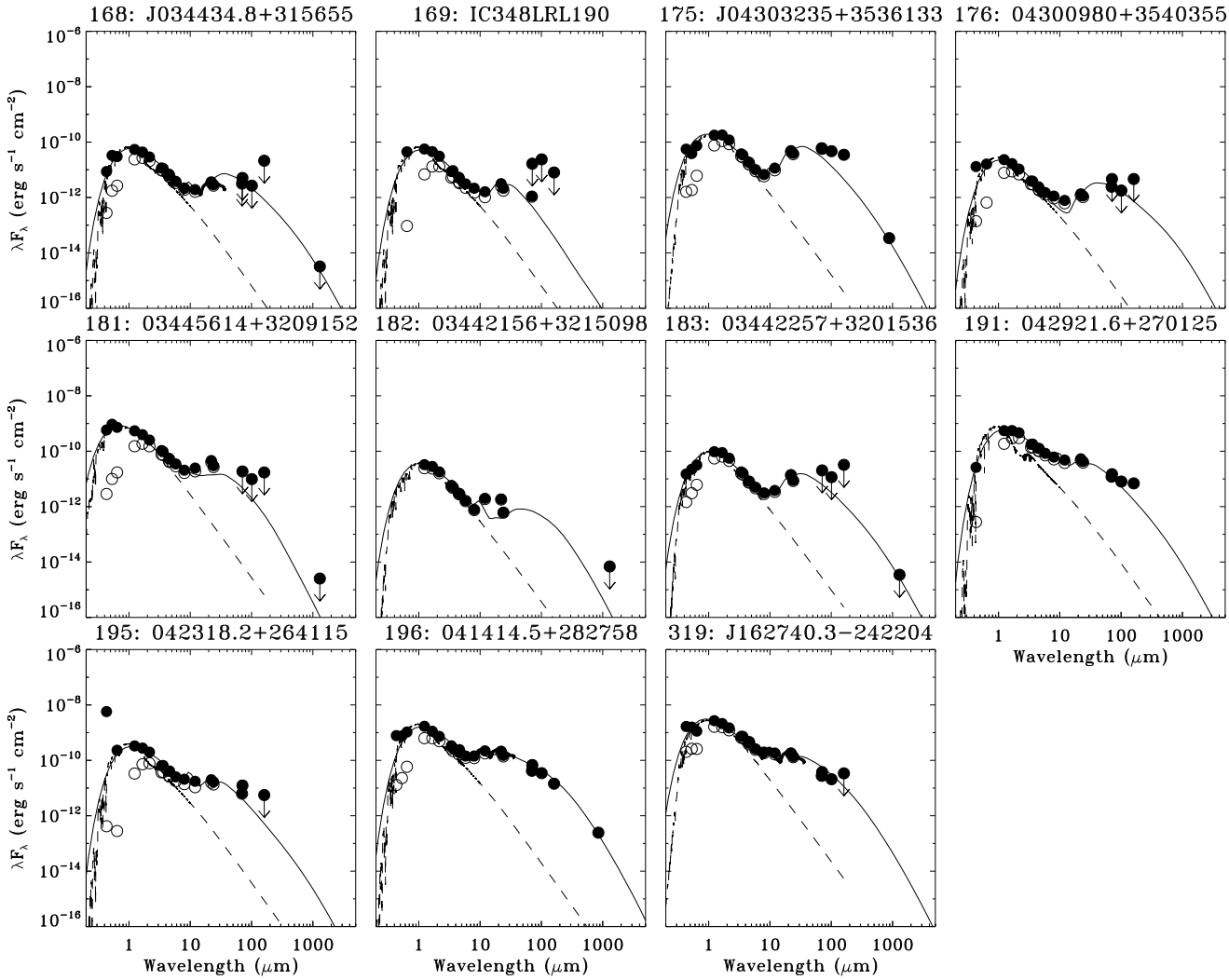

Fig. B.2: SEDs of low-mass disks with small holes.

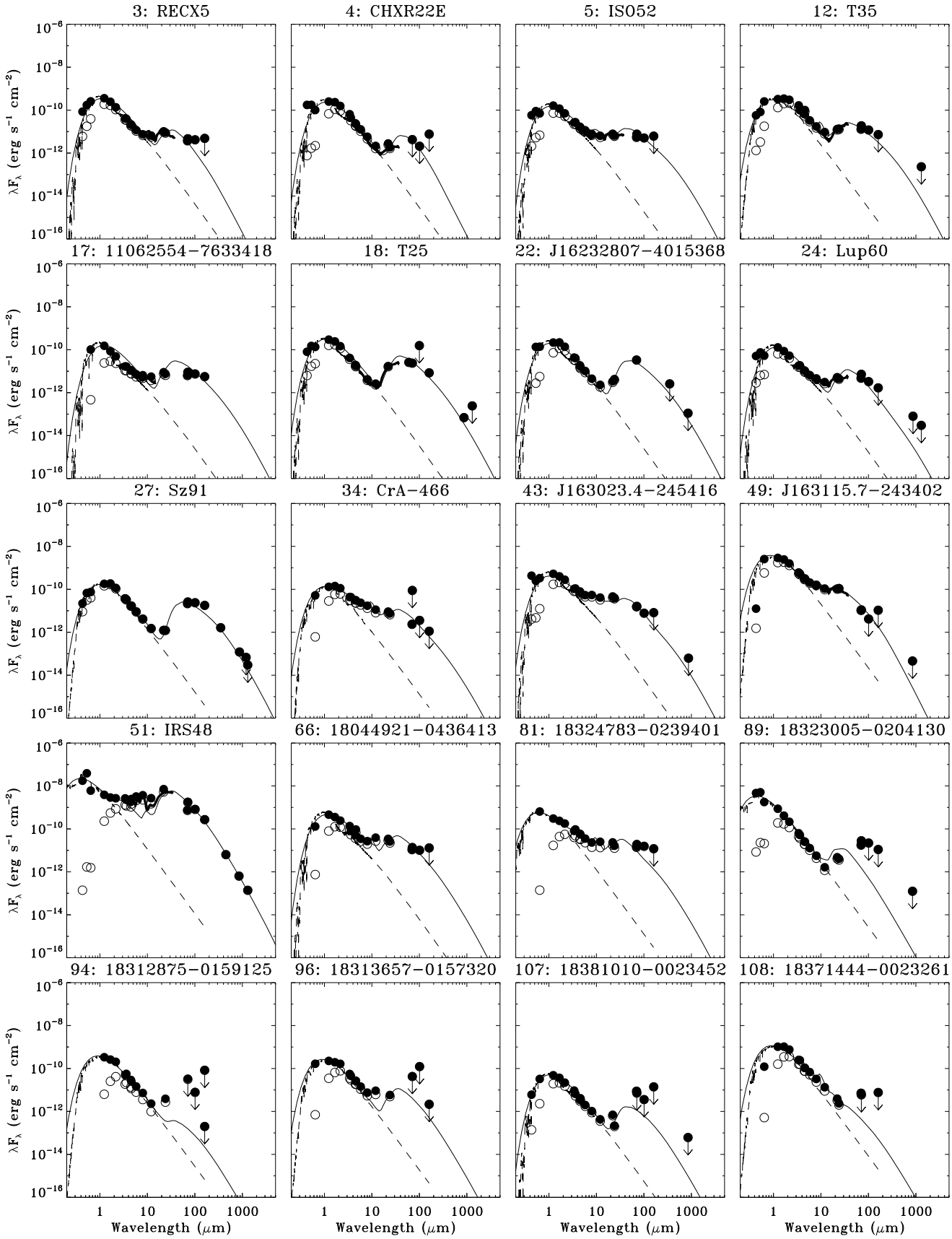

Fig. B.3: SEDs of low-mass disks with large holes.

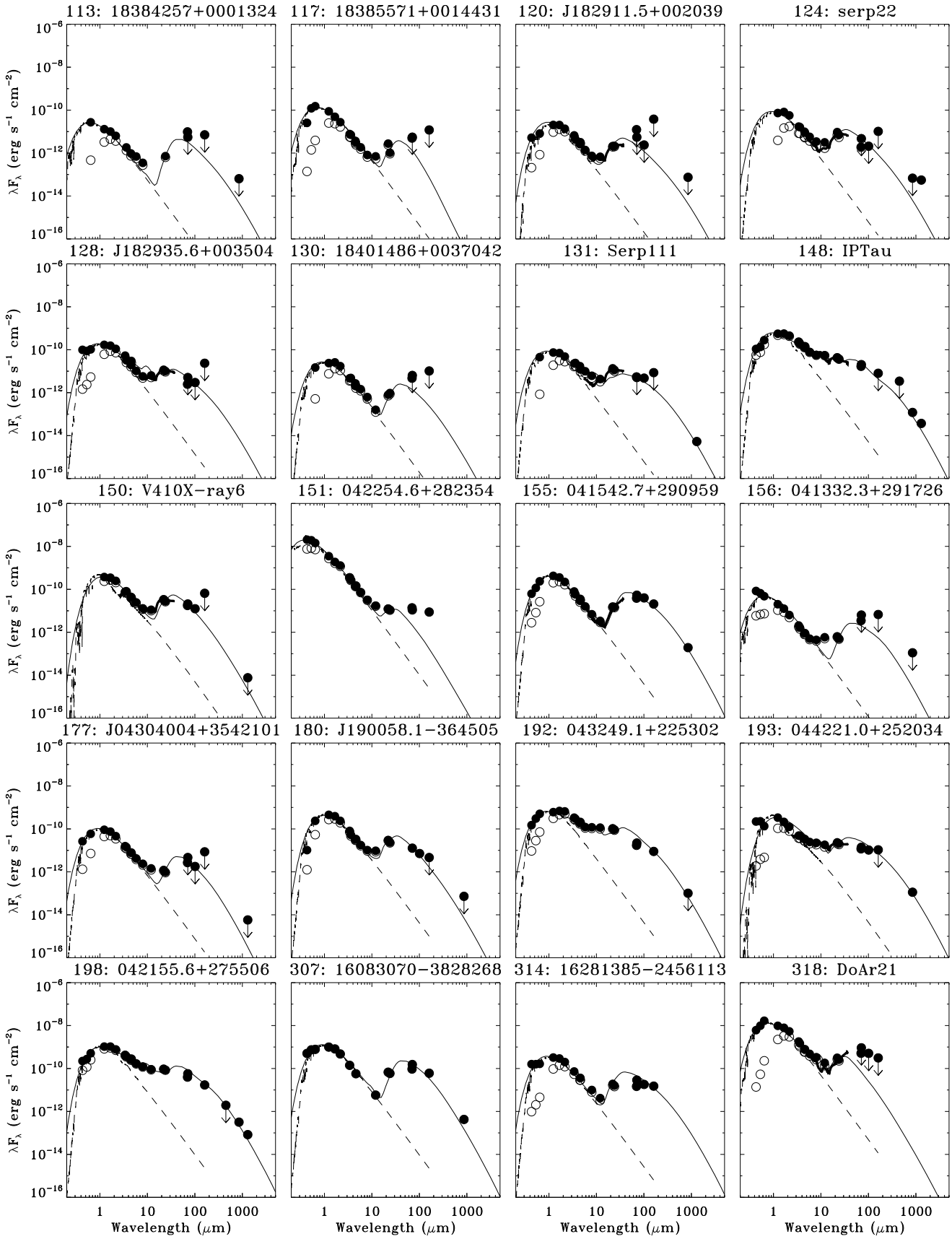

Fig. B.3: SEDs of low-mass disks with large holes.

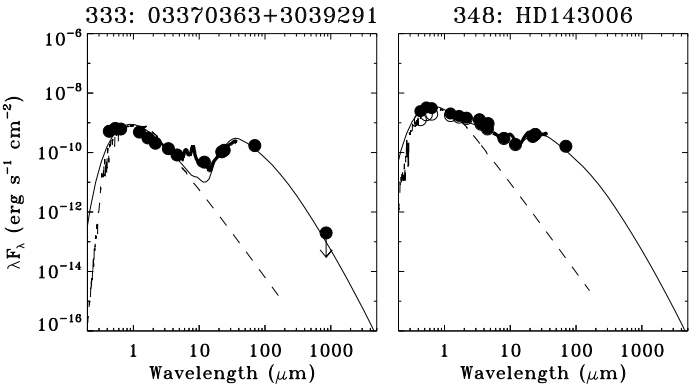

Fig. B.3: SEDs of low-mass disks with large holes.

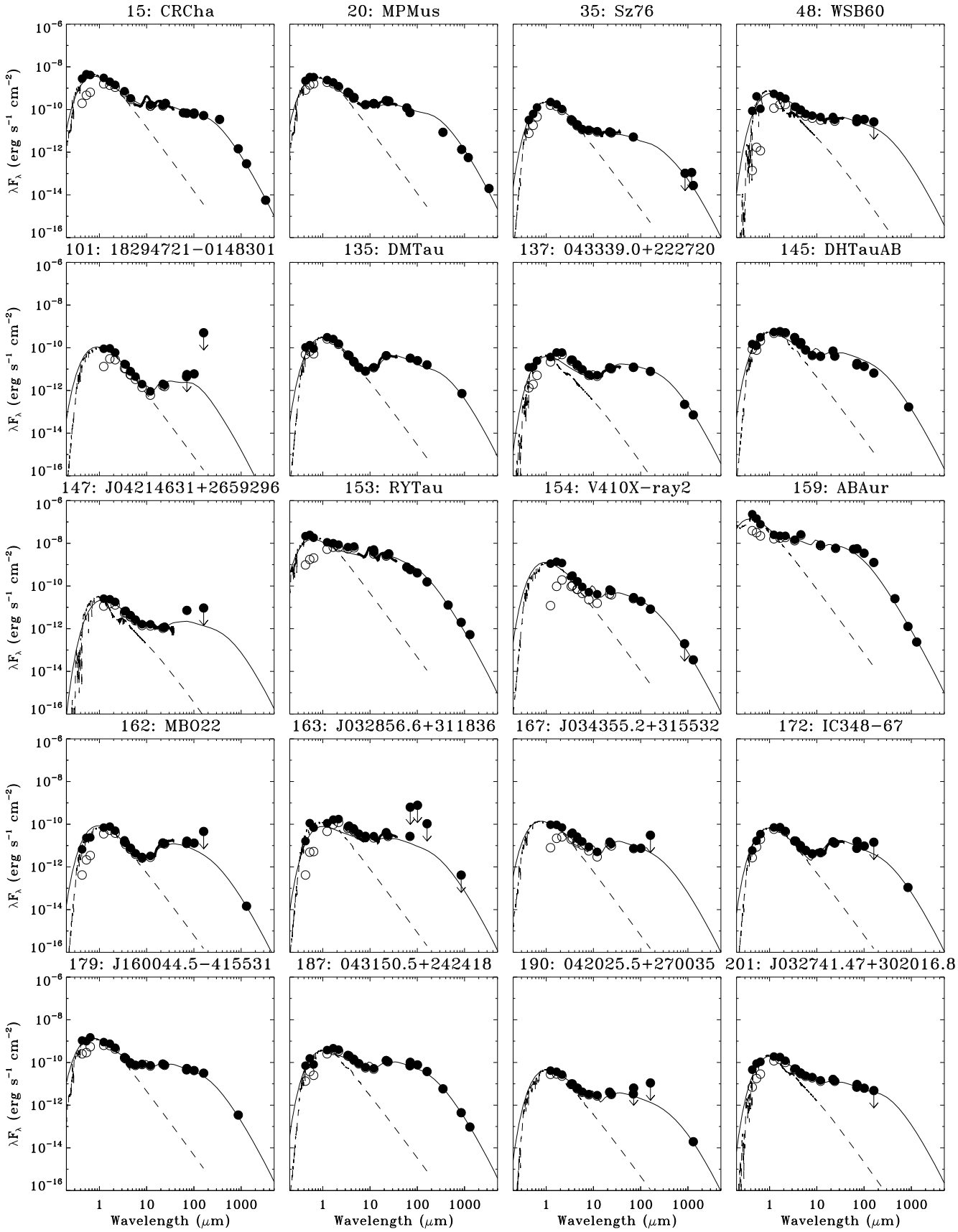

Fig. B.4: SEDs of massive disks with small holes.

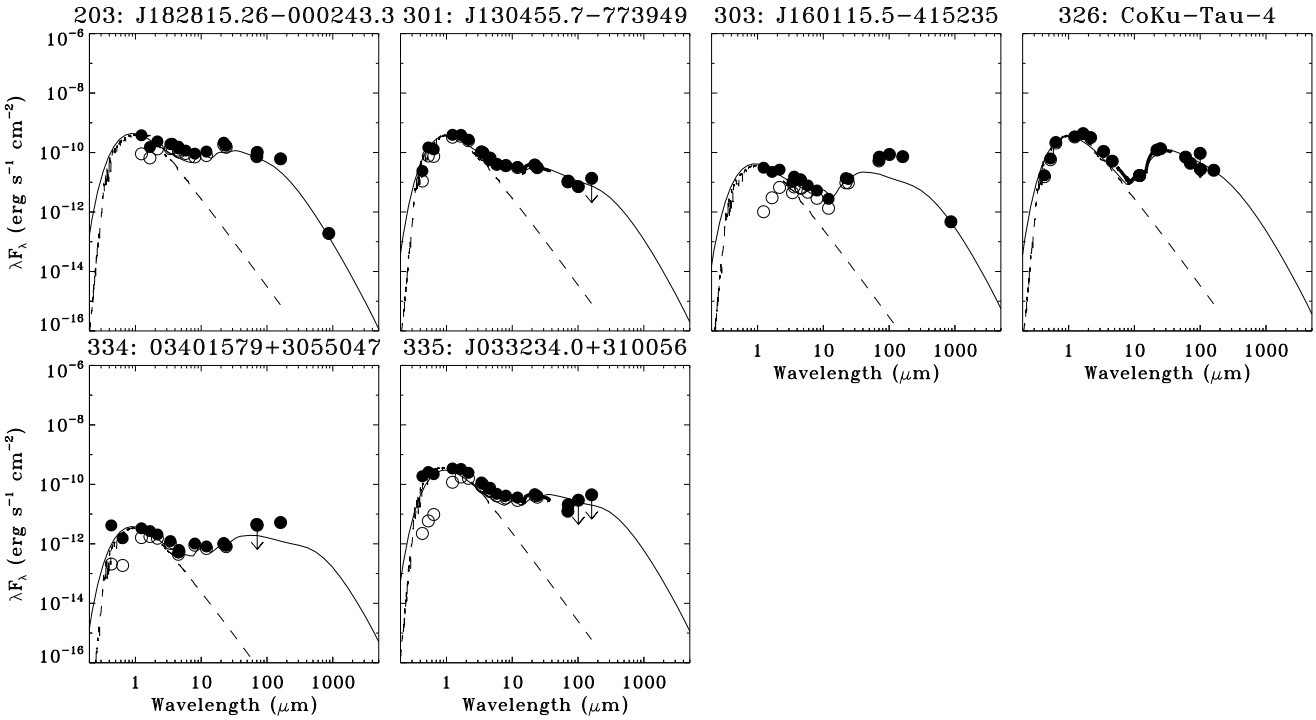

Fig. B.4: SEDs of massive disks with small holes.

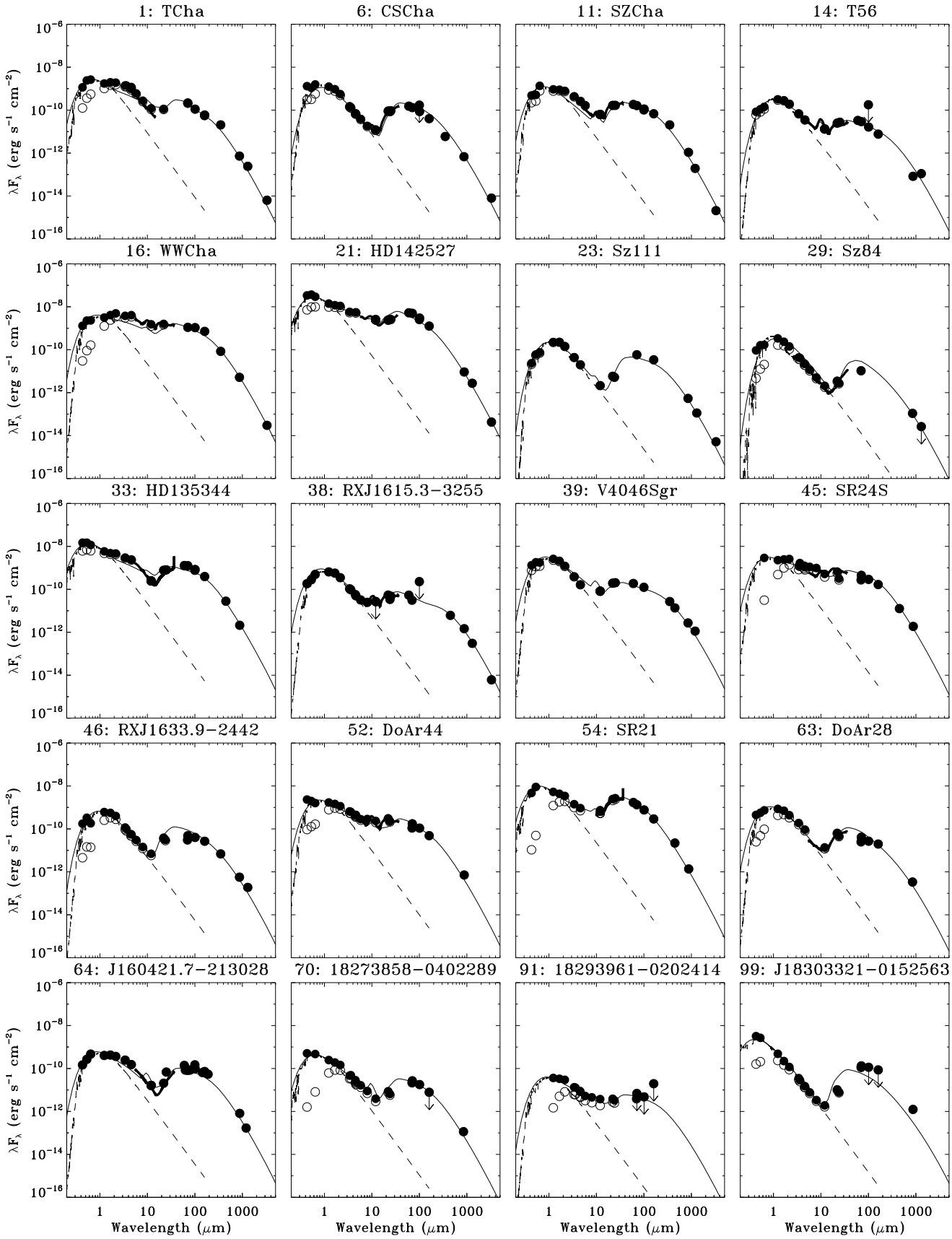

Fig. B.5: SEDs of massive disks with large holes.

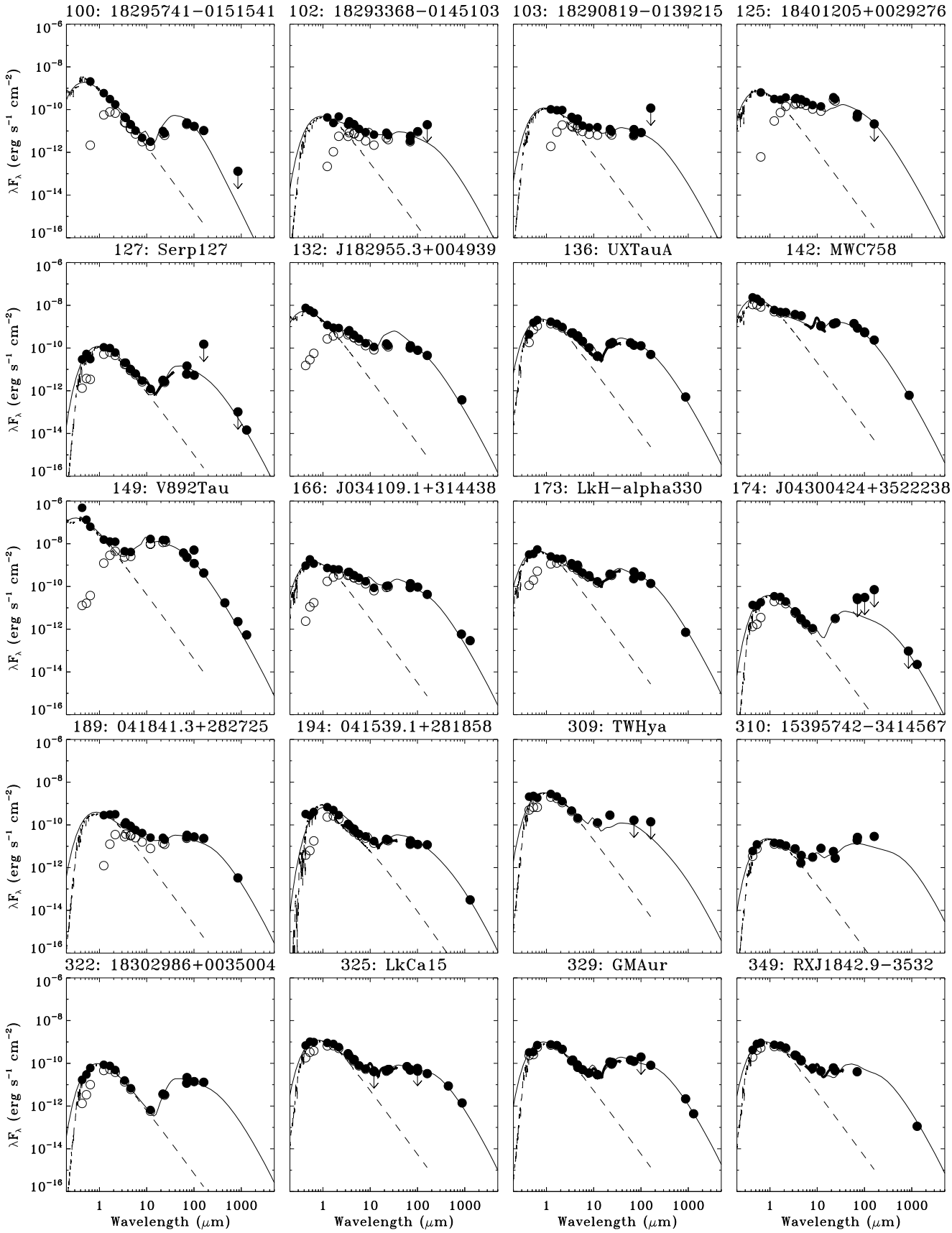

Fig. B.5: SEDs of massive disks with large holes.

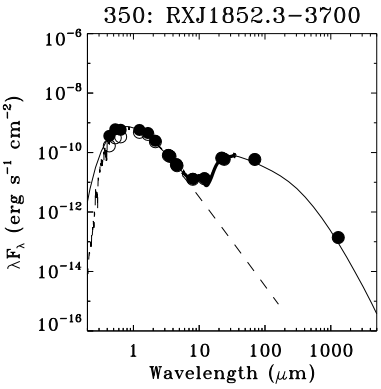

Fig. B.5: SEDs of massive disks with large holes.

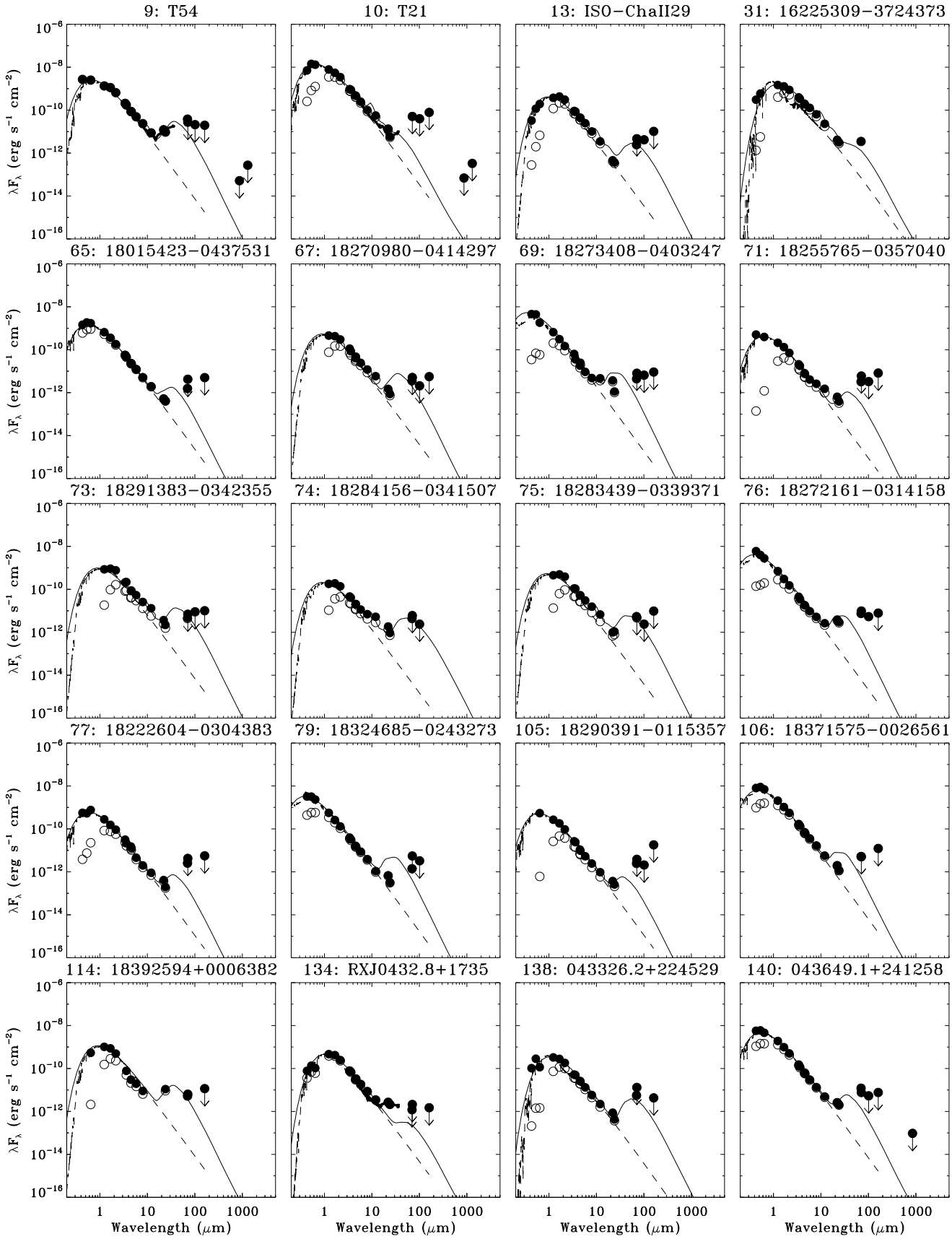

Fig. B.6: SEDs of low scale height disks.

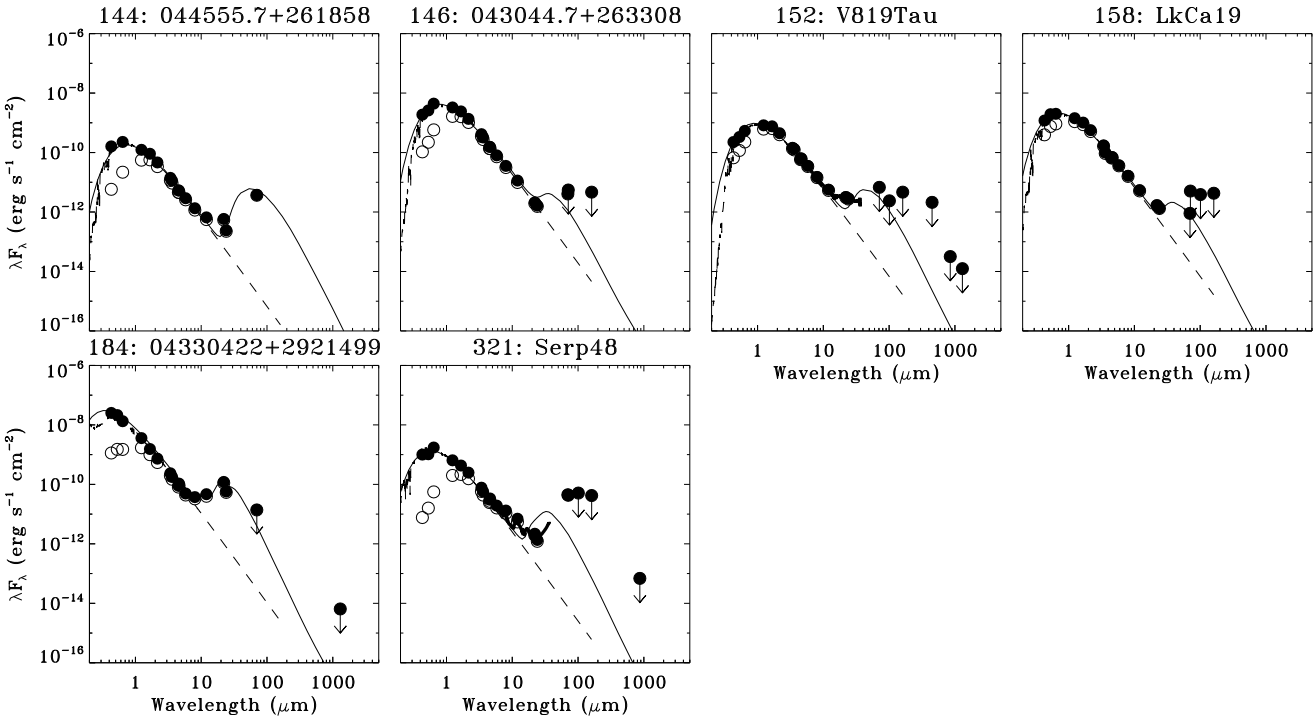

Fig. B.6: SEDs of low scale height disks.

Appendix C: Submillimeter photometry

Table C.1: Submillimeter photometry

ID	SABOCA [350 μm] (mJy)	LABOCA [870 μm] (mJy)	SCUBA [450 μm] (mJy)	SCUBA [850 μm] (mJy)	SMA [880 μm] (mJy)	230 GHz [1.3mm] (mJy)	110 GHz [3.3mm] (mJy)	Ref
1	2400±200	210±20				105±150	7±1	1,2
2		<40						1
6	690±180	197±12.2					8.8±1.5	1,3
9		<15				<118		1,2
10		<20				<143		1,2
11	2400±500	314±12				77.5±20.3	2.3±0.4	1,4
12						<100		2
14		24±6				47.8±15.5		1,2
15	4000±200	420±50				124.9±24	6.2±1.5	1,2
16	9800±2400	1500±10					33.1±1.2	1,3
18		20±6				<105		1,2
20	1000±200	390±10				224±8	22±3.3	1,5
21					2700±270	1190±30	47±6	6,7
22	<300			<31.4				1
23				153.2±11.5		49±4.8	5.7±0.7	1,4
24		<23.2				<13		8,4
25		<30				<57		1,9
26				<30.5		<42		1,9
27	190±40	35±3				<27		1,4
28		<21						8
29				30.8±6.6		<11.4		1,10
32	<82			<36.8				1
33			4200±840		620±62			11,12
35		<30				<45		1,4
36	<220			72.6±18.5				1
38			919±184		430±43	132±3.9	6.7±0.6	13,12
39	3154±419		2042±111	770±39		451±20		14
40	<700	<20				<8.4		1,10
41						<9.6		10
43		<18						1
44				37.8±11		9.3±3		1,10
45			1900±380		550±55			13,12
46	800±200	164±14				81.8±2.7		1,10
47				<50.1				1
49				<13				10
50						<5.4		15
51			950±200	180±18		60±6		16,17
52					210±21			12
54			3300±660		400±40			13,12
55	<900	92±6						1
56				<59.1				1
58		<18						1
60				<24.2		<11.4		1,10
62	<600	62±9				24.5±3.1		1,10
63				95.2±16.4				1
64					238±24	67.5±1.4		18
70				32.4±10.7				1
82				<57.1				1
86				<107.1				1
88				<137.3				1
89				<35.4				1
92				<79.3				1
95		49±11						1
98		63±8						1
99		360±30						1
100				<36.8				1

Table C.1: Submillimeter photometry continued

ID	SABOCA [350 μm] (mJy)	LABOCA [870 μm] (mJy)	SCUBA [450 μm] (mJy)	SCUBA [850 μm] (mJy)	SMA [880 μm] (mJy)	230 GHz [1.3mm] (mJy)	110 GHz [3.3mm] (mJy)	Ref
107				<17.3				1
113				<18.2				1
115						<22.8	<1.9	4,4
120				<21.1				1
124				<19.2		24±0.6		1,15
127				<29.2		6.3±0.6		1,15
131						2.3±0.6		15
132		109±11						1
135					210±21			12
136					150±15			12
137				63.2±18		31±2		1,19
140				<27				20
142					180±18			12
145					49±4.9			21
148			<516	34±5		16±5		22
149			2570±350	638±54		234±19		22
150						<3.3		20
152			<317	<9		<5.4		22
153			1920±160	560±30		229±17		22
154				<55.8		15±1		1,19
155				54.5±17.7				1
156				<31.4				1
159			3820±570	359±67		103±18		22
161				<115.1		3.7±0.9		1,15
162						6.3±1.1		15
163				<117.4				1
165						<1.4		15
166				166.7±14		126±12		1,23
168						<1.4		15
171				17.3±5.7				1
172				31±6				20
173					210±21			12
174				<26.9		9.7±1.5		1,20
175					10±2			20
177						<2.5		20
178				222.4±16.3				1
179		100±5						8
180		<21						8
181						<1.1		20
182						<3		20
183						<1.5		20
184						<2.8		20
185						<27		9
187	680±114			125.5±18.3		41±5		22,1
188			<442	32±8		<36		22
189				93.4±15.7				1
190						8.4±1.4		19
192				<28.6				1
193				31.9±9.4				1
194						13.4±1.4		19
196				69.3±18.8				1
197			<456	130±7		47±0.7		22
198			<291	90±7		36±5		22
200		<40				26±9		1,24
202				<55.5				1
203		55±10						1
303		136±7						1
307		123±14						1
316		98±13						1

Table C.1: Submillimeter photometry continued

ID	SABOCA [350 μm] (mJy)	LABOCA [870 μm] (mJy)	SCUBA [450 μm] (mJy)	SCUBA [850 μm] (mJy)	SMA [880 μm] (mJy)	230 GHz [1.3mm] (mJy)	110 GHz [3.3mm] (mJy)	Ref
321		<20						1
325			1310±260		410±41			13,12
329					640±64	189±15		12,25
333				<56.1				1
349						49±9		26
350						60±8		26

Refs. 1) This work. 2) Henning et al. (1993), 3) Lommen et al. (2007), 4) Lommen et al. (2010), 5) Gräfe & Wolf (2013), 6) Fukagawa et al. (2013), 7) Verhoeff et al. (2011), 8) Romero et al. (2012), 9) Merín et al. (2008), 10) Cieza et al. (2010), 11) Pérez et al. (2014), 12) Andrews et al. (2011), 13) van der Marel et al. (2015), 14) Jensen et al. (1996), 15) Merín et al. (2010), 16) van der Marel et al. (2013), 17) Brown et al. (2012), 18) Mathews et al. (2012), 19) Andrews et al. (2013), 20) Cieza et al. (2012b), 21) Andrews & Williams (2007b), 22) Andrews & Williams (2005), 23) Enoch et al. (2006), 24) Nuernberger et al. (1997), 25) Isella et al. (2009), 26) Hughes et al. (2010)

Appendix D: Herschel photometry

This section presents the fluxes and cut out maps of the Herschel PACS photometry.

Table D.1: Herschel photometry

ID	PACS 70 (mJy)	PACS 100 (mJy)	PACS 160 (mJy)
1	4.98±0.5	3.74±0.37	3.17±0.32
2	0.22±0.03	0.20±0.04	<0.27
3	0.11±0.03	0.14±0.03	<0.26
4	<0.10	<0.07[a]	<0.41[a]
5	0.18±0.05	0.17±0.03	<0.33[a]
6	3.11±0.31	2.90±0.29	2.15±0.25
7	0.21±0.04	0.21±0.03	<0.31
9	<0.65[a]	<0.71[a]	<1.06[a]
10	<1.20[a]	<1.34[a]	<4.21[a]
11	3.86±0.39	3.80±0.38	3.65±0.37
12	0.44±0.05	0.40±0.05	<0.39
13	<0.11	0.14±0.03	<0.55[a]
14	0.69±0.08	0.55±0.06	0.41±0.07
15	1.58±0.16	2.31±0.23	2.80±0.28
16	26.06±2.92	36.06±3.9	38.45±6.0
17	0.21±0.05	0.25±0.03	0.30±0.09
18	0.56±0.07	-	0.45±0.1
21	117.78±11.78	100.65±10.06	67.82±6.78
23	1.38±0.14	-	1.82±0.2
24	0.17±0.04	0.11±0.03	<0.09[a]
25	<0.34	<0.32	<0.38[a]
26	<0.26	<0.12[a]	<0.02[a]
27	0.61±0.07	0.80±0.08	0.96±0.17
28	<0.11	<0.15	<-0.11[a]
32	0.73±0.08	<1.61[a]	<2.98[a]
33	29.8±2.98	28.3±2.83	21.13±2.11
34	<2.09	<0.12	<0.06[a]
36	<1.44	<1.09[a]	<3.36[a]
40	1.89±0.2	1.18±0.15	<3.65
41	<0.05[a]	<0.33[a]	<2.70[a]
43	0.38±0.05	0.26±0.05	<0.44[a]
44	0.54±0.06	0.74±0.09	<2.02[a]
45	10.58±1.06	9.74±0.98	8.96±0.96
46	1.14±0.12	1.35±0.14	1.43±0.27
47	1.00±0.22	1.15±0.37	<0.49[a]
48	0.86±0.09	1.16±0.12	<1.41
49	0.26±0.04	<0.14	<0.57[a]

Table D.1: Herschel photometry continued

ID	PACS 70 (mJy)	PACS 100 (mJy)	PACS 160 (mJy)
50	0.23±0.05	-	<-0.06[a]
51	41.14±4.12	27.3±2.77	14.53±4.18
52	4.10±0.41	3.66±0.37	2.60±0.5
53	<0.14	<0.12[a]	<0.25[a]
54	31.58±3.16	25.75±2.58	15.61±1.88
55	2.26±0.23	2.15±0.22	2.06±0.35
56	1.26±0.39	<2.78	<6.05[a]
58	0.34±0.05	<0.28	<0.59[a]
59	<0.07	<0.13	<-0.06[a]
60	<0.21[a]	<0.32	<0.73[a]
61	0.12±0.04	<0.08	<0.56
62	1.32±0.14	-	1.62±0.31
63	0.97±0.11	0.90±0.1	1.06±0.26
64	-	3.48±0.35	3.88±0.84
65	<0.10	-	<0.27
66	0.32±0.05	0.34±0.04	<0.70[a]
67	<0.12	<0.07	<0.30
68	<0.13	<0.08	<0.34
69	<0.19	<0.22	<0.49
70	0.63±0.07	0.60±0.06	<0.42
71	<0.14	<0.11	<0.44
73	<0.16	<0.30	<0.54[a]
74	<0.14	<0.08	<-0.02[a]
75	<0.11	<0.08	<0.52
76	0.23±0.04	0.18±0.04	<0.42
77	<0.10	-	<0.30[a]
78	<0.14	<0.10	<0.88
79	<0.13	<0.11	<-0.08[a]
80	<0.18	<0.24	<0.59
81	0.44±0.06	0.52±0.06	<0.64
82	<0.33[a]	<0.10[a]	<2.61[a]
83	<0.12	<0.09	<0.64
84	<0.12	<0.07	<0.42
85	<0.27	<0.53	<0.05[a]
86	<1.05[a]	<1.40[a]	<1.55[a]
88	<32.9[a]	<26.25[a]	<59.51[a]
89	0.66±0.09	<0.74[a]	<0.59[a]
90	<0.22	<0.22	<1.98
91	<0.16	<0.16	<1.05
92	<0.31[a]	<0.47[a]	<2.55[a]
93	<8.45[a]	<5.27[a]	<10.49[a]
94	<0.74[a]	<0.26[a]	<4.44[a]
95	<2.27[a]	<2.78[a]	<9.57[a]
96	<1.00[a]	<4.13[a]	<-4.57[a]
97	<2.49[a]	<6.83[a]	<8.58[a]
98	<1.46[a]	<3.07[a]	<10.72[a]
99	3.13±0.33	<3.84[a]	<4.62[a]
100	0.56±0.07	0.55±0.06	0.56±0.16
101	<0.13	0.20±0.05	<27.08
102	0.13±0.04	0.31±0.04	<1.05
103	0.27±0.06	0.28±0.08	<6.29
104	<0.14	<0.07	<0.22
105	<0.09	<0.07	<0.97
106	<0.12	-	<0.66
107	<0.17	<0.12	<0.75
108	<0.14	-	<0.41[a]
110	<0.14	-	<0.54
111	0.28±0.06	-	<1.93[a]
112	<0.11	-	<0.64
113	<0.13	-	<0.38

Table D.1: Herschel photometry continued

ID	PACS 70 (mJy)	PACS 100 (mJy)	PACS 160 (mJy)
114	0.15±0.04	-	<0.62
115	0.40±0.06	0.29±0.08	<0.84
116	<0.22	-	<1.02
117	<0.13	-	<0.64
118	<0.11	-	<0.76
119	<0.13	-	<0.02[a]
120	<0.13	<0.08	<2.04
121	<0.59[a]	-	<0.45[a]
122	<0.10	-	<0.07[a]
123	0.13±0.04	<0.07	<0.38
124	<0.11	<0.07	<0.55
125	1.42±0.15	-	<1.14
126	<16.95	<33.54	<3.04[a]
127	0.34±0.05	0.18±0.03	<8.11
128	<0.12	<0.10	<1.26
129	<0.12	-	<0.10[a]
130	<0.15	-	<0.55
131	<0.12	0.16±0.03	<0.46
132	3.03±0.31	2.64±0.27	2.41±0.28
133	0.44±0.06	0.46±0.07	<0.94
134	<0.05	-	<0.08
135	0.77±0.08	0.84±0.09	0.85±0.17
136	3.21±0.32	-	2.68±0.28
137	0.29±0.04	-	0.42±0.09
138	<0.31	-	<0.23[a]
139	0.46±0.07	-	<0.37
140	0.18±0.05	<0.18[a]	<0.41
142	20.39±2.04	17.59±1.76	12.65±2.57
145	0.44±0.06	0.45±0.05	0.35±0.09
146	<0.13	-	<0.25
147	0.17±0.06	-	<0.50
148	0.48±0.08	-	<0.43
149	53.78±5.39	39.92±4.05	22.87±3.33
150	0.49±0.07	0.42±0.08	<3.51
151	0.26±0.05	-	0.47±0.12
152	<0.16	<0.08	<0.25
153	13.82±1.38	-	8.36±0.86
154	0.66±0.09	0.64±0.07	0.44±0.11
155	1.26±0.14	1.34±0.14	1.11±0.13
156	<0.15	-	<0.36
157	0.21±0.05	<0.10	<0.37
158	<0.12	<0.13	<0.23
159	131.87±13.19	-	67.75±6.79
160	0.30±0.05	0.20±0.03	<0.64
161	<23.85	<23.35	<0.67[a]
162	0.38±0.08	0.44±0.09	<2.46
163	<14.92	<26.05	<5.67[a]
164	<0.13	<0.14	<0.85
165	<0.14	<0.18	<1.01
166	3.20±0.32	3.15±0.32	2.28±0.43
167	0.17±0.05	0.25±0.05	<1.64
168	<0.12	<0.09	<1.14
169	<0.39	<0.80	<0.43[a]
171	0.40±0.06	0.34±0.07	<2.01
172	0.37±0.06	0.32±0.05	<0.77
173	11.41±1.14	10.25±1.03	7.38±0.74
174	<0.58[a]	<1.03[a]	<3.80[a]
175	1.35±0.14	1.58±0.16	1.87±0.27
176	<0.11	<0.06	<0.25
177	<0.11	<0.06	<0.46

Table D.1: Herschel photometry continued

ID	PACS 70 (mJy)	PACS 100 (mJy)	PACS 160 (mJy)
178	2.47±0.36	4.41±0.76	10.19±1.65
179	1.23±0.13	1.41±0.14	1.69±0.19
180	0.30±0.04	0.24±0.03	<0.25
181	<0.44[a]	<0.33[a]	<0.92[a]
182	<-0.07[a]	<-0.03[a]	<-0.72[a]
183	<0.48	<0.39[a]	<1.73[a]
185	0.21±0.06	0.24±0.05	<0.91
187	2.41±0.24	2.60±0.26	2.02±0.22
188	0.48±0.1	0.33±0.11	0.32±0.08
189	0.75±0.09	0.91±0.09	1.25±0.16
190	<0.15	-	<0.59
191	0.35±0.07	0.27±0.04	0.37±0.11
192	0.52±0.09	-	0.48±0.16
193	0.33±0.05	0.35±0.04	<0.57
194	0.43±0.06	0.41±0.05	0.63±0.18
195	0.29±0.06	-	<0.30
196	1.60±0.17	1.16±0.12	0.77±0.1
197	0.60±0.08	-	0.64±0.15
198	1.35±0.15	-	0.92±0.14
200	0.48±0.06	0.37±0.05	0.47±0.15
201	0.22±0.05	0.21±0.03	<0.26
202	1.73±0.3	<1.95	<1.53[a]
203	2.39±0.25	-	3.30±0.38
204	<73.51	<60.36	<9.49[a]
301	0.26±0.05	0.24±0.05	<0.73
303	1.63±0.17	2.88±0.29	3.90±0.4
307	3.63±0.37	-	3.24±0.33
309	<3.93[a]	-	<7.50[a]
310	0.62±0.07	-	1.55±0.18
314	0.68±0.07	0.61±0.08	0.81±0.26
317	1.08±0.11	0.69±0.07	<0.38
318	<21.71[a]	<17.06[a]	<16.7[a]
319	0.89±0.1	0.70±0.12	<1.82[a]
321	1.02±0.11	<1.72[a]	<2.26[a]
322	0.51±0.07	0.47±0.05	0.70±0.14
325	1.20±0.13	1.45±0.15	1.77±0.38
326	1.03±0.11	0.92±0.09	1.36±0.35
329	2.93±0.3	-	4.34±0.44
334	<0.10	-	0.28±0.09
335	0.49±0.15	<0.99	<2.39
336	<0.12	0.13±0.02	<0.18

Notes. [(a)] Upper limit due to cloud confusion.